UNIVERSITÀ DEGLI STUDI DI MILANO

PhD School in Physics, Astrophysics and Applied Physics
Department of Fisica

Cycle XXXII

Development of a novel sunphotometer for aerosol and dust characterization in the atmosphere

Disciplinary Scientific Sector FIS/07

PhD Thesis of:
Agostino TETTAMANTI

Supervisor of the Thesis: **Professor Marco A. C. POTENZA**

Director of the School: **Professor Matteo PARIS**

A.Y. 2019-2020

Contents

CHAPTER 1

Introduction

The term aerosol refers to a suspension of solid particles or liquid droplets in a gaseous medium (Iqbal 1983[3]). Aerosols are a two-phase system, consisting of the suspended solid or liquid phase, and the surrounding gas phase (Kulkarni, Baron, and Willeke 2011 [23]). During the last decades, aerosols and the need to measure them have acquired more and more importance. For istance, aerosols can affect human health because great aerosol loads degrade the air quality (Schwartz and Neas 2000 [11]). This problem regards specially urbanized areas, such as the Po Valley in Europe (Mazzola, Lanconelli, Lupi, *et al.* 2010 [22]; Putaud, Cavalli, Martins dos Santos, *et al.* 2014 [28]).

In addition, volcanic eruptions can generate plumes that are dangerous for aviation. Consequently, the air routes have to be diverted, with subsequent economic damage. Hence, it is very important to monitor the spread of the aerosol plumes.

Finally, aerosols also impact on the radiative balance of the Earth atmosphere with three types of interactions: direct, semi-direct and indirect:

– aerosols scatter and absorb solar radiation, this is the direct effect (Dubovik, Smirnov, Holben, *et al.* 2000 [10]).

– The aerosol particles change the atmospheric thermodynamics (Kazadzis, Bais, Amiridis, *et al.* 2007 [16]). They heat the surrounding environment, reduce the ambient relative humidity and lead to evaporation of clouds. This kind of interaction is known as semi-direct effect.

– Finally, aerosols act as cloud condensation nuclei. They influence the cloud microphysics and increase the amount of clouds (Twomey 1977 [1]).

7

Considering the great effects that aerosols can have, their characterization is an important even if complex task. Their properties, indeed, are highly variable, both in time and space (Hess, Koepke, and Schult 1998 [7]). Different aerosols have different sizes, chemical compositions and lifetimes in the atmosphere. Some aerosol species travel large distances before deposition (fine aerosols, saharan dust). Some of them have anthropogenic origins, others are natural. All these factors make aerosols the most uncertain driver of global climate change (IPCC 2013 [25] and Heald, Ridley, Kroll, *et al.* 2014 [26]).

Most aerosol measurement techniques fall into two categories: the first relies on collection of aerosols on a substrate for subsequent laboratory measurements. The second allows in situ measurements of aerosols. The first approach offers powerful analytical techniques, generally available only in the laboratory. However, this approach has a disadvantage in that the particles may be modified by the transport and collection processes. On the other hand, in situ techniques (such as remote sensing) provide non-invasive measurements, but the degree of particle characterization is more limited. Moreover, they rely on complicated inversions (Kulkarni, Baron, and Willeke 2011 [23]).

A primary tool to analyze the aerosol interactions with solar radiation is the remote sensing (Dubovik 2004 [15]). Indeed, during the past 20 years international networks of ground-based photometers were set up. The most widespread network is the AERONET network (initiated by NASA), with measurement sites all over the world. (Holben, Eck, Slutsker, *et al.* 1998[8]). Another network is the ESR-SKYNET (Estellés, Campanelli, Smyth, *et al.* 2012[24]). Despite their widespread use, the limitation of these networks is their low geographical coverage. Satellite instrumentation fills the geographical gaps, but the retrieval of aerosol properties from satellite radiances is not easy (Drury, Jacob, Spurr, *et al.* 2010 [21]). Thus, ground-based measurements are the most accurate. Furthermore, they are necessary to calibrate and validate satellite retrieval products and improve satellite algorithms.

The ground-based sunphotometer measures the direct normal irradiance and the angular distribution of sky radiance. Both the measurements are multi-spectral. From the direct normal irradiance the aerosol optical depth is retrieved. The latter quantity is a key parameter for various aerosol-related studies (e.g. the aerosol radiative forcing). The sky radiance allows the retrieval of the aerosol phase function (Nakajima et al. 1983[4]; Nakajima et al. 1996[6]). Optical depth, phase function and single-scattering albedo provide a compre-

hensive consideration of aerosol radiative properties. Generally, proper algorithms invert the photometer measurements and derive the single scattering albedo, as well as the aerosol microphysical parameters (Dubovik, Smirnov, Holben, *et al.* 2000[10]).

1.0.1   The goal of my PhD

My PhD activity is part of the GAIA project (Geolocalized Aerosol characterization by Integrated Arrays). The local government of the Aosta Valley (Northern Italy) funds GAIA through the european ESF program. GAIA aims at streghtening the aerosol monitoring network of the Aosta Valley.

During my PhD I designed a novel sunphotometer. It's name is ARBOL (ARray of BOLometers). ARBOL is new, cheap and efficient. ARBOL mechanics, electronics and acquisition software were created from scratch.

ARBOL is more flexible than common sunphotometers. For example, the acquisition software is written ad-hoc. For this reason, the user can set arbitrary measurement sequences and acquisition times. During tests the direct normal irradiance was measured every 5 seconds. A commercial POM photometer from PREDE measures the same quantity once per minute. ARBOL can reach a higher sampling frequency.

The mechanical structure and the electronics layout of ARBOL are novel too. The mechanics provides the following benefits:
- six telescopes observe the same direction in six different wavelengths. Thus, ARBOL spectral measurements are actually simultaneous.
- Each telescope optics provides a spectral and angular selection of the incoming light.
- ARBOL is light. It can be transferred easily from one site to another.

The front-end electronics of ARBOL relies on a novel design. Here, the major challenge is the wide dynamic range of the signal. A double stage preamplifier provides two gain values to measure very different light levels with the same sensor.

In the framework of the GAIA project, the Aosta Valley environment is particularly interesting because it is representative of mountainous environments. Here, intricate weather patterns influence the aerosol dynamics. Mountain-valley breezes bring polluted air masses from the neighboring Po valley (Diémoz, Barnaba, Magri, *et al.* 2019

[33]). Temperature inversions push down the aerosols into the lowest atmospheric layers. Accordingly, two ARBOL measurement sites have been set up. They are just few km away, but at different altitudes. The goal is to study the air quality differences between the two places.

The first site is at the local Environment Protection Agency (ARPA), in the suburbs of the city of Aosta ($583m$ a.s.l). The second site is located at the astronomical observatory of Saint Barthelemy (OAVdA). This site is $1700m$ a.s.l.

Both the ARBOL instruments were characterized and tested during my PhD. Moreover, ARPA already manages a POM02 sunphotometer from PREDE. The instrument is part of the ESR-SKYNET network. Both the ARBOLs were calibrated with the calibration tranfer from POM.

The thesis describes in detail the design, structure and implementation of each component of ARBOL. Furthermore, it discusses the instrumental characterizations and the calibrations. Finally, preliminary results from the two measurement sites are reported. Measurements were collected between Spring and Summer 2019. The structure of the thesis is the following:

- chapter 2 describes the opto-mechanical structure of ARBOL, as well as the solar tracking. The Sun is tracked thanks to an active feedback system.
- chapter 3 highlights the electronics: the front end analog circuit; the temperature monitoring system; the management of the supply and the digital gain control.
- chapter 4 deals with the signal acquisition. The acquisition timings, the custom software and the acquisition hardware are described.
-chapter 5 is about the instrument characterizations.
-chapter 6 deals with measurements. The calibration approach and the optical depth retrieval are described. Measurements are presented, uncertainties and accuracies discussed.

Finally, let me stress one more advantage. Further instrument development is possible from ARBOL novel technology. For example, the telescopes of ARBOL are light collectors. They are a good starting point to create a novel MAX-DOAS instrument. The latter technique retrieves the vertical column density of pollution gases. It measures scattered sunlight at different elevation angles and it searches for the pollutant absorption spectrum.
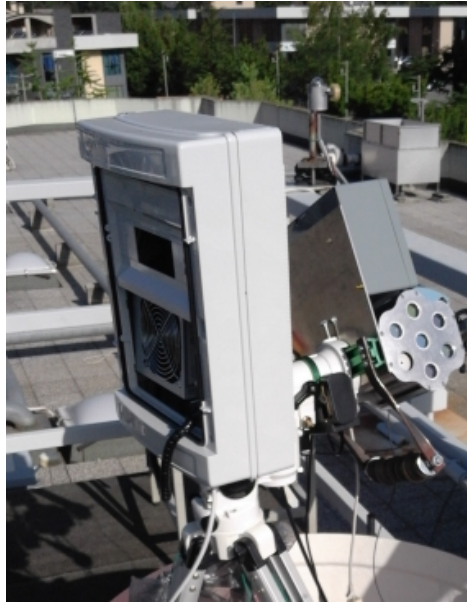
(a) ARBOL located at the ARPA site

(b) ARBOL located at the Observatory site

Figure 1.1

Opto-mechanical design of ARBOL

The current chapter describes the mechanical structure and the optics of ARBOL. The latter imposes the mechanical specs. The workshop of the Physics Department ("Officina Meccanica del Dipartimento di Fisica") created each mechanical component ad-hoc. All the components are built with anticorodal aluminum alloy to limit the total weight. The conceptual design was made in collaboration with Daniele Viganò.

2.1 General Layout
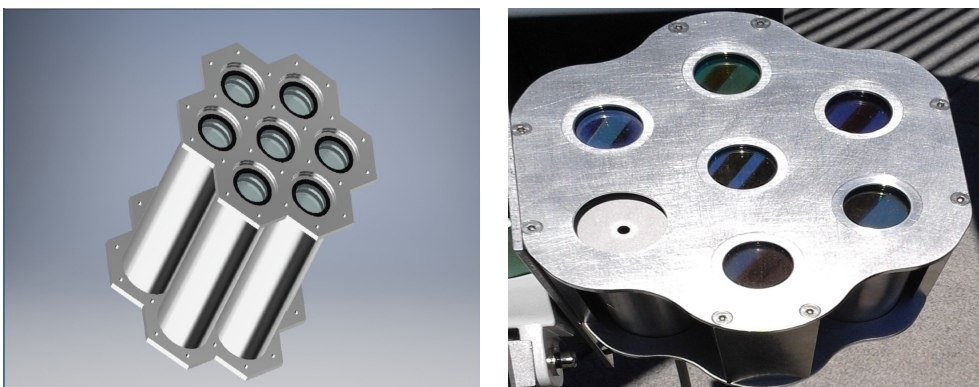
(a) ARBOL: the mechanical design ...   (b) .. and the instrument.

Figure 2.1

Figure 2.1 shows the mechanical structure of ARBOL. The instrument is $149mm$ long, $136mm$ large and $135mm$ high. Its weight is

approximately 1.8kg. The instrument body is made up of seven parallel cylinders: six of them are telescopes designed to collect sunlight or skylight and the seventh is for solar tracking. A feedback network manages the tracking mechanism.

Each of the telescopes fulfills the following specs:

1) it is $130mm$ long, with a $0.1mm$ tolerance

2) the internal diameter is $35mm$

3) the external diameter is $38mm$

Two identical flanges press the telescopes from above and below to keep the telescopes aligned and fixed. The flanges are screwed to four rectangular $125mm$ long spacers.

Let's analyze the telescope internal structure. Cylindrical sections keep the internal components (lenses, electronic boards, baffles, filters) at fixed distances (see fig. 2.3 below). These sections have the following geometry:

4) the internal diameter is $32mm$

5) the external diameter is $34.9mm$

6) the length coincides with the distance to be kept between internal components.

The sections can pass into the telescope because diameter "5)" is $0.1mm$ smaller than diameter "2)". The internal components have a disk shape with a diameter of $34.9mm$. Inside the telescope, sections and components are stacked on top of each other. The telescope and the stack lengths are the same ($130mm$). The screwed flanges fix everything togheter.

Proper O-rings compensate the flange pressure on the inside. When the system is screwed, the inner sections, the telescopes and the spacers perfectly match into the flanges.

The mechanical design allows an easy maintenance. When one of the flanges is unscrewed, the inside of ARBOL is accessible (fig. 2.2).

Finally, the cylindrical sections have opaque black internal walls to reduce the stray light inside the instrument.

2.2   The structure inside a telescope

We leave the tracking telescope for later (see sect. 2.4) and focus now on the other ones. These six telescopes measure six different wavelengths. Thus, each telescope has a different bandpass filter inside. Nevertheless, their inner light path is the same.

Figure 2.2. ARBOL during maintenance. An unscrewed flange can be appreciated

2.2.1   The optics
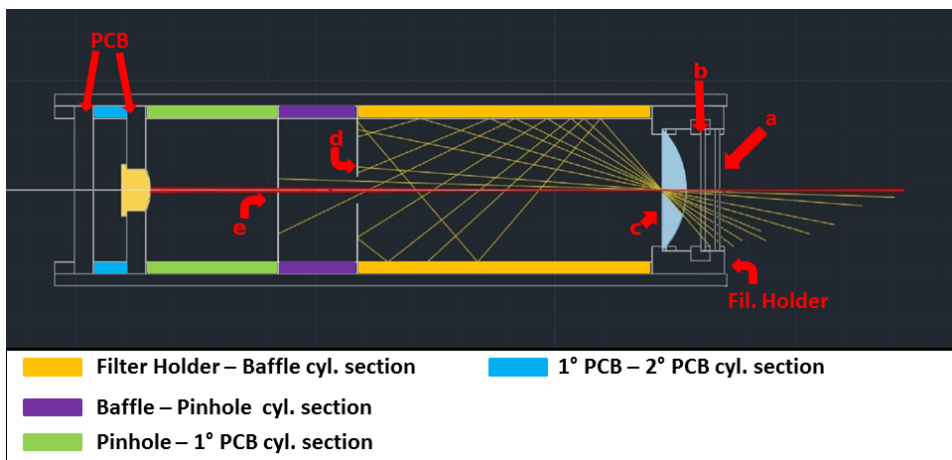
Figure 2.3. A telescope profile view. Different colors highlight different cylindrical sections

Figure 2.3 shows the light paths through a telescope. The incoming light (from right to left) passes through a plane parallel optical window (a), a bandpass filter (b), the objective lens (c), a baffle (d) and a pinhole (e). As explained above, cylindrical sections keep the components in place.

a) The optical window is composed by borosilicate (NBK-7) glass.

Basically, the window protects the main optical components from dust.

b) The filter operates the spectral selection. ARBOL observes six wavelengths: $400nm$, $500nm$, $675nm$, $870nm$, $940nm$, and $1020nm$. The filter FWHM is approximately $10nm$ for all but the $1020nm$ wavelength. The latter is $15nm$. The filter selection is a trade-off between two opposite needs:

- ARBOL data analysis is based on the Lambert-Beer law. This law applies to monochromatic light. Thus, observations should be monochromatic.

- Narrow filter responses reduce the light levels and make detection difficult. So the filter response cannot be too narrow.

A filter with $FWHM = 10nm$ is the ideal compromise. The filters responses of ARBOL are calibrated (fig. 2.4).

Figure 2.4. Filter spectral responses

c) The objective is a plano-convex lens (borosilicate glass). It collects light in its rear focal plane.

The pin-hole e) fixes the instrument field of view. Its position is

centered on the lens focal spot. Let φ be the pin-hole diameter, f the focal length of the lens. Light parallel to the telescope axis or within the angle

$$\theta \leq \frac{\varphi}{2f} \tag{2.1}$$

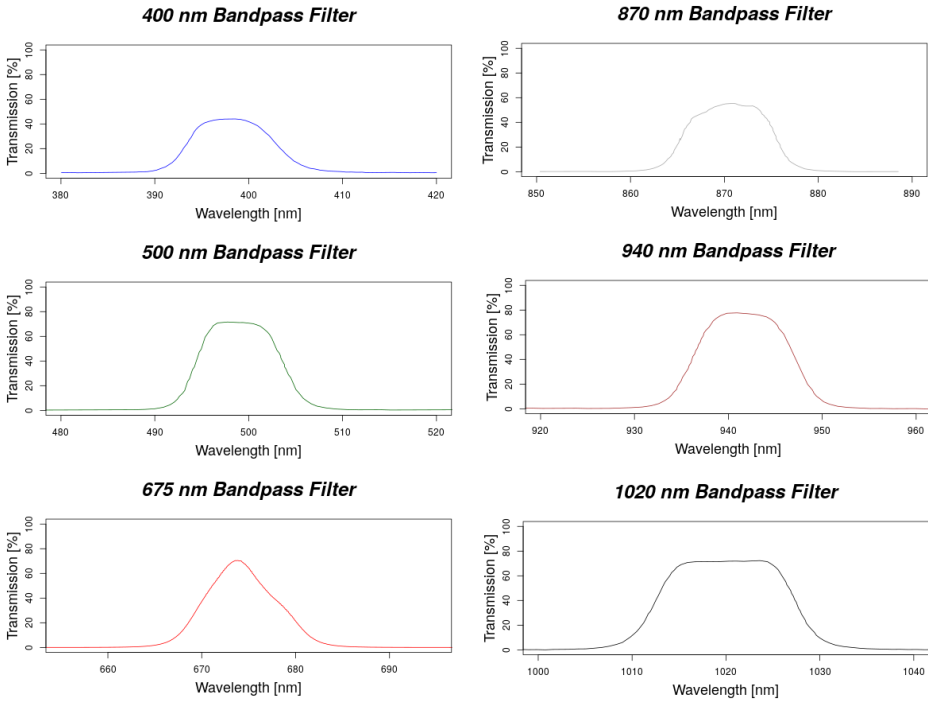can cross the pin-hole, while other directions are rejected. θ coincides with half the field of view. In the case of ARBOL, we have $f = 50mm$, $\varphi = 1mm$ and $\theta = 34'$, so the field of view is:

$$FOV = 2\theta = 1.1° \tag{2.2}$$

An accurate characterization of the telescope FOV is discussed in section 5.2.1.

A baffle d) reduces the stray light between c) and e) . Both d) and e) are precisely centered into an aluminum disk $34.9mm$ in diameter.

The LA1255 lens from "Thorlabs" is the telescope objective c). Its nominal focal length is $f = 50mm$. The optical windows a) are the WHP2511 from "Knight Optical". Finally, bandpass filters b) are the 400FIB25, 500DIB25, 675DIJ25, 870FIB25, 940DIB25 and 1020DIB25 from "Knight Optical" as well. The pinhole e) and the baffles d) are built ad-hoc. An aluminum slab 0.3 mm thick were etched chemically.

2.2.2   The Optics Housing

The telescope internal diameter is $35mm$. However, the window a), the filter b) and the lens c) have a smaller diameter ($25mm$), so a housing is used to mount the optics fixed inside the telescope. Figure 2.5a shows the housing and its design. This component fills the inner empty space between the telescope and the optics.

A couple of identical holders forms the housing (fig. 2.5a). The holder geometry is the following (fig. 2.5b):
- the external diameter is $34.9mm$.
- the internal diameter is $25.1mm$.
- the thickness is $9mm$
- a $2mm$ step imposes an entrance pupil of $21mm$.
Each holder cell hosts one or two optics. More precisely, two holders sandwich the window, the filter and the lens. A first O-ring lies between the window and the filter and a second is placed between the filter and the lens. The O-rings prevent the risk of breaking the optics. Both O-rings have a section of $1.78mm$ and an internal diameter $21.95mm$.

(a) A optics-housing opened   (b) Holder design (profile view)
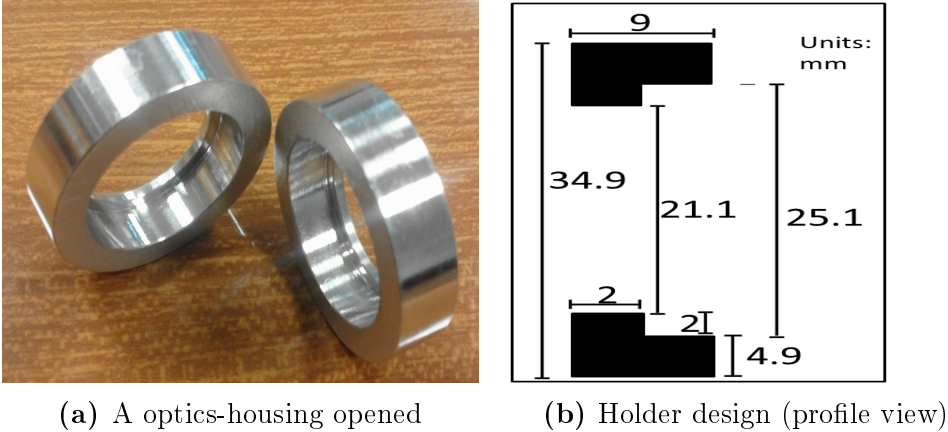
Figure 2.5

The O-ring sizes are chosen to make the O-rings act on the filter mount only. As a result, any pressure on the filter surface is avoided.

The optics-housing lies in the front of the telescope (see fig. 2.3).

2.2.3 PCB sizes

Here we describe the PCB mechanical details, while the next chapter will describe the electronics. There are two PCBs inside each of ARBOL telescopes. One of them contains the light sensor.

(a) Front side   (b) Back side
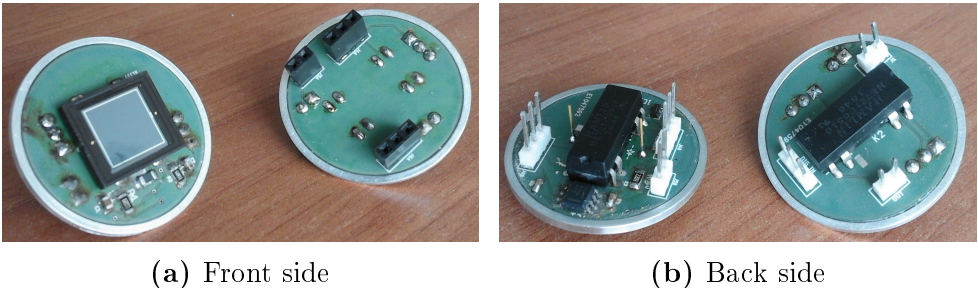
Figure 2.6. Assembled front-end PCB for ARBOL telescopes

Both PCBs are round disks with a diameter of $32mm$. An aluminum ring is glued to each PCB. Ring and PCB create a disk whose diameter is $34.9mm$. Thus, they match the telescope internal structure well. Both the PCB and the aluminum ring are $1.57mm$ thick.

The two PCBs must be connected together: hence, the light sensor PCB mounts proper board-to-board pin connectors. The headers are

22-03-2021 or 22-03-2031 from the 4030 series of "Molex". The other PCB mounts the corresponding sockets. They are the 2212S-03SG-85 or 2212S-03SG-85 models from the 2212S series of "Multicomp". Both headers and sockets are through-hole components with a standard $2.54mm$ pitch.

These connectors are ideal for the mechanical geometry of ARBOL, since they allow to stack the PCBs on top of each other. They create the electrical connection, but keep a distance greater than $10mm$ between PCBs, leaving enough space to mount components in there as well. Finally, the connectors allow an easy maintenance because it is simple to connect (or disconnect) the PCBs to each other.
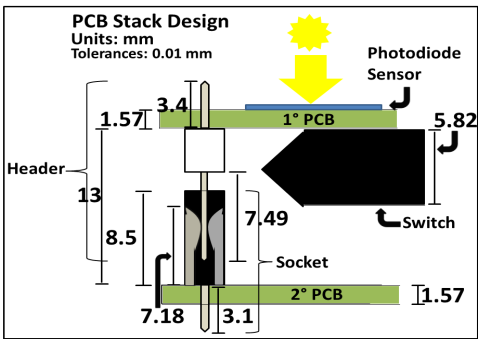
(a) PCB stack design
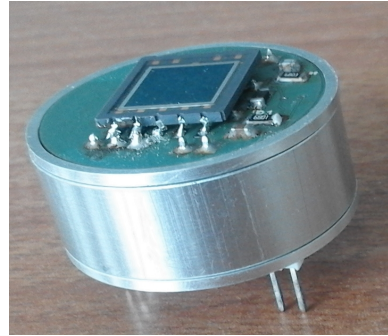
(b) 2 PCBs stacked togheter

Figure 2.7

A cylindrical section lies between the two PCBs (see fig. 2.7b). This section keeps a fixed distance between PCBs, thus avoiding any mechanical pressure on the board connectors.

2.2.4 The position of the pin-hole

The lenses of ARBOL are made of NBK-7 glass, whose refractive index depends on the wavelength (fig. 2.8). Their focal length is:

$$f(\lambda) = \frac{r_b}{n(\lambda) - 1} \qquad (2.3)$$

where r_b is the radius of curvature and $n(\lambda)$ the refractive index at wavelength λ. Eq. 2.3 states f changes with λ. For the LA1255 lens we have $r_b = 25.8mm$. The resulting $f(\lambda)$ are listed in table 2.1.

λ [nm]	f [mm]
400	48.5
500	49.4
1020	50.9

Table 2.1
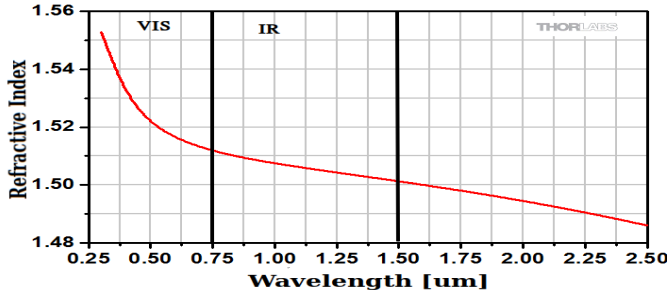
Figure 2.8. NBK-7 refractive index vs wavelength. Source:"Thorlabs".

We saw above that the pin-hole (e) must lie in the focal plane to limit the instrument FOV. If the lens–pin-hole distance x is not the correct one, the pin-hole cuts the incoming light beam.

Let's compute the precision we need to place the pin-hole correctly.

(a) Parallel beam

(b) Inclined beam
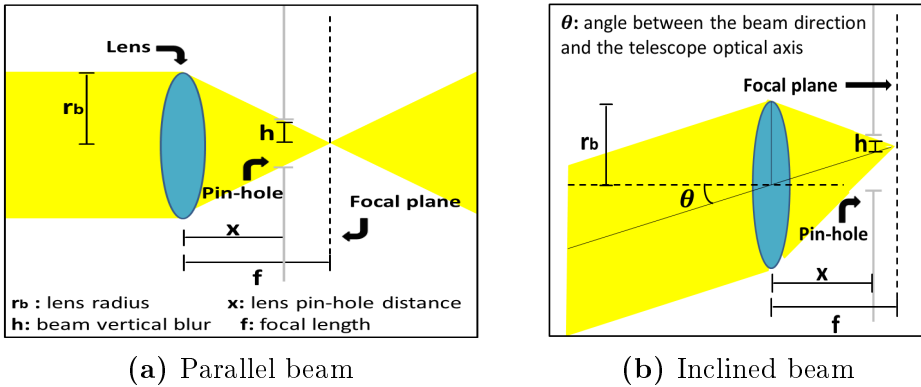
Figure 2.9. Lens–pinhole system

Considering figure 2.9,the pin-hole is $(f-x)$ distant from the actual focal plane (where h is half the beam vertical blur). We compute h as a function of the distance x. For the simple situation of fig. 2.9a we find:

$$h = (f - x)\frac{r_b}{f} \qquad (2.4)$$

20

However, we must consider inclined beams as well (fig. 2.9b). Let θ be the angle between the beam direction and the telescope optical axis. From trigonometry, we add a term in eq. 2.4 accounting for the incoming beam direction:

$$h = x tg(\theta) + (f - x)\frac{r_b}{f} \qquad (2.5)$$

We assume $\theta = 0.25$ degrees, half the angle subtended by the Sun in the sky. $\phi = 1mm$ is the pin-hole diameter. As long as the condition $h \leq \frac{\phi}{2}$ is fulfilled, the pin-hole doesn't cut the light beam. In this case, the positioning error is not critical. The cutting-beam limit is:

$$h = \frac{\phi}{2} \qquad (2.6)$$

Let the condition 2.6 be true. We evaluate the corresponding lens–pin-hole distance for two cases:
- if $x > f$. We call this limit x^+:

$$\frac{\phi}{2} = x^+ tg(\theta) + (x^+ - f)\frac{r_b}{f} \qquad (2.7)$$

- if $x < f$. We call this limit x^-:

$$\frac{\phi}{2} = x^+ tg(\theta) + (f - x^-)\frac{r_b}{f} \qquad (2.8)$$

x^- and x^+ set the precision we need to place the pin-hole and avoid the cutting beam effect. For example, for $\lambda = 400nm$ we have $f = 48.5mm$. Thus, $x^- = 47.4mm$ and $x^+ = 49.6mm$:

$$x = 48.5 \pm 1.1mm \qquad (2.9)$$

Let's compare the result of the eq. above and the focal lengths of table 2.1. $f(1020) = 50.9$ is outside the interval of distances in eq. 2.9. Accordingly, the length–pin-hole distances must differ among different wavelengths (i.e. different ARBOL telescopes).

We now compute the cylindrical section lengths to set the correct length–pin-hole distances.

First, the effective focal length f_b is retrieved. f_b accounts for the finite thickness of the lens. Thus, the lens–pin-hole distance x must coincide with f_b, not with f. For the LA1255 $d = 5.3mm$. f_b is:

$$f_b(\lambda) = f(\lambda) - \frac{d}{n(\lambda)} \qquad (2.10)$$

For example, we have $f(400nm) = 48.5mm$. The corresponding f_b is:

$$f_b(400nm) = 45mm \qquad (2.11)$$

Second, a baffle lies between the lens and the pin-hole. Its thickness is $0.3mm$ and its distance from the pin-hole is fixed at $11mm$. Moreover, the lens lies $2mm$ inside the optics-housing ($2mm$ is the holder step thickness, see sect. 2.2.2). Accordingly, we get the optics-housing–baffle section length SP:

$$SP(400) = f_b(400) - (11 + 2 + 0.3) = 31.7mm \qquad (2.12)$$

From the eq. above, if the optics-housing–baffle section is $31.7mm$ long, the actual focal plane and the pin-hole positions coincide.

We summarize the main results of the current section:
1) First, the lens–pin-hole distance differs for each wavelength. Thus, different cylindrical section lengths are necessary with different telescopes. Otherwise, the pin-hole cuts the light beam.
2) The optics-housing–baffle section (yellow in fig. 2.3) sets the correct lens–pin-hole distance. We retrieved $SP(400)$ here, but the same computation is made for each wavelength.

The next section summarizes the section lengths.

2.2.5 Overview of the telescopes

We give here an overview of the internal configuration of the telescopes. Figure 2.10 shows a schematic of the distances. The optics-housing is
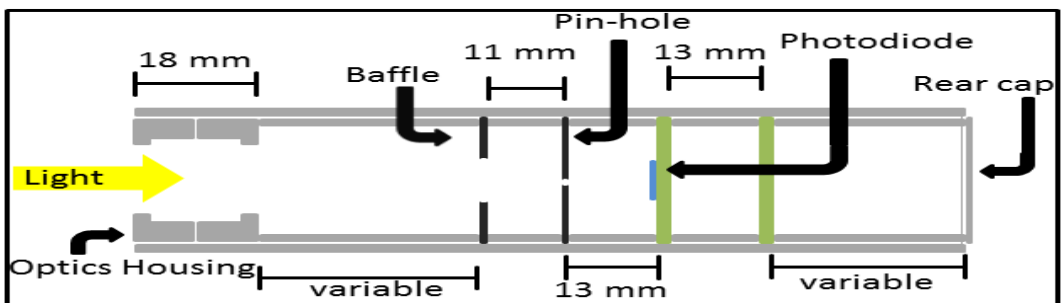
Figure 2.10. Inner axial distances inside the telescope. Units are in millimeters.

$18mm$ long. The cylindrical sections are:

1) the baffle–pin-hole section: $11mm$
2) the pin-hole–first PCB:$13mm$
3) the first PCB–second PCB:$13mm$

The lengths above doesn't change with wavelength. Instead, the optics-housing–baffle section length changes. Table 2.2 reports the length for each wavelength:

λ [nm]	f_b [mm]	Section length SP [mm]
400	45.0	31.7
500	45.9	32.6
675	46.7	33.4
870	47.2	34.0
940	47.3	34.0
1020	47.4	34.0

Table 2.2

Finally, the total length of sections and components must coincide with the telescope length ($130mm$, see above sect. 2.1). Thus, the rear sections lengths change with wavelength too, to compensate the variable length of the optics-housing–baffle section. We report here the rear section lengths:

λ [nm]	Rear section length [mm]
400	40.3
500	38.7
675	38.6
870	38.0
940	38.0
1020	38.0

Table 2.3

2.3   ARBOL cables and connections

ARBOL has a control unit to manage the power supplies as well as the signal acquisitions. It lies next to the main body of ARBOL, but out of it (see fig. 2.11b).In this section we describe the control unit dimensions as well as the cables used to acquire the signals of ARBOL. The control unit electronics is described in the next chapter.
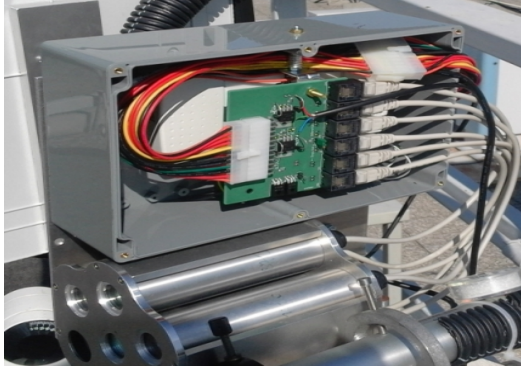
(a) Objects inside the control unit
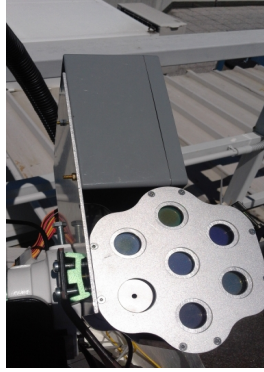
(b) ARBOL and the control unit screwed
on the slab

Figure 2.11

2.3.1 The control unit size and position

An aluminum slab mounts both the control unit box and the main
body of ARBOL (fig. 2.11b). The box position does not disturb the
tracker motion during operations. The box is the G3008 from "Multi-
comp". Its dimensions are $240mm$ x $90mm$ x $160mm$. There are two
objects inside the box: the "National Instruments" acquisition device
and the control electronic PCB (fig. 2.11a). See section 4.1 for more
details about the acquisition device. The electronic PCB manages the
signals:
- it receives the supplies from the power supply
- it delivers the supplies to each telescope of ARBOL
- it receives the analog signals from the telescopes of ARBOL
- it delivers the analog signals to the acquisition device
To manage the signals correctly, the control PCB mounts the following

connectors:
- six RJ45 connectors to connect with the telescopes
- an ATX connector for the connection with the power supply
- eight 22-23-2021 "Molex" pin headers to acquire signals with the acquisition device

Moreover, the control PCB accomplishes three electronic tasks, described in the next chapter (section 3.3).

2.3.2   The cables

Power supplies and signals must go to and come from the ARBOL telescopes. For each telescope there are:
- the two $\pm 9V$ power supplies
- the analog ground
- the measured light signal
- the measured temperature signal
- the $+5V$ digital signal
- the digital ground

TIA 568B Ethernet cables provide the electrical connections from the control unit to the instrument. A single cable can connect 8 signals and in our case there are 7 electrical signals for each telescope. Thus, one cable corresponds to one telescope (and serves only one wavelength). The cables are shielded and the wires inside are twisted into 4 pairs.

Inside each telescope, the ethernet cable is stripped and each of its wires mounts a proper wire-to-board connector. More precisely, each wire mounts:
- the 08-55-0124 "Molex" solderless terminal
- the corresponding 10-11-2023 or 10-11-2033 crimp housing

At the same time, the telescope rear PCB mounts the 22-03-2021 and 22-03-2031 headers. The latter are compatible with the wire connectors, thus the connection can be established.

Inside the control unit, RJ45 connectors receive the signals from the ethernet cables. The RJ45 terminals make the cable plug/unplug easy. A precise color coding governs the electric connections of ARBOL (we refer to the colors of wires inside the cable). Table 2.4 shows this color coding.

Wire Color	Type of signal
White-Orange	Dg_ground
Orange	$+5V$
White-Green	$-10V$
Blue	An_ground
White-Blue	Measured light signal
Green	$+10V$
White-Brown	To be left floating
Brown	Temperature signal

Table 2.4

Finally, cable glands 822-9675 from "RS Components" let the cable exit out of the telescope back, while at the same time granting the proper sealing of the telescopes.

2.4 Solar Tracking

To measure the direct normal irradiance, ARBOL must track the Sun. The current section describes the system responsible for the movements of the instrument.

The general idea to track the Sun is based on a feedback mechanism. This idea has already been tested within the master thesis of Dr. Marco Pallavera [32]. Moreover, Dr. Claudio Lucianaz (also involved into the GAIA project) has developed the software interface to control the tracker motors.

The feedback mechanism relies on the tracking telescope of AR-BOL. In the following subsections the mount, the tracking telescope and the software are described in details.

2.4.1 The Tracking Mount

ARBOL is fixed on a tracking mount. The latter is composed of a tripod and a mechanical body that can rotate along two orthogonal axes. In our case, the mount is an EQ3 from Sky-Watcher. This mount is a "german" equatorial type with two stepper motors that control one axis each. EQ3 is thought for amateur purposes, but we adapted it to our scientific aims.

In our case, a Raspberry PI3 controls the EQ3. An INDI server is installed on a Linux Ubuntu Mate operating system to communicate

Figure 2.12. An EQ3 tracking mount

Figure 2.13. The box containing ARBOL's power supply and the motor
controls

with the hand controller. First, the position to point is sent from the
PC to the hand controller. Afterwards, the mount points to it.

We operate the EQ3 in altazimuthal configuration. This configura-
tion has the advantage of allowing to use only one motor to span the
entire almucantar line (for more details about the almucantar measure-
ments see sect. 4.2.2). Thus, the almucantar sky radiance measure-
ments are simpler and faster.

A box hosts the control panel/motor board and the hand controller
cable (fig. 2.13). The hand controller is fixed outside of the box, ori-
ented northward so that the sunlight never hits the hand controller
during measurements. The box also contains the power supply of AR-
BOL and corotates with the instrument. For this reason, the power
supply cable as well as the motor cables don't twist.

Finally, the motor power supply is separated from the power supply
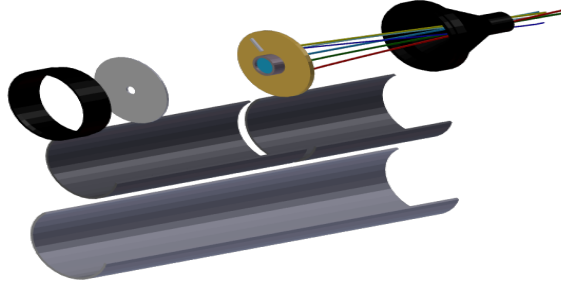
Figure 2.14. Internal view of the tracking optical unit. Image taken from Marco Pallavera master thesis [32]

of ARBOL. While this solution is not the most compact, splitting the supplies definitely improves the sensor performances of the instrument.

2.4.2   The tracking optical unit

We now describe the tracking telescope of ARBOL, whose measurements determines the tracking feedback.
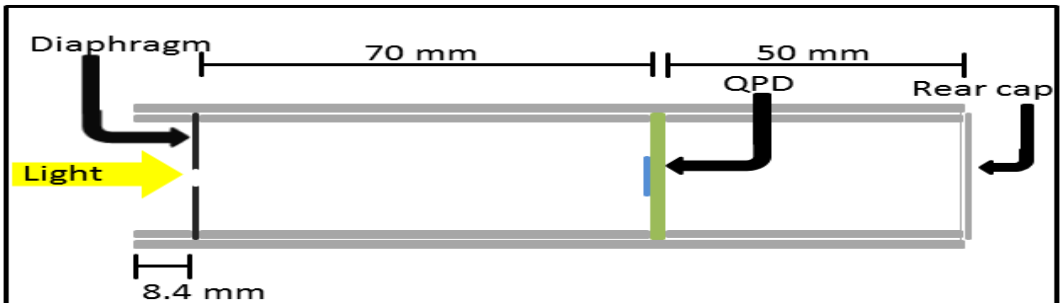
Figure 2.15. Inner axial distances inside the tracking telescope.

The telescope structure is simpler than the other telescopes. The following elements are stacked on top of each other (lengths are in the telescope axis direction):
- a cylindrical section $(8.4mm)$
- a diaphragm $(0.3mm)$
- a cylindrical section $(70mm)$
- a PCB $(1.57mm)$
- a cylindrical section $(50mm)$
- a rear cap
The above lengths sum up to $130mm$, which is the axial length of
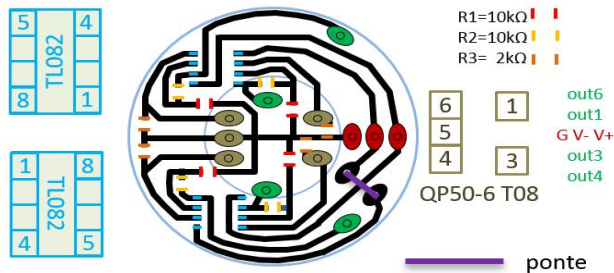
Figure 2.16. Circuit layout. Image taken from Marco Pallavera's master thesis [32]

the ARBOL telescopes. Thus, the tracking telescope can be mounted between the flanges of ARBOL.

The impinging light meets first the diaphragm, which imposes the field of view amplitude. Its diameter is $4mm$. The PCB-diaphragm distance is $70mm$. Consequently, the field of view is:

$$\theta = tg^{-1}\left(\frac{2}{70}\right) \simeq 1.6° \tag{2.13}$$

The PCB is a disk ($1.57mm$ thick) whose diameter is $35mm$. The PCB mounts a four quadrant silicon photodiode (QPD). The QPD center precisely intersects the telescope axis.

We briefly describe the PCB electronics to let the reader understand the tracking mechanism. Each quadrant of the QPD is connected to a preamplifier (see fig. 2.16). The latters are non-inverting transimpedance amplifiers. They lie on the lower disk face, while the upper face mounts the QPD (which in our case is the QP50-6 T08 from "First Sensor").

An ethernet cable takes the QPD signals to the Raspberry PI3. The ADS1115 ADC (resolution 16–bits) digitalizes the voltages and the Raspberry acquires them.

A python software controls the tracking feedback. Let's name each quadrant voltage signal after the corresponding cardinal point: North-West (NW), North-East (NE), South-East (SE), South-West(SW). The Sun is in the field of view center if the quadrant signal differences are minimized:

$$(NW + NE) - (SW + SE) \tag{2.14}$$

for the height direction, and:

$$(NW + SW) - (NE + SE) \tag{2.15}$$

29
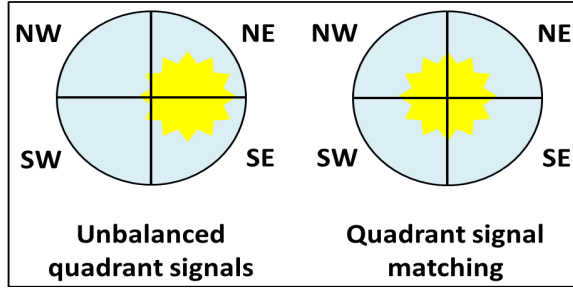
Figure 2.17. Left: situation where quadrant signals do not match. Right: quadrant signal matching

for the azimuth one. When the Sun moves, the result of eq. 2.14 (or eq. 2.15) becomes bigger than the tolerance threshold. In this case, the software activates the motor to correct the alignment: this is the feedback mechanism. The software checks differences 2.14 and eq. 2.15 once every second. The system has proven to be able to track the Sun from sunrise down to sunset without any problem.

We briefly report a mechanical problem of the tracking telescope and its solution. The photodiode quadrants are separated by two blind lines that can rotate around the telescope axis. If these lines are not correctly aligned with the cardinal points, the feedback algorithm does not work properly and eventually fails tracking the Sun. Thus, the inner PCB must be mounted correctly inside the telescope. Marco Pallavera reported that a precision $\pm10°$ allows the correct working of the solar tracking. As the required precision is not too high, we employed a hand-made solution. We simply glued the PCB, the $50mm$ cylindrical section and the rear cap together. Moreover, the directions of the QPD separators were drawn on the rear cap. With this solution we can control the QPD separator direction from outside the telescope. Tests have shown this solution solves the problem.

2.5   Acronyms in chapter 2

Acronym	Meaning
PCB	Printed Circuit Board
QPD	Quadrant PhotoDiode
ADC	Analog-to-Digital Converter
FWHM	Full Width at Half Maximum
INDI	Instrument Neutral Distributed Interface

Electronics Layout

3.1 Light detection and signal amplification: the front end electronics

3.1.1 Overview

Each telescope in ARBOL has got a photodiode sensor and pre-amplification electronics. The preamplifier provides two different signal gains to extend the dynamical range, and the proper gain value is selected by a relay. The latter can be software controlled with a digital signal. After preamplification, the measurement is sent to the acquisition system, digitized and acquired on a PC.

Temperature variations of the photodiode can change its photosensitivity. The signal can be corrected, provided the photodiode temperature is known (see sect. 5.2.2). Accordingly, each front-end PCB is given a thermistor and the temperature is monitored.

Both the preamplifier and the thermistor circuitry are designed ad hoc and they will be described in the following sections.

3.1.2 Photodiode Sensors

ARBOL has got two different sensor types. The photodiode S5107 [39] is used with 500nm, 675nm and 870nm spectral channels; the photodiode S1337 [41] is used with 400nm, 940nm and 1020nm. They are both from Hamamatsu.

Some specs are common:
- both the photodiodes are silicon based
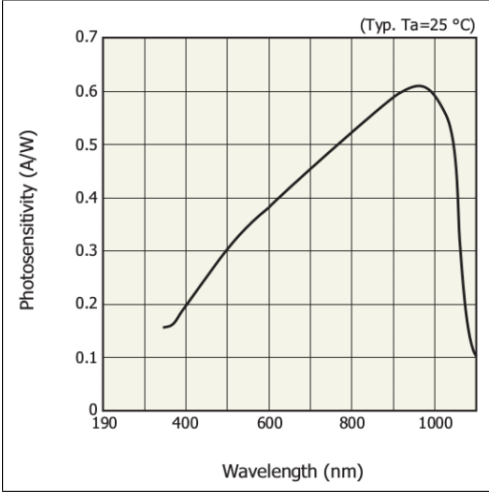
(a) S1337 spectral response.[41]
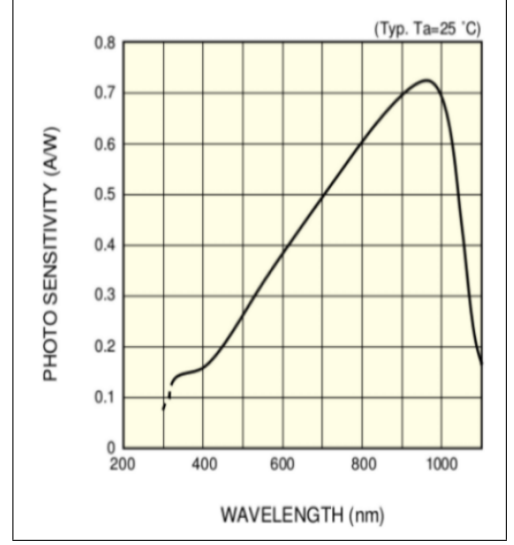
(b) S5107 spectral response.[39]

Figure 3.1. Comparison between S1337 and S5107 spectral responses. T=25°C.

- the spectral response is from 320/340nm up to 1100nm, with a sensitivity peak at 960nm.
- the sensible surface is squared, $1cm^2$ wide.

There are some differences in the spectral response curve (fig. 3.1). For istance, the S5107 curve is narrower and more effective between 600 and 1100nm.

The most important difference is the temperature coefficient (fig. 3.2): the bigger this coefficient, the more the photosensitivity is affected by temperature variations. Figs. 3.2a and 3.2b show the photodiode S1337 is less affected by temperature changes.

For example, let's consider the 1020nm channel. For the sake of simplicity, let's average the curves 3.2a and 3.2b between 1010 and 1030 nm. This range is the spectral window of the 1020nm bandpass filter. For the S1337 photodiode the temperature coefficient is:

$$\frac{dS_{1020}}{dT}^{S1337} = 0.29\frac{\%}{C} \tag{3.1}$$

while the S5107 reveals:

$$\frac{dS_{1020}}{dT}^{S5107} = 0.53\frac{\%}{C} \tag{3.2}$$

32
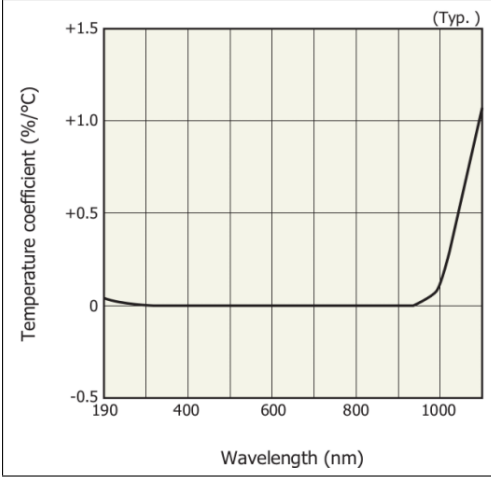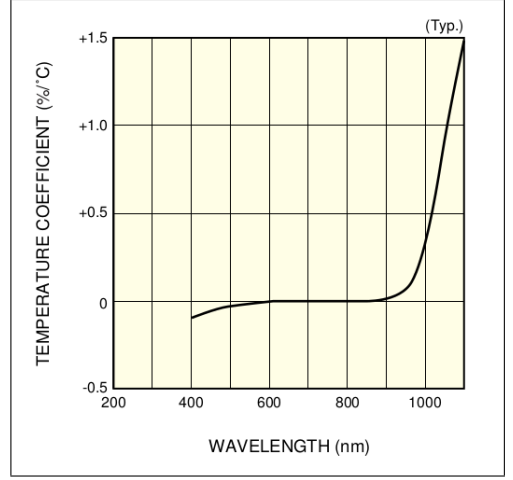
(a) S1337[41] (b) S5107[39]

Figure 3.2. Comparison between S1337 and S5107 photosensitivity temperature coefficient

The former sensor halves the fractional variation. We can conclude the photodiode S1337 is more suited for 1020nm. The same can be shown for 400nm and 940nm.

By contrast, the other channels are not affected by temperature at all. For these wavelengths the more sensitive S5107 is used.

Section 3.2 describes the temperature effects on photocurrent.

3.1.3 Photodiode linearity and transimpedance amplifier circuit

The preamplifier electronics is based on the transimpedance amplifier circuit (TIA hereinafter). A simplified scheme is shown in fig. 3.3. The schematic diagram presents two important characteristics:
- the sensor is a photodiode and it is used in photovoltaic mode.
- an op-amp and the negative feedback provide the current to voltage conversion and the necessary signal amplification.

The photovoltaic mode is suited for precision application. The photodiode is grounded and no voltage bias is applied. Consequently, there is no dark current and the noise level is lowered (e.g. see [54] and [52]).

The feedback resistor R_{fd} provides the transimpedance DC gain,

33
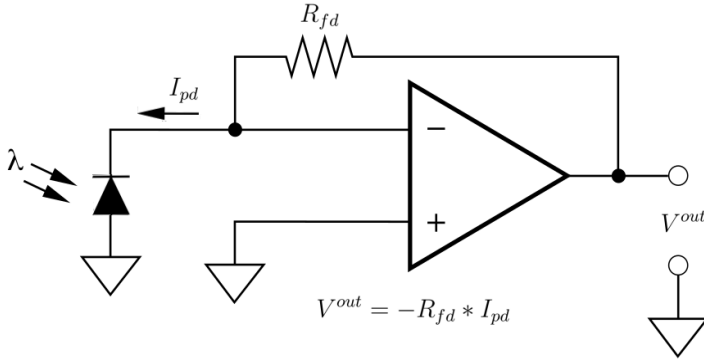
Figure 3.3. An example of transimpedance amplifier.

while the feedback capacitor (not shown) guarantees the circuit stability. Ohm's law relates the photocurrent to the output voltage:

$$V^{out} = -R_{fd} \times I_{pd} \tag{3.3}$$

where I_{pd} is the photocurrent. The transimpedance gain is:

$$G \equiv \frac{V^{out}}{I_{pd}} = -R_{fd} \tag{3.4}$$

The presence of the op-amp helps extending the photodiode linear range. The following equation describes the circuit saturation limit (eq. (4) from [52]) :

$$P_{sat} = \frac{V_{bi}}{(R_s + R_{pd}^{in}) \times S_\lambda} \tag{3.5}$$

Here P_{sat} is the saturation power, V_{bi} the contact voltage (from 0.2 to 0.3 V for silicon photodiodes), R_s the series resistance and S_λ the sensitivity of the photodiode. Finally, R_{pd}^{in} is the TIA equivalent input resistance.

The op-amp based TIA exploits the op-amp properties to make the photocurrent see a very low R_{pd}^{in}. This fact is briefly shown.

Let A be the op-amp open loop gain, V^+ and V^- the non-inverting and inverting op-amp input nodes. V^+ is grounded. We can write:

$$V^- = \frac{-V^{out}}{A} = \frac{R_{fd} \times I_{pd}}{A} \tag{3.6}$$

34

Eq. 3.3 has been employed to replace V^{out} with the product. The TIA input resistance is then:

$$R_{pd}^{in} = \frac{V^-}{I_{pd}} = \frac{R_{fd}}{A} \qquad (3.7)$$

where V^- has been substituted according to the 3.6. The photodiode load R_{pd}^{in} is A^{-1} times smaller than R_{fd}. In the case of ARBOL, we have:

$$A = 10^7 \qquad (3.8)$$

Thus, the equivalent input resistance is not greater than 1Ω even if $R_{fd} = 10^7\Omega$.

Let's consider again eq. 3.5. R_s is the resistance of the silicon and the bonds of the photodiode (generally $R_s \sim 10\Omega$, [43]). We neglect R_{pd}^{in} ($\sim 1\Omega$) and we find $P_{sat} \simeq 40mW$. This is the photodiode linearity limit. The linearity range of the photodiode is kept extremely large because R_{pd}^{in} is small.

3.1.4 TIA components, front end architecture

A detailed description of ARBOL front-end circuit is given here. Figure 3.4 shows the schematic. The circuit can amplify either the S1337 or the S5107 photodiode current.

The photocurrent dynamic range is very extended (from $I_{pd}^{max} \simeq 1mA$ down to $I_{pd}^{min} \simeq 10nA$). The current must be converted into voltage and acquired. The voltage must be between $10V$ and $0.01V$ for the signal acquisition. The conversion task is not trivial. The wider current range must be mapped into a tighter voltage range.

The solution is based on two different gain values. The two gains cover the whole current range. The higher gain observes the weak skylight, the lower gain the strong sunlight. Thus, the proper current-to-voltage conversion is granted. The circuit design provides a loop for each gain value. The reed relay HEC721 [45] redirects the signal photocurrent towards the correct loop.

Both the loops follow the TIA circuit structure (see above, sect. 3.1.3). The maximum output voltage must not exceed the voltage supply ($V_{sup}^{\pm} = \pm 9V$) to avoid signal clipping. The low gain resistance R_1 is chosen accordingly:

$$V^{max} = R_1 \times I_{pd}^{max} \simeq 6.8V < V_{sup}^+ \qquad (3.9)$$
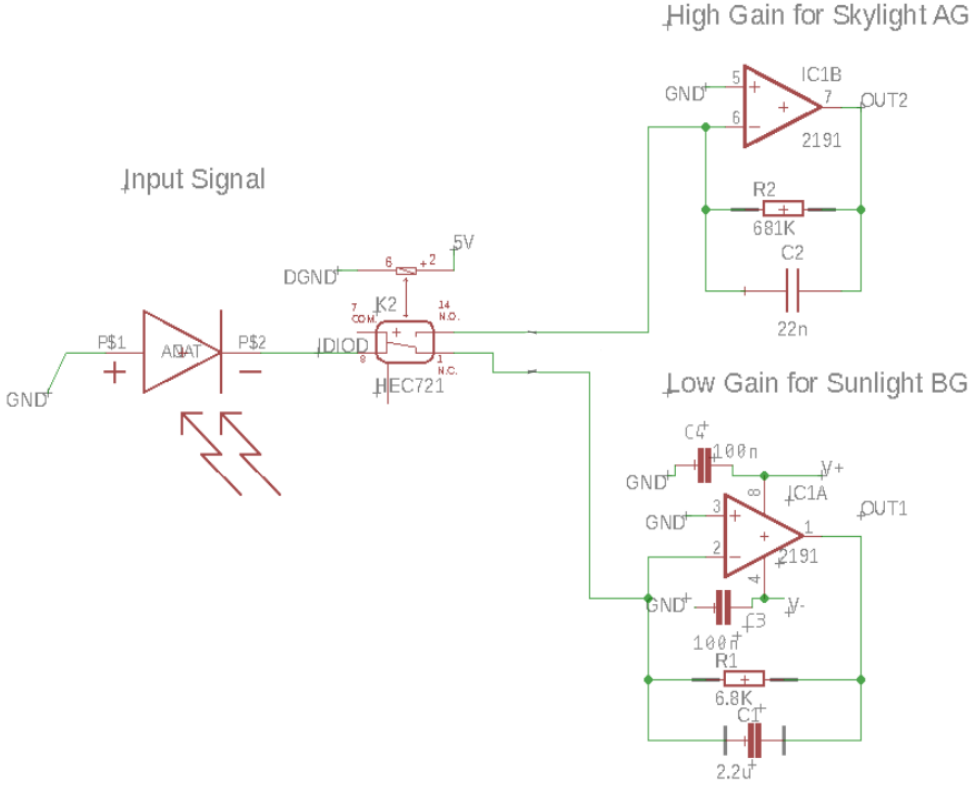
Figure 3.4. Front end schematic for the light measuring circuit.

The feedback capacitor is $C_1 = 2.2\mu F$. The value of C_1 limits the circuit bandwidth (see below, the next section). For the high gain loop we have $R_2 = 680k\Omega$ and $C_2 = 22nF$. R_2 and C_2 values might change in the future because the gain value retrieval is not complete yet (sect. 5.1.2).

The low gain loop detects photocurrents as small as $I_{pd} \simeq 1\mu A$. For smaller currents the high gain is necessary. The high gain measures currents as large as $I_{pd} \simeq 10\mu A$. Both the loops observe currents between $1\mu A$ and $10\mu A$. The range overlap allows the intercalibration between different gain acquisitions.

We discuss now the characteristics of the circuit components.

HEC721 is a single-pole-double-throw reed relay. A $+5V$ digital signal controls the relay status. The relay preserves the TIA perfor-

mances for two reasons:
- it introduces no leakage currents
- it presents a low resistance across terminals ($R_{rel} = 0.2\Omega$)

HEC721 is electromechanical and it introduces no leakages. Leakage currents add up to the photocurrents in the inverting op-amp input node, where they are amplified and generate biases in the output voltages. Avoiding leakages improves the circuit output accuracy.

A low R_{rel} preserves the photodiode linear range. The photodiode load is given by the series resistance:

$$R_{load} = R_{pd}^{in} + R_{rel} \tag{3.10}$$

where R_{pd}^{in} is the TIA equivalent input resistance (see previous section). R_{load} substitutes R_{pd}^{in} in eq. 3.5. The lower R_{load} is, the higher P_{sat}. Accordingly, a low R_{rel} helps preserving the photodiode linear range.

OPA2191 [37] from Texas Instruments is the circuit op-amp. The device is a CMOS type and it is dual: a small package (SOIC8) contains two amplifiers. OPA2191 offers very good performances:
- a low input offset voltage (typically $10\mu V$)
- a low input offset voltage drift ($0.15\ \frac{\mu V}{^\circ C}$)
- a small input bias current (few pA, much smaller than the minimum expected photocurrent, $10nA$)
Bias currents add up to the photocurrents in the inverting op-amp input node. CMOS op-amps offer low bias input current levels. For this reason, they are ideal for transimpedance application.
The temperature affects OPA2191 very little because the offset voltage drift is low. ARBOL makes measurements in the outdoor, where temperature can change a lot. OPA2191 temperature stability improves ARBOL performances.

From an AC point of view, the OPA2191 noise is extremely low:
- input voltage noise density is $e_n = 15nV/\sqrt{Hz}$
- input current noise density is $i_n = 1.5fA/\sqrt{Hz}$

OPA2191 has a DC gain $A = 10^7$ and a gain-bandwidth product $GBW = 2.5MHz$. Accordingly, there's a pole at $f_p = 0.25Hz$. Finally, OPA2191 is supplied with a $\pm 9V$ dual supply. The large supply range allows a large output voltage range.

Other op-amps were considered and discarded, because OPA2191 fulfills all the requirements listed above, while the other op-amps only met some of them. For example, bipolar OP270 is dual but it has too

high bias currents. LTC6268 is fine with transimpedance applications, but the maximum dual supply range is $\pm 2.5V$. OPA145 lacks a dual op-amp package. Finally, AD8626 has a higher GBW product, which means the output noise is higher (see the next section).
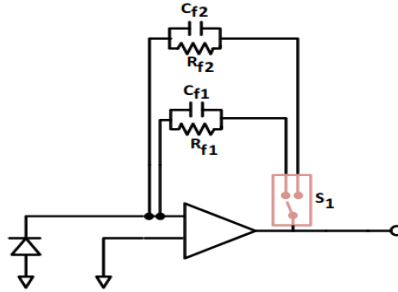
Figure 3.5. Programmable gain TIA as suggested by Orozco [27]
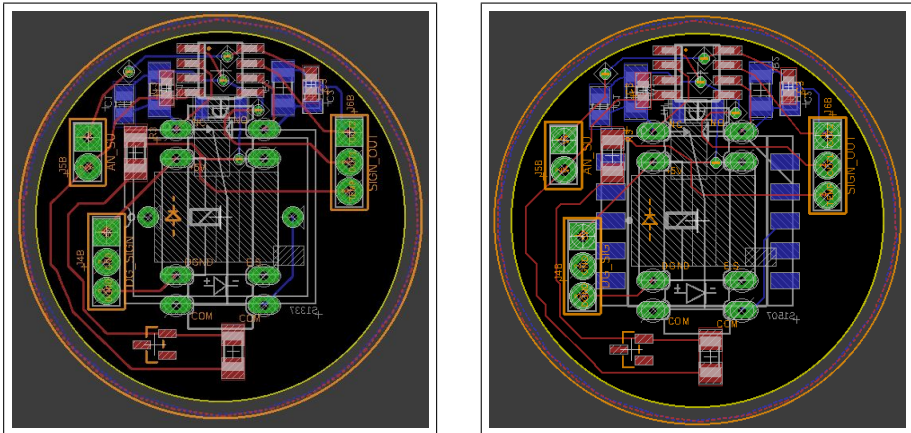
(a) PCB carrying S5107 photodiode

(b) PCB carrying S5107 photodiode

Figure 3.6. Eagle PCB designs

Different circuit diagrams were considered as well. For example, Orozco [27] suggests a programmable gain TIA with a double feedback loop (fig. 3.5). We can compare it with the circuit in figure 3.4. The latter enjoys two benefits:
- the relay is outside the feedback loop
- consequently, no relay resistance is added into the feedback loop
In the circuit in figure 3.5, the op-amp saturates every time S_1 changes the gain, because the feedback loop is broken. In figure 3.4, when the

relay disconnects the current input the voltage output simply drops. This circuit preserves the op-amp stability. Moreover, no relay resistance into the feedback loop means no offset errors into the TIA gain value.

For these reasons, the electronic design in figure 3.4 was preferred.

The Eagle ecad software was employed to design the PCB boards (figs. 3.6a and 3.6b). A circular disk hosts the preamplifier and the temperature monitoring circuit (described in section 3.2). Its diameter is 32 mm long. The photodiode lies on the top side, towards the impinging light. On the opposite side there are the relay as well as the op-amp and passive components.

3.1.5 AC analysis

The TIA output voltage noise floor is computed in this section.

Figure 3.7 shows the photodiode equivalent circuit [35]. The parallel among an ideal current source, a shunt resistance R_{sh} and a terminal capacitance C_t replaces the photodiode. C_t is about 700 pF for S5107, 1100 pF for S1337. R_{sh} corresponds to the slope of the photodiode I-V characteristic between $\pm 10mV$. It ranges from 10's to 1000's Mega Ohms [49]. For instance, S1337 datasheet states a $200M\Omega$ value.

OPA2191 common mode input capacitance ($C_{IC} \sim 5pF$) and differential input capacitance ($C_{ID} \sim 1pF$) are neglected because they are in parallel with C_t.

C_{fd} and R_{fd} can be either $C_1 = 2.2\mu F$ and $R_1 = 6.8k\Omega$ for the low gain loop or $C_2 = 22nF$ and $R_2 = 680k\Omega$ for the high gain loop.

The bulletin [48] from Texas Instruments is followed to compute the total output noise.

Both current and voltage input noise densities generate output voltage noise. The current noise sources are:
- the op-amp generated current noise density i_n
- the photodiode shot noise density, i_s
- the feedback resistor thermal noise. A current source i_R in parallel with an ideal noiseless resistor models this kind of noise.

The only voltage noise source is the op-amp noise density, e_n.

Let E be the output referred noise root mean square. For the current sources, we have:

$$E = \sqrt{i^2(|T(\omega)|^{max})^2 GBW_i} \tag{3.11}$$

In eq. 3.11 i can be any of the current densities listed above. $T(\omega)$ is the
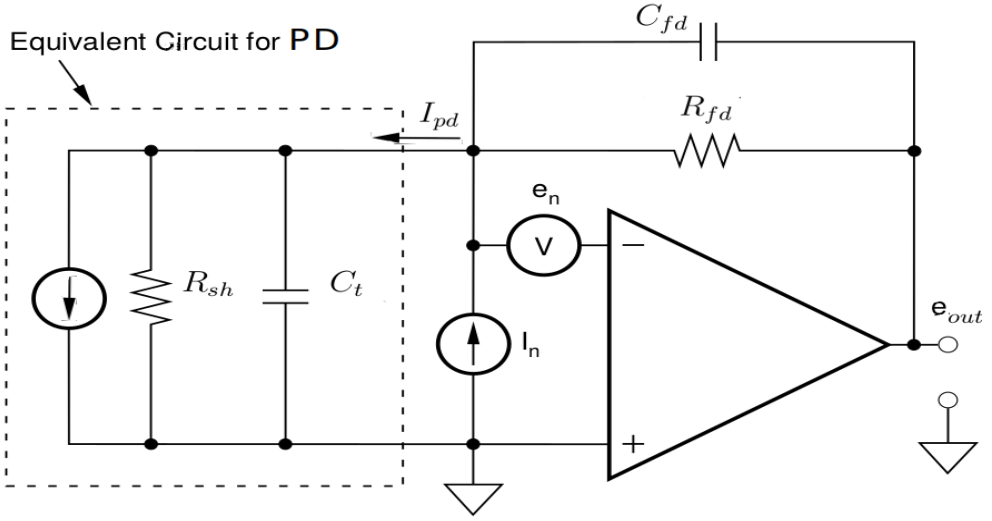
Figure 3.7. Equivalent TIA circuit for small signals

complex transimpedance gain, GBW_i the equivalent noise bandwidth. C_{fd} and R_{fd} form a first order low pass filter for the input current. Accordingly, $T(\omega)$ is:

$$T(\omega) = \frac{R_{fd}}{1 + j\frac{\omega}{\omega_p}} \qquad (3.12)$$

where j is the imaginary unit, ω_p the pole corner frequency:

$$\omega_p = \frac{1}{2\pi R_{fd}C_{fd}} \qquad (3.13)$$

From the 3.12 follows $|T(\omega)|^{max} = R_{fd}$, the DC value. The equivalent noise bandwidth is (see [47]):

$$GBW_i = \frac{\pi}{2}\omega_p \qquad (3.14)$$

For both the gain loops the feedback resistor R_{fd} optimizes the DC gain value, while C_{fd} fixes the pole frequency so that:

$$\omega_p \simeq 10Hz \Rightarrow GBW_i \simeq 17Hz \qquad (3.15)$$

ARBOL does not need fast measurements and GBW_i can contain only low frequencies. At the same time, a small GBW_i reduces the output noise.

40

OPA2191 input current noise density is $i_n = 1.5 fA/\sqrt{Hz}$. Thus, inserting values into eq. 3.11 for the high gain loop ($R_{fd} = R_2$) we get:

$$E_{in} = \sqrt{i_n^2 R_2^2 GBW_i} = 4.2nV \qquad (3.16)$$

E_{in} is small. The op-amp input current noise is negligible.

We now consider photodiode shot noise density, i_s, that depends on the photocurrent intensity:

$$i_s = \sqrt{eI_{pd}} \qquad (3.17)$$

where e is the electron charge, expressed in Coulomb. Figure 3.8 shows i_s in the sub-micron current range. There is no need to consider stronger currents, because in that case the signal overcomes the noise.
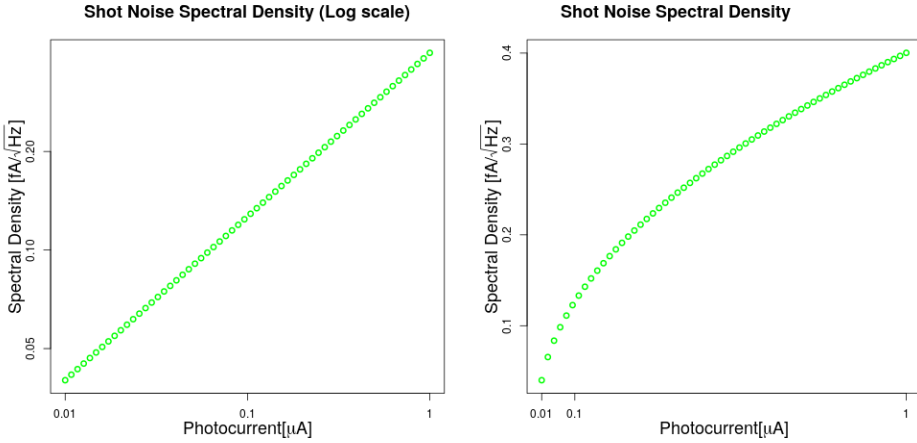
Figure 3.8. Shot noise spectral density i_s. On the left there's the log-log plot for the same quantity

From 3.8 it follows that i_s is smaller than i_n. Assuming $I_{pd} = 10nA$ ($\Rightarrow i_s = 0.04 fA/\sqrt{Hz}$) the output voltage noise due to shot noise is:

$$E_{is} = \sqrt{i_s^2 R_2^2 GBW_i} = 0.1nV \qquad (3.18)$$

The shot noise is small too.

Finally, R_2 thermal noise is analyzed. A current source in parallel with a noiseless resistor models R_2 and the noise density is:

$$i_R = \sqrt{\frac{4kT}{R_2}} \qquad (3.19)$$

Here k is the Boltzmann constant, T the absolute temperature. For $T = 298.15K$, we have $i_R = 0.15pA/\sqrt{Hz}$. The output noise is:

$$E_R = \sqrt{i_R^2 R_2^2 GBW_i} = 0.4\mu V \tag{3.20}$$

The latter is the biggest noise contribute among the input current noise sources, but still it is quite small.

Equations 3.16, 3.18 and 3.20 consider only the high gain loop. Computation for the low gain loop is not necessary: in this case, E_{in}, E_{is} and E_R are even smaller because R_1 is smaller than R_2.

Finally, we consider the op-amp input voltage noise source, e_n. The output noise root mean square E_{en} is:

$$E_{en} = \sqrt{e_n^2 (|NG(\omega)|^{max})^2 GBW_e} \tag{3.21}$$

By definition, the noise gain $NG(\omega)$ amplifies a voltage source connected with an op-amp input (see [53]). GBW_e is the corresponding equivalent noise bandwidth. The gain coincides with $NG(\omega)$ for both V_{os} (the DC input offset voltage) and e_n. The following equation describes $NG(\omega)$ for a transimpedance amplifier circuit:

$$NG(\omega) = 1 + \frac{Z_{fd}(\omega)}{Z_{pd}(\omega)} \tag{3.22}$$

Z_{fd} is the parallel combination between R_{fd} and C_{fd}; Z_{pd} is the parallel between R_{sh} and C_t. Substituting impedance factors we find:

$$NG(\omega) = \frac{1 + j\omega R_{fd} C_{fd}}{1 + j\omega R_{fd}(C_{fd} + C_t)} \tag{3.23}$$

In equation 3.23 R_{sh} is neglected because $R_{sh}^{-1} \ll R_{fd}^{-1}$. Moreover, C_t can be neglected as well ($C_t \ll C_{fd}$). Accordingly, the noise gain is:

$$NG(\omega) = 1 \tag{3.24}$$

Equation 3.24 states the TIA circuit does not amplify an input voltage. NG does not depend on frequency and GBW_e coincides with OPA2191 open-loop bandwidth. It ends up to [37]:

$$GBW_e = 2.5MHz \tag{3.25}$$

The OPA2191 input-referred spectral density is $e_n = 15nV/\sqrt{Hz}$. The corresponding output voltage noise is:

$$E_{en} = \sqrt{e_n^2 NG^2 GBW_e} = 23.7\mu V \tag{3.26}$$

The latter noise source determines the total output noise level of the circuit:

$$E_{an} = \sqrt{E_{en}^2 + E_R^2 + E_{in}^2 + E_{is}^2} = 24\mu V \simeq E_{en} \qquad (3.27)$$

Both the gain loops have the same noise level. Equations 3.26 and 3.27 are valid for both because:
- the op-amp is the same
- the following inequalities hold:

$$C_t \ll C_1; R_{sh}^{-1} \ll R_1^{-1} \qquad (3.28)$$

for the low gain, and:

$$C_t \ll C_2; R_{sh}^{-1} \ll R_2^{-1} \qquad (3.29)$$

for the high gain.

3.1.6   An important TIA benefit

The op-amp DC input offset voltage (V_{os}) sees a unity gain in the TIA circuit because $NG(\omega) = 1$. For both the high and low gain loops, V_{os} reaches the output node unchanged and is thus negligible. ($V_{os} = \pm 10\mu V$)

By contrast, different circuit designs amplify V_{os}. For example, the circuit of figure 3.9 was tested. Two stages are cascaded in this circuit: first a low gain TIA, then an inverting amplifier. The second stage provides the extra-gain for low light levels. In this case, V_{os} is not negligible. The measured signal and the TIA offset reach node V_{out1} as voltages. For low light levels, the former can be as small as the latter, or even smaller. The second stage makes no distinction and amplifies them both. Consequently, V_{os} and the measured signal are comparable in amplitude at the V_{out2} output.
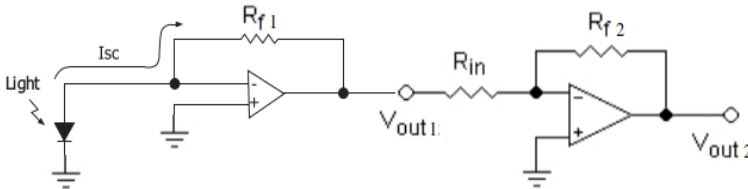
Figure 3.9. Scheme of the prototype circuit used during the measurement tests.

A significant offset is a critical problem because it can drift: for example, V_{os} drifts with temperature ($\frac{dV_{os}}{dT} = 0.15\frac{\mu V}{°C}$), but other kinds of drift were observed too. V_{os} drifts introduce systematic errors into the measurement and thus a real-time monitoring of V_{os} is necessary to make accurate light measurement.

The circuit of figure 3.4 is based only on the TIA circuit scheme. The TIA distinguishes the input offset voltage from the input signal photocurrent. The latter is amplified, but V_{os} and its drifts are kept small and so the offset monitoring is not necessary; moreover the circuit design is simpler. For these reasons, the circuit of figure 3.4 was preferred.

3.1.7 Managing high and low gain

A second HEC721 relay (S_2 in fig. 3.10) reduces the number of ouput voltage channels from two to one. The relay receives the output voltage from both the gain loops and switches between them properly. The same digital signal controls both S_1 and S_2, so the two are synchronized. For spatial reasons, S_2 lies on a second PCB. The two PCBs can be stacked (see sect. 2.2.3).
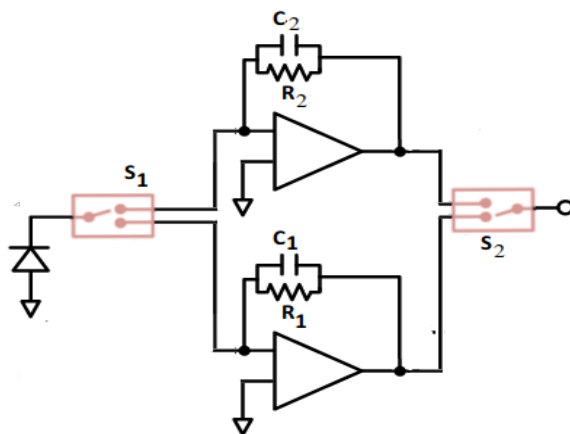
Figure 3.10. Simplified ARBOL front-end circuit scheme

Each telescope in ARBOL has got the same front-end circuit design. Accordingly, the light measuring outputs are six, one for each spectral channel. The total number of relays is 12 per instrument. The same $+5V$ digital signal switches all of them concurrently.

3.2 Temperature monitoring

ARBOL operates outdoors. The temperature change can be sharp and pronounced: during morning time temperature can increase by more than $\sim 15°C$ in a few hours. The temperature variations affect the instrument electronics and thus must be monitored.

The temperature monitor system is described here. In section 5.2.2 temperature corrections will be applied to data.

3.2.1 The precision required to measure temperature

Temperature affects the electronics and causes the following effects:
- changes to the resistance values
- changes to the photodiode sensitivity
Moreover, the current flow causes the resistor self-heating effect.

OPA2191 offset thermal drift is ignored here, since it was shown above to be negligible. (sect. 3.1.4 and 3.1.6)

First, let's analyze changes of the resistance values due to temperature.

$\alpha = 100\frac{ppm}{°C}$ is the temperature coefficient for both R_1 and R_2, the feedback resistors, and their resistance values depend on temperature through the following:

$$R(T) = R(25°)(1 + \alpha(T - 25°)) \tag{3.30}$$

In terms of the relative resistance change, we have:

$$\frac{\Delta R}{R(25°)} = \alpha \Delta T \tag{3.31}$$

Let's assume a diurnal temperature change $\Delta T_{day} = 10°$ and a seasonal change $\Delta T_{year} = 30°$. The relative resistance change is obtained for ΔT_{year}:

$$\frac{\Delta R}{R(25°)} = 0.003 \tag{3.32}$$

The corresponding percentage variation is 0.3%. During a day the percentage variation is even smaller: 0.1%.

The resistor sensibility to temperature is low and the resistance change due to temperature oscillations is not critical.

We consider now the self-heating effect, which is caused by the current flow in the resistor.

The low gain loop faces the strongest photocurrent, because the sunlight is the most intense to measure. We compute the power dissipated into the low gain feedback resistance, R_1. We ignore R_2 (the high gain) because skylight photocurrents are smaller. The expected maximum photocurrent is a few mA ($I_{pd} \sim 2 - 3mA$), $5 - 6V$ the corresponding applied voltage. Thus, R_1 dissipates almost 20 mW:

$$P_{diss} \sim 18mW \qquad (3.33)$$

The self-heating coefficient of R_1 is $\theta_{sh} = 2.9\frac{mW}{^\circ C}$. The resistor heating is given by:

$$\Delta T_{sh} = \frac{P_{diss}}{\theta_{sh}} \sim 6^\circ C \qquad (3.34)$$

The temperature variation is small. The self-heating does not change the resistance value of R_1. This effect is not critical.

Last, the temperature can change the photodiode sensitivity and bias the measured light signal. Among the spectral channels of AR-BOL, only the $1020nm$ is affected. The effect is negligible or absent for the other channels (see figure 3.2a and 3.2b). The S1337 photodiode observes the $1020nm$ wavelength. From eq. 3.1, we have:

$$\frac{dS_{1020}}{dT}^{S1337} = 0.29\frac{\%}{C} \qquad (3.35)$$

Let ΔT be the temperature variation. S_{1020} changes according to:

$$\Delta S_{1020} = \frac{dS_{1020}}{dT}^{S1337} \times \Delta T \qquad (3.36)$$

A daily temperature change ($\Delta T_{day} = 10^\circ$) obtains $\Delta S_{1020} = 3\%$. A seasonal change ($\Delta T_{year} = 30^\circ C$) reveal a 9% S_{1020} change. The change in photodiode sensitivity is critical. The temperature must be monitored.

Eq. 3.35 states that the temperature measurement doesn't need to be very precise. ΔS_{1020} must not be greater than 1%. A temperature precision within $1^\circ C$ limits the relative uncertainty ΔS_{1020} to 0.3%.

3.2.2   The electronics

The circuit to measure the photodiode temperature is a simple voltage divider based on an NTC thermistor (figure 3.11). A fixed resistance
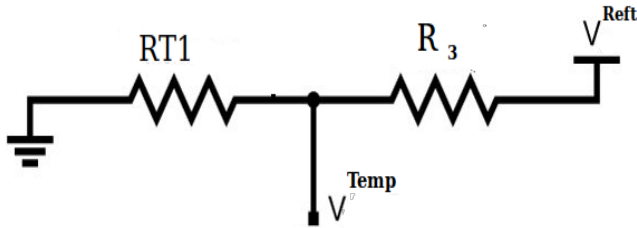
Figure 3.11. Circuit to measure the temperature. Simplified scheme

($R3 = 220k\Omega$) and the thermistor ($RT1$) form the circuit loop. A temperature increase makes $RT1$ decrease according to:

$$RT1(T) = RT1(298.15K)e^{\beta(\frac{1}{T} - \frac{1}{298.15})} \qquad (3.37)$$

where $RT1(298.15K)$ and β are device specific quantities. The NB20N50104KBA NTC thermistor from AVX was selected. The following values characterize this thermistor:

$$\beta = 4160K \qquad (3.38)$$

and

$$RT1(298.15K) = 100k\Omega \qquad (3.39)$$

Fig. 3.12a plots $RT1(T)$ for NB20N50104KBA. The circuit loop draws a small current because $RT1$ is on the order of $10^5\Omega$.

NB20N50104KBA is a surface mount device. Its package size is the standard 1206, its position is as close as possible to the photodiode and it lies on the same PCB layer, less than $1mm$ away from the light sensor.

The output voltage V^{Temp} is measured between $RT1$ and $R3$. The following equation describes the divider response:

$$V^{Temp}(T) = V^{Reft}\frac{RT1(T)}{RT1(T) + R3} \qquad (3.40)$$

where V^{Reft} is a fixed reference voltage. The optimal selection of $R3$ makes $V^{Temp}(T)$ proportional to T. Thus, $V^{Temp}(T)$ simulations with different $R3$ values were launched, the optimal fixed resistance $R3$ selected. Simulations considered temperatures between $-20°C$ and $40°C$, because environmental conditions generally don't exceed these boundaries. Figure 3.12b shows the plot of $V^{Temp}(T)$.

47
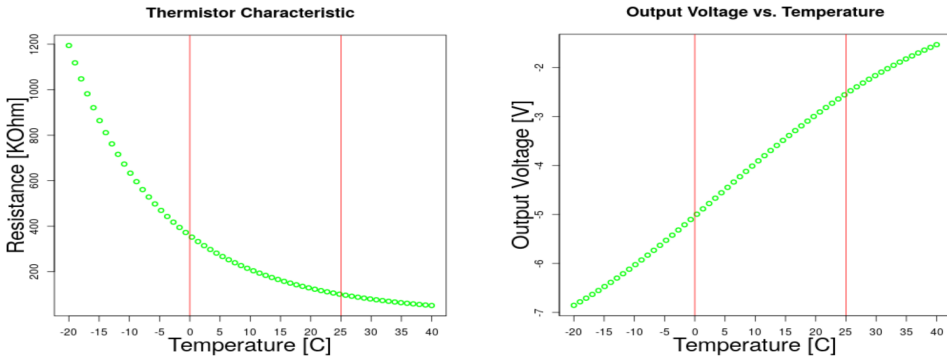
(a) $RT1$ vs. temperature

(b) V^{Temp} vs. temperature

Figure 3.12

Decoupling from supply load

OPA2191 and the thermistor voltage divider share the same negative supply ($V^{V^-} = -9V$). Load changes can cause supply voltage drops. The thermistor circuit works correctly if V^{Reft} is costant (see eq. 3.40). V^{Reft} fluctuations bias the temperature measurement. Thus, the "REFT" node voltage must be decoupled from supply.
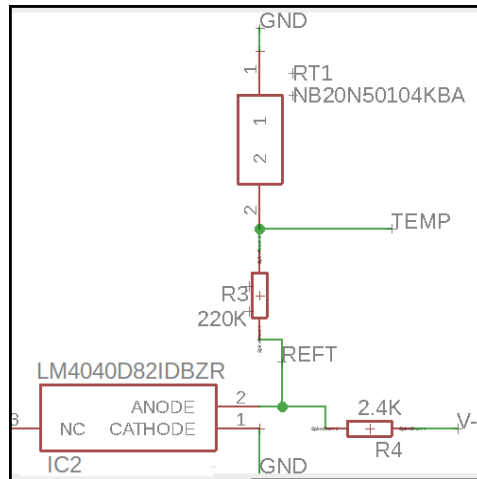
Figure 3.13. Circuit to measure the temperature. Eagle schematic.

Figure 3.13 is the schematic of the circuit used to measure the temperature. A second loop and a voltage reference ($IC2$) are added to the circuit. $IC2$ is the reference LM4040 from Texas Instruments

48

and it keeps a constant voltage $V^{Reft} = -8.192V$ within 1% tolerance, regardless of the supply voltage change.

LM4040 has minimum and maximum operating currents [36]:

$$I_{min}^{ref} = 100\mu A \tag{3.41}$$

$$I_{max}^{ref} = 15mA \tag{3.42}$$

If the current crossing $IC2$ exceeds these limits, LM4040 stops working correctly.

Let's consider R_4 and $IC2$. They form a voltage divider whose load is $R3 + RT1$. Let the current through $IC2$ be I^{LM4040} and the current crossing $R3 + RT1$ be I^{th}. The value of R_4 determines both I^{LM4040} and I^{th}. The following R_4 was selected:

$$R_4 = 2.4K\Omega \tag{3.43}$$

Let's show it keeps I^{LM4040} inside the operating range. We consider two extreme cases.

I^{LM4040} is maximum if these conditions happen simultaneously:
1) the temperature dependent resistance $R3 + RT1(T)$ is maximum.
2) a supply fluctuation makes the supply voltage $|V^{V^-}|$ increase. (usually $V^{V^-} = -9V$).

If the control unit electronics (see below, sect. 3.3) fails, $V_{max}^{V^-}$ can be as big as $V_{max}^{V^-} = -12V$. Let's assume this value. $RT1$ is maximum too:

$$RT1(-20°C) \simeq 1200k\Omega \tag{3.44}$$

The corresponding current crossing $RT1$ and R_3 is:

$$I^{th} = \frac{V^{Reft}}{RT1(-20C) + R3} = 5.8\mu A \tag{3.45}$$

We consider the "REFT" node. From Kirchhoff's current law:

$$I_{max}^{LM4040} = \frac{|V_{max}^{V^-} - V^{Reft}|}{R4} - I^{th} = 1.6mA \tag{3.46}$$

We have:

$$I_{max}^{LM4040} < I_{max}^{ref} \tag{3.47}$$

The current across $IC2$ is still inside the operating range. LM4040 keeps working correctly.

The I_{min}^{LM4040} is proven in a similar way. Let's consider:
1) a minimum $|V^{V-}|$ caused by supply variations. We assume an arbitrary value $V_{min}^{V-} = -8.6V$
2) a minimum $R3 + RT1$:

$$RT1(40C) \simeq 50k\Omega \qquad (3.48)$$

Equations 3.49 and 3.50 give the thermistor current and the current across LM4040 respectively:

$$I^{th} = \frac{V^{Reft}}{RT1(40°C) + R3} = 30.3\mu A \qquad (3.49)$$

$$I_{min}^{LM4040} = \frac{|V_{min}^{V-} - V^{Reft}|}{R4} - I^{th} = 140\mu A \qquad (3.50)$$

From the above equation it follows:

$$I_{min}^{LM4040} > I_{min}^{ref} \qquad (3.51)$$

Once again the current across $IC2$ is inside the operating range.

The range considered is more extended than the typical working conditions, so we can safely assume that LM4040 works correctly with $R4 = 2.4k\Omega$.

Thermistor self heating effects

Eq. 3.49 above reveals the maximum current across the thermistor: $I^{th} = 30.3\mu A$. I^{th} is small and a corresponding small power is dissipated across $RT1$:

$$P_{max}^{th} = V^{Reft} I_{max}^{th} = 0.25mW \qquad (3.52)$$

Hence, we can conclude the thermistor self-heating effect is negligible.

3.3 Control Unit Electronics

In this section the control unit electronics is described. Three are its main tasks:
- it sorts the measured voltages and the supplies to and from the telescopes of ARBOL
- it regulates the incoming power supplies
- it drives the 12 relays of ARBOL
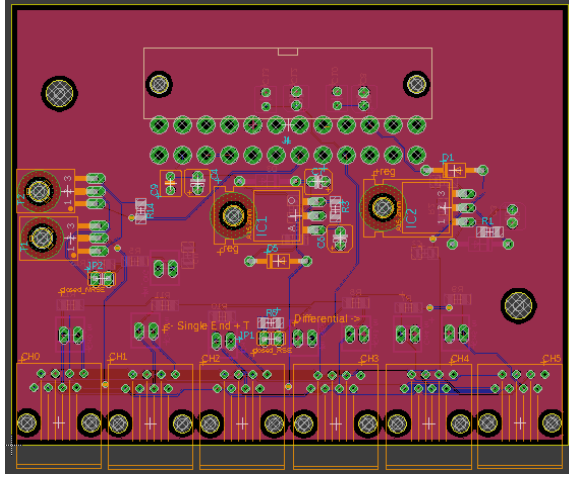
Figure 3.14. The control unit electronics. Eagle design

3.3.1 Power Supply

ARBOL needs a dual power supply for the analog front end circuit and a $+5V$ supply for the relay driver circuit. A commercial Alpine ATX Psu fulfils the requests. It provides $\pm 12V$ and $+5V$.

The control unit electronics regulates the $\pm 12V$ for three reasons:
- the output voltages of the ATX Psu are not very precise. The regulation sets precise symmetric supply voltages
- the ADC of ARBOL needs signals within $\pm 10V$. The regulation limits the supply range (and consequently the output signals) within $\pm 10V$.
- the regulation rejects the Psu voltage ripple

LM317 [50] and LM337 [51] are the selected adjustable regulators. LM317 regulates the positive supply, LM337 the negative. The adjustable output range is from $1.2V$ up to $37V$ ($-1.2V$ to $-37V$).

The regulating circuits follow the datasheets application information (fig. 3.15). Both circuits have two external resistors: R_1 and R_2 for the LM317 circuit, R_3 and R_4 for the LM337 circuit. The output voltage is set according to:

$$V_{out}^{LM317} = +1.25V \left(1 + \frac{R_1}{R_2}\right) \tag{3.53}$$
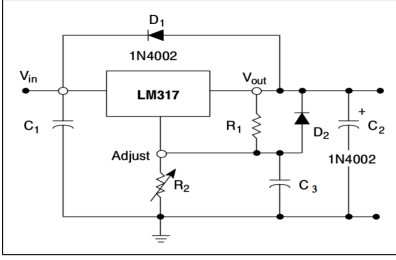
(a) Positive regulation   (b) Negative regulation
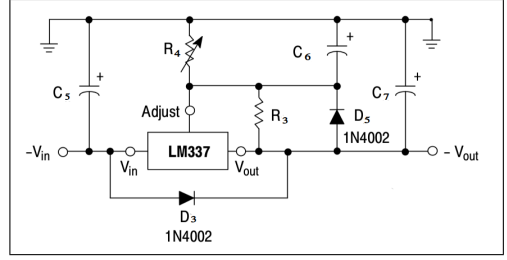
Figure 3.15. Voltage regulation circuit schemes

and:

$$V_{out}^{LM337} = -1.25V \left(1 + \frac{R_3}{R_4}\right) \tag{3.54}$$

The regulator circuits work correctly provided two requirements are fulfilled:

- first, the input-output voltage difference is greater than the voltage dropout of the regulators: $V^{do} < |V_{out} - V_{in}|$

- second, a minimum current load of $10mA$ flows across R_1 (R_3 for LM337):

$$\frac{V_{out} - V_{adj}}{R_1} = 10^{-2} \tag{3.55}$$

From the datasheets ([50] and [51]) we know V^{do} is smaller than $2.5V$. We avoid dropout problems because we set:

$$V_{out} = \pm 9V \tag{3.56}$$

and consequently $|V_{out} - V_{in}| = 3V > V^{do}$.

Eq.s 3.53 and 3.55 fix $R_1 = 120\Omega$ and $R_2 = 750\Omega$ and obtain $V_{out}^{LM317} = +9V$. The same resistor values ($R_3 = 120\Omega$ and $R_4 = 750\Omega$) determine $V_{out}^{LM337} = -9V$.

3.3.2 Digital Signal Control

A digital $+5V$ signal controls the relays of ARBOL. Here we compute the current driving the relays and discuss the relay driver circuit.

HEC721 datasheet [45] provides the coil resistance: $R_{coi} = 200\Omega$. A single relay on-status requires:

$$I_{coi} = \frac{+5V}{R_{coi}} = 25mA \tag{3.57}$$
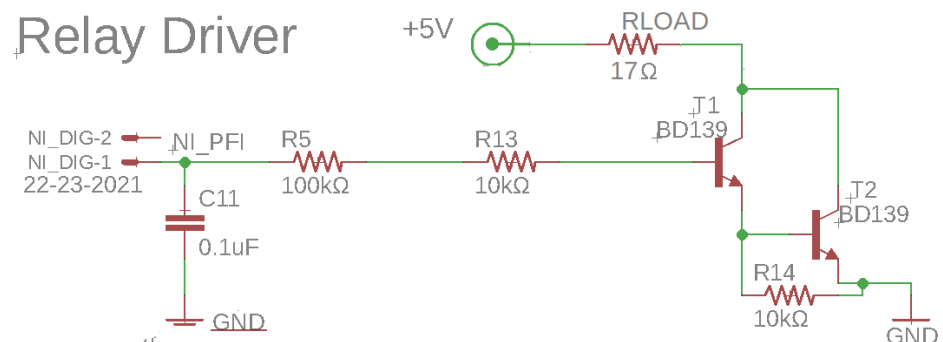
Figure 3.16. Relay driver circuit

ARBOL has got 12 relays. The total relay on-status draws 12 times the current above:

$$I_{rel} = 12 I_{coi} = 300 mA \tag{3.58}$$

The relay controller is the National Instrument acquisition device (NI device). Its maximum current output is $16mA$ (see [38], digital output characteristics), which means that it cannot provide enough current and an interface circuit is needed.

Figure 3.16 is the scheme of the relay driver circuit. The $+5V$ supply provides I_{rel} (eq. 3.58). The circuit is based on a Darlington transistor switch. R_{load} is the equivalent resistor of the 12 relays. Its resistance is $\simeq 17\Omega$. Two BD139 medium power transistors form the Darlington configuration.

We show the National Instrument device can control the relay driver: for collector currents above $250mA$, BD139 has got a DC current gain between 40 and 250 [40]. We assume a mean value $h_{FE} = 100$ for both T_1 and T_2, the transistors. The Darlington base current I_b is determined by:

$$I_b = \frac{I_{rel}}{h_{FE}^{T1} h_{FE}^{T2}} = 0.03 mA \tag{3.59}$$

The NI device can drive the Darlington pair, because I_b in eq. 3.59 is below the NI maximum output current ($16mA$).

To check that the circuit can actually switch the relays on, let's consider the loop from $+5V$ node to ground node, crossing R_{load} and $T2$. Let V_{load} be the voltage drop across R_{load}. Each HEC721 sees the same V_{load}, because R_{load} corresponds to the parallel combination of

53

the 12 relays. From the KVL, we have:

$$V_{load} = V_{sup} - V_{ce}^D \qquad (3.60)$$

where $V_{sup} = +5V$, V_{ce}^D is the voltage drop across $T2$. The following condition switches the relays on (see [45]):

$$V_{load} > 3.75V \qquad (3.61)$$

First, we compute V_{ce}^D. The expected collector currents of $T1$ and $T2$ are $I_c^{T1} \simeq 3mA$ and $I_c^{T2} \simeq 300mA$. From these current levels we get V_{ce}^{T1} and V_{be}^{T2} (see figure 2 and 3 of BDR139 datasheet [45]). Their sum is:

$$V_{ce}^D = V_{ce}^{T1} + V_{be}^{T2} \simeq 0.9V \qquad (3.62)$$

Inserting values into eq. 3.60, we have $V_{load} = 5 - 0.9 = 4.1V > 3.75V$. We can conclude the circuit design can switch the relays of ARBOL on.

The selected transistor type can withstand the dissipated power when the relays are switched on:

$$P^{T2} = I_c^{T2} V_{ce}^D = 0.24W \qquad (3.63)$$

P^{T2} is below $1.25W$, the maximum power dissipation for BD139.

Finally, we analyze the Darlington base current, I_b: this current loop starts from the National Instrument device (node NI_{PFI} in fig. 3.16), crosses $R_{13} + R_5$, T_1 and T_2 and comes to ground node. We fix R_b value to get $I_b = 0.03$ (as in eq. 3.59). From the KVL and Ohm's law:

$$R_b = \frac{V_{sup} - V_{be}^{T2} - V_{be}^{T1}}{I_b} = 110K\Omega \qquad (3.64)$$

By using $R_{13} = 10K\Omega$ and $R_5 = 100K\Omega$ the series resistance is equal to R_b.

3.4 Acronyms in chapter 3

Acronym	Meaning
PCB	Printed Circuit Board
TIA	TransImpedance Amplifier
DC	Direct Current
AC	Alternating Current
GBW	Gain Bandwidth product
NG	Noise Gain
NTC	Negative Temperature Coefficient (referred to a thermistor)
Psu	Power Supply Unit
ADC	Analog-to-Digital Converter
NI	National Instruments
KVL	Kirchhoff Voltage Law

CHAPTER 4

Software and acquisition

4.1 National Instruments Acquisition Device

4.1.1 Brief Device Description

(a) The NI-6210 acquisition device
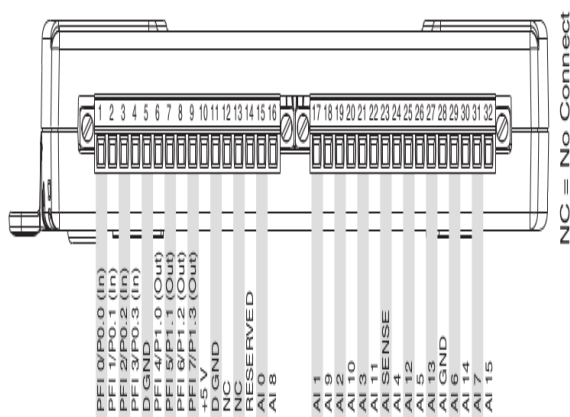
(b) USB-6210 pinout scheme

Figure 4.1

The National Instruments USB-6210 [38] carries out the signal acquisition of ARBOL and controls the relays of the instrument. This multifunction device has many inputs and outputs. Its pinout includes (fig. 4.1b):

57

- 16 single ended analog inputs. These inputs can be used as 8 differential inputs as well.
- 4 digital inputs
- 4 digital output channels
- a $+5V$ node referred to the device ground
- nodes to manage the measurement system ground (analog ground AI_GND, digital ground DG_GND, AI_SENSE described below)

Each analog input has a 16-bits ADC.

The USB-6210 device (NI-daq hereinafter) allows a remote control of ARBOL by means of a dedicated code. The code controls both the analog acquisition and the relay switching.

Ground loops deteriorate the signal acquisition precision. Hence, a proper grounding helps to avoid ground loop problems. The next section discusses the system grounding.

4.1.2 The grounding issue
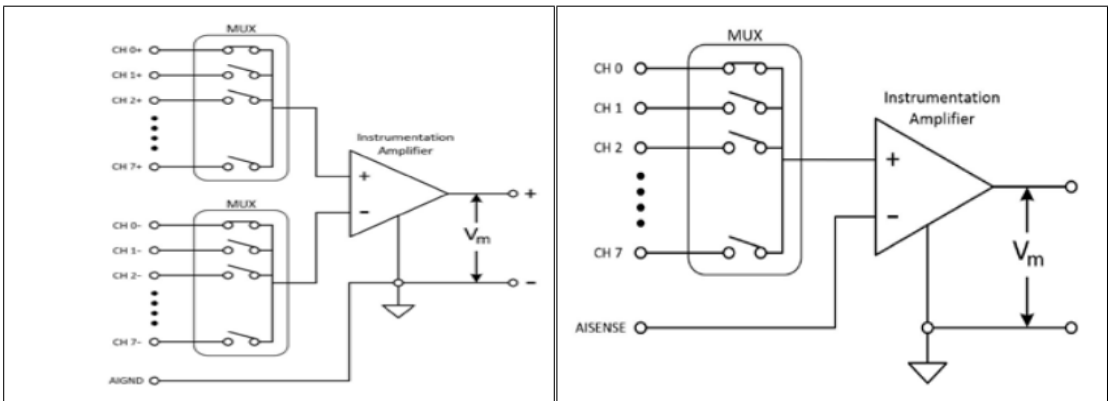
(a) Diff. Configuration   **(b)** NRSE Configuration

Figure 4.2. Connection schemes (Figures borrowed from NI technical note [44])

The grounding issue arises because the ground level of NI-daq generally differs from the system ground (the supply ground of ARBOL in our case). In this case, unwanted currents between the two nodes start flowing and a ground loop is generated. Two configurations to acquire measurements and avoid this issue are explained here.

By definition, a voltage signal referenced to a system ground (such as earth or a building ground) is a grounded signal source. The front-end voltage signals of ARBOL are grounded signal sources. National

Instruments recommends either a differential or a Non-Referenced Single Ended (NRSE) mode to preserve the acquisition accuracy [44]. The former mode is the configuration chosen to acquire the front-end light signals.

Figure 4.2a shows the differential mode configuration. An instrumentation amplifier rejects the signal common-mode voltages. For this reason, the differential mode is the most accurate. However, for each signal acquisition the amplifier needs one input for the signal and one input for the corresponding reference voltage. Thus, the input wires are twice the acquired signals. As ARBOL measures six wavelengths, 12 inputs are connected to NI-daq.

Other acquisition modes are single ended and one input wire per acquisition is enough. Thus, the other modes are less precise but simpler. The NRSE mode is used to acquire voltages from the front-end temperature measurements. Three of the six telescopes of ARBOL have a temperature measuring circuit. Consequently, only three NI-daq inputs are used to acquire temperature signals. Finally, the reference voltage level is sent to the AI_SENSE node (see fig. 4.2b).

NRSE and differential acquisition modes are thought to keep the supply ground split from the NI-daq ground. However, no electrical insulation between the NI-daq digital control and the driver circuit was conceived during the design phase. Consequently, they must share the same reference level. For this reason, NI-daq and supply ground have actually been connected. Fortunately, the issue is not critical. Acquisition tests didn't show any ground loop despite the connection of the two ground nodes.

A future version of the relay driver circuit must include the electrical insulation to allow the ground splitting. This is a precaution to further ensure that there aren't ground loops in the signal acquisition.

4.1.3   Connection summary

Table 4.1 summarizes:
- the connections from the NI-daq inputs/outputs to the control unit electronics
- the connections from the control unit electronics to the front-end PCBs inside the telescopes of ARBOL
- the grounding connections

NI-daq i/o nodes	Contr. unit nodes	Spectral channel
Ai0	ch0 left	400nm
Ai1	ch1 left	940nm
Ai2	ch2 left	1020nm
Ai3	ch3 left	500nm
Ai4	ch4 left	675nm
Ai5	ch5 left	870nm
Ai6	ch0 right	400nm temp.
Ai14	ch1 right	940nm temp.
Ai7	ch2 right	1020nm temp.
Ai GND	NI_GND	—
Ai SENSE	AGND	—
PFI7	NI_PFI	—

<div align="center">Table 4.1</div>

4.1.4 The acquisition lower limit. Quantization noise

NI-daq contains 16-bit ADCs. Each of them converts the front end analog signal into one of 2^{16} digital values. The ADC analog input range is from $-10V$ to $+10V$. The least significant bit (LSB) is:

$$LSB = \frac{10 - (-10)}{2^{16}} \simeq 300\mu V \qquad (4.1)$$

From the eq. above, we can evaluate the quantization noise E_{dg} [20]:

$$E_{dg} = \frac{LSB}{\sqrt{12}} \simeq 87\mu V \qquad (4.2)$$

The total output noise is the squared sum of the quantization noise 4.2 and of the preamplification noise 3.27 ($E_{an} = 24\mu V$):

$$E_{tot} = \sqrt{E_{dg}^2 + E_{an}^2} = 90\mu V \qquad (4.3)$$

The front-end analog noise is small, while the ADC quantum noise is dominant.

Note that the LSB value in the equation 4.1 is greater than the result of eq. 4.3. For this reason, it's the LSB step that limits the acquisition dynamic range. Both artificial light (LED-based) and dark tests showed that the signal noise E_{tot} cannot be detected, because it is smaller than the LSB.

4.1.5 A possible future improvement

The digitized output voltages have unexpected DC offsets. They are on the order of few mV. In sect. 3.1.6 it was shown the front-end output offset is negligible. These offsets are probably due to the NI-daq electronics. They might drift with temperature. Further tests (both laboratory and in situ measurements) are necessary to investigate them. Their characterization will improve the low light acquisition reliability of ARBOL.

4.2 The acquisition software

The acquisition device can be controlled either by Labview or directly with C APIs. The C option has been adopted because:
- it is free
- it works well in the Unix environment
- in case of huge data sets, it's the best performing solution
- the APIs were integrated with Qt and QCustomPlot. Consequently, the software of ARBOL has a user friendly graphical interface.

The APIs from National Instrument are not supported for Debian-based operating systems. For this reason, the computer controlling ARBOL has a CentOS operating system.

The following subsections describe the software of ARBOL. To begin with, the NI-daq APIs are described. They rely on NI-DAQmx Base, a driver that allows to build applications for many NI devices, the USB-6210 included. Then, the other software characteristics are reported: the acquisition timings are introduced, the graphical interface explained and the file format of registered data described.

4.2.1 The API structure

NI-daq API manual can be found online [46]. However, a documentation more focused on C programming is provided as HTML page, alongside the device installation.

Every NI-daq duty corresponds to a NI-DAQmx software task. A task is a collection of one or more virtual channels with timing, triggering, and other properties. At this level all the parameters necessary for the channels configuration and creation must be fed to the task. Three are the NI-daq duties during a measurement of ARBOL:

- the measurement of light (i.e. an analog input acquisition task)
- the temperature measurement (an analog input acquisition task again)
- the digital relay control (a digital output task)

   The following instructions manage the analog acquisition:

1) "DAQmxBaseCreateTask" creates the task.

2) "DAQmxBaseCreateAIVoltageChan" provides the task with:
- the name of the NI-daq inputs to acquire the signal from ($Ai0, Ai1$,...
See figure 4.1b for the pinout)
- the task acquisition mode (NRSE or differential)
- the maximum and minimum analog input voltages

3) "DAQmxBaseCfgSampClkTiming" configures the acquisition tim-
ing parameters:
- the sample clock source to use (internal or external clock source)
- the sample rate. NI-daq samples the analog signals of every input
channel in the task once for every clock shot [42].
- a flag to select the finite or continuous acquisition. In the former case
the number of samples to be acquired for each channel is required too.

4) the task is started ("DAQmxBaseStartTask"): from this moment
on NI-daq is acquiring.

5) the computer reads the acquired data with "DAQmxBaseReadAnalogF64".

   The digital task is created an controlled in a similar way:

1) "DAQmxBaseCreateTask" creates the task

2) "DAQmxBaseCreateDOChan" creates the digital output line. Here
the channel name is set (PFI pins in figure 4.1b)

3) "DAQmxBaseStartTask" starts the task

4) "DAQmxBaseWriteDigitalU32" controls the digital output status
(0 or 1)

   Ports of four digital output lines are generally found on NI USB
devices. A port status is controlled with an hexadecimal number, which
is a short way to set four lines together.

   Finally, proper instructions stop and close the tasks (both analog
and digital) to release the memory. These instructions are "DAQmxBaseS-
topTask" and "DAQmxBaseClearTask".

4.2.2   ARBOL software and acquisition timings

ARBOL software is based on C++. It integrates the National Instru-
ments APIs with QCustomPlot and Qt. The core of the software are
three objects:
- the class "cont_acqNI"

- the class "plotReadNI"
- the class "evRec"

Class "cont_acqNI" is the actual NI-daq controller. It initializes the NI tasks:
- a first analog input task for measuring light
- a second analog input task for measuring the front-end temperature
- a digital output task to control the relays of ARBOL
Furthermore, "cont_acqNI" initializes the whole set of objects to manage the signal acquisition: QTimers, QButtons, "plotReadNI" classes to access the graphical interfaces, the "evRec" class to record acquired data. Finally this class wipes the environment by releasing the employed memory.

Class "plotReadNI" is the QCustomPlot graphical interface. QCustomPlot is a Qt C++ widget specifically developed for data visualization. Its collection of C++ objects allows the programmer to create personalized canvas.

Finally the class "evRec" is responsible for data registration.

In the next section some characteristics regarding the acquisition software are analyzed.

The acquisition times for the sunlight measurement

ARBOL software must manage the acquisition times on two different levels:
- slow times: the time scales are greater than a second. In this case, QTimer classes schedule events repeated in time (event loops) with repetitive shots. They invoke the analog acquisitions at the right time.
- fast times: shorter than a second. These events are fast paced, they happen inside the acquisition task. The task time parameters govern these events. For example, the signal is sampled according to the sampling frequency. The latter is set with the the API instruction "DAQmxBaseCfgSampClkTiming" (see above).

The software of ARBOL is written ad-hoc and consequently it is very flexible. The following time parameters have been chosen arbitrarily:
- the sunlight measurement is made once every 5 seconds
- both the the temperature and the light measuring tasks collect a finite amount of samples (finite acquisition option)
- every acquisition collects 300 samples per channel (i.e. for each wavelength)
- the sample rate is $f_r = 600 Hz$

The task measurement lasts $\Delta t = 0.5s$. The spectral channels are acquired simultaneously during Δt. An average of the collected samples over Δt is the measurement. A root mean square value is obtained too and assigned as measurement uncertainty.

The almucantar scan and its perspectives

By definition, the almucantar is a circle in the sky whose points must have an elevation angle coinciding with the Sun elevation.

In the almucantar a sunphotometer observes aureole and sky radiances through a large range of scattering angles. The almucantar measurement is essential for the retrieval of the aerosol phase function (see Nakajima *et al.* 1996 [6]). Moreover, it allows to derive size distribution and aerosol optical depth as well (Holben *et al.* 1998 [8]).

ARBOL is not ready to observe the almucantar yet. Tests have been made, but issues regarding the characterizations (see sect. 5.1.2 for a better description) have hindered observations, making them unreliable. Nevertheless, the almucantar software has been created.

The new version of ARBOL software manages both the high and low gain acquisition. Each acquisition has the same time parameters as before (finite number acquisition; 300 samples; $f_r = 600Hz$; $\Delta t = 0.5s$). A QTimer calls the acquisition sequence, whose structure is the following:
- the low gain is activated. A first analog task is started, the low gain observation performed
- the first task is completed. The digital task switches on the high gain
- a second analog task is started, the high gain observed
- the second task is completed. The high gain is switched off
- a third analog task is launched. The front-end temperature measured

For each almucantar angle, the sequence above acquires samples with both the high and the low gain. In sect. 3.1.4, we showed that there is a light (or photocurrent) range where both the gain regimes can acquire samples. Thus, the almucantar sequence makes the intercalibration between high and low gain observations possible.

The first almucantar tests were done with a 5 seconds break between a measurement and the following one. 5 seconds correspond to about $12°$ angle step, because the solar tracker scan speed is $2.43\frac{deg}{s}$. The sky radiance changes the most for azimuth angles close to the Sun (the aureole). Thus, the resolution is fine for sky observations, but scarce for aureole measurements.

The resolution will be increased as development goes on. If the number of samples per channel is set to 90 and the sample rate maintained $f_r = 600Hz$, the analog acquisition task needs only:

$$\Delta t = 90 \times \frac{1}{f_r} = 0.15s \qquad (4.4)$$

to complete the acquisition. Thus, ARBOL will measure both the high and low gain in $\Delta t = 0.3s$. Assuming we launch the fast acquisition sequence every 0.4 seconds, from the solar tracker speed we get the following angular resolution:

$$\Delta \theta = 0.4 \times 2.43 \simeq 1° \qquad (4.5)$$

The angular resolution above is high. Current existing photometers reach a resolution as high as 2°. ARBOL is expected to halve this limit.

The digital signals

A single digital output is enough because the 12 relays of ARBOL are synchronized. Accordingly, only the "PFI7" line of the USB-6210 device is connected (see the pinout 4.1b). The relays are activated writing the hex number "0x8". The instruction makes the high gain front-end electronics ready to measure. The hex zero switches the relays off. The low gain can be used.

Data recording

Let's consider a single run of an analog task. We are measuring light with ARBOL. NI-daq acquires data from different wavelengths into a single array. This is the interleaved option, which makes the acquisition faster. Class "evRec" saves data into a table, called record. We describe the record structure.

A record begins with the string "NDR" (new data record). Then, we have a header row and a header column. The former contains the shot times of the sample clock, while the latter the names of the NI-daq analog inputs. "evRec" splits data based on the sample clock time and the input channel. It puts each data in the corrisponding record field. Finally, each record table terminates with a blank line. When the software of ARBOL is launched, "evRec" opens a file. Everytime QTimers call an acquisition task and data are acquired, "evRec" adds

Figure 4.3. An example of file containing two records, written by "evRec".

a new record into the same file. Thus, in figure 4.3 we see two records inside the same file. The first record is referred to a light measurement, the second to a temperature measurement. The file name must contain the date and time the ARBOL software is launched, in the exact next format: "yyyy-MM-dd_hh:mm:ss.dat".

Graphical User Interface

The graphical user interface (GUI) has proved itself fundamental for ARBOL development, because it shows ARBOL observations in real time. Nevertheless, the GUI is not mandatory: the ARBOL software can work without it as well. The GUI generates a sample data vs time plot for every channel of ARBOL.

The "plotReadNI" class is the QCustomPlot user-friendly window. "cont_acqNI" initializes one or more "plotReadNI" classes inside its constructor. The number of acquired channels determines automatically the number of windows. Each canvas hosts two channels plots. The string "Stop Scaling ai#" (centered inside the plot square) allows an easy channel identification (see figure 4.4). The charts auto-scale the plots by default, but it's an option that can be disabled. If the user clicks the "Stop Scaling" label, the window stops scaling the plotted data. Moreover, the user can either drag the axis range or scroll it to change the zoom with the mouse wheel.

In fact, NI-daq cannot access its sample clock, because the NI-daq APIs don't support this retrieval. Thus, the computer clock is used to plot data vs time. A Qt code instruction evaluates the UTC time $t_{sam}[0]$ right before the acquisition task begins. For each sample, the acquisition time is interpolated with a simple law:

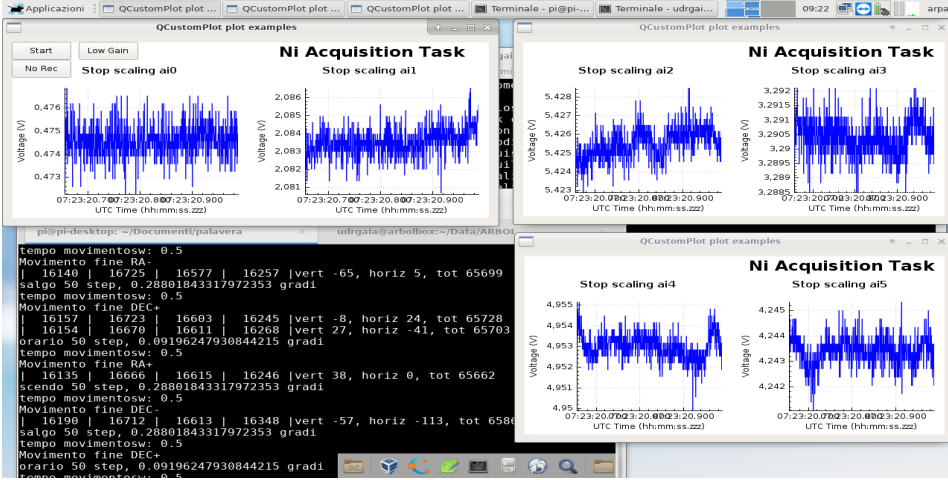$$t_{sam}[i] = t_{sam}[i-1] + \Delta t_{sam} \tag{4.6}$$

Figure 4.4. Real-time plotting of ARBOL data for the six spectral channels. The auto-scale option is active

where i spans from 0 up to 300 (the number of samples per channel), Δt_{sam} is the inverse of the task sample rate (for direct Sun measurements $f_r = 600 Hz$):

$$\Delta t_{sam} = f_r^{-1} \simeq 2mS \tag{4.7}$$

The resulting time array is passed to "plotReadNI" to plot collected data.

The graphical user interface also offers three QButton objects for some basic controls (see the high left corner of figure 4.4):
- the acquisition start/stop
- the low/high gain switch (controlling the front-end relays)
- the data record start/stop
The same options are managed automatically in the software version without the GUI.

Finally, everytime an acquisition task is invoked, the graphical interface is refreshed immediatly afterwards. A QTimer manages the GUI refreshing too, hence the GUI plots are real time plots.

The software simplified scheme

To conclude the current chapter, it'll be shown a (simplified) scheme to summarize the software operations.
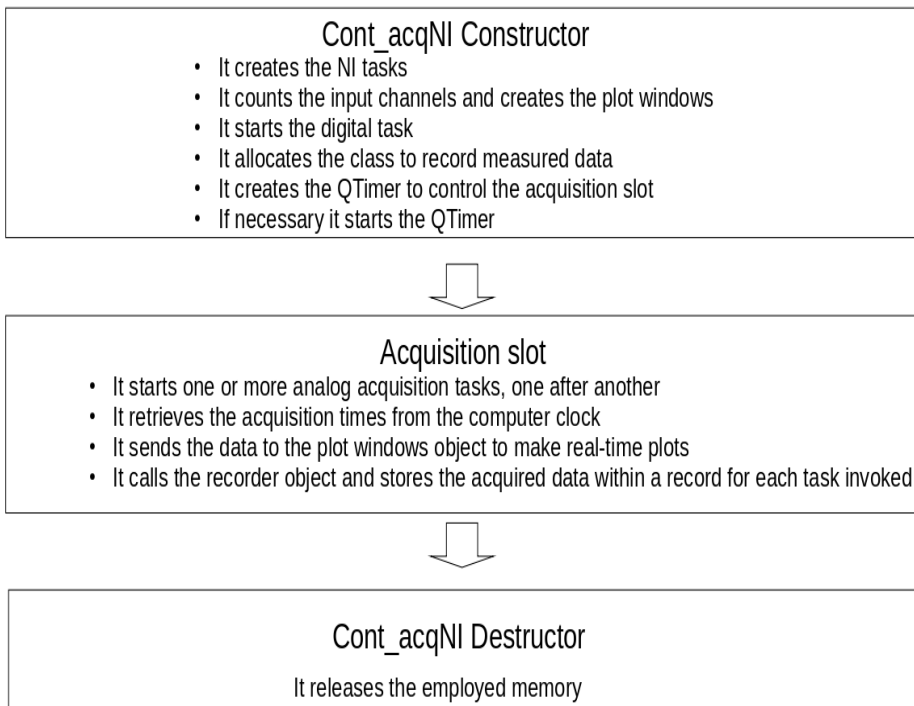
Cont_acqNI Constructor
- It creates the NI tasks
- It counts the input channels and creates the plot windows
- It starts the digital task
- It allocates the class to record measured data
- It creates the QTimer to control the acquisition slot
- If necessary it starts the QTimer

Acquisition slot
- It starts one or more analog acquisition tasks, one after another
- It retrieves the acquisition times from the computer clock
- It sends the data to the plot windows object to make real-time plots
- It calls the recorder object and stores the acquired data within a record for each task invoked

Cont_acqNI Destructor

It releases the employed memory

Figure 4.5. Simplified diagram to summarize the software operations

4.3 Acronyms in chapter 4

Acronym	Meaning
NI	National Instruments
NI-daq	USB-6210 National Instruments AcQuisition Device
NRSE	Non-Referenced Single-Ended mode
ADC	Analog-to-Digital Converter
PCB	Printed Circuit Board
LSB	Least Significant Bit
DC	Direct Current
API	Application Program Interface
GUI	Graphical User Interface

Characterizations

We explain here the main instrument characterizations:

– the retrieval of the front-end electronics gain values

– the characterization of the telescope field of view

– the correction of measurements affected by temperature biases

The two ARBOLs have been specifically used under different sunlight and skylight conditions. This allows us to cover a good set of cases of real interest.

5.1   Gain Value retrieval

Generally, the diffuse sky radiance is normalized over the direct normal irradiance and given as input to the data analysis algorithms. ARBOL uses one sensor to measure both these quantities. This choice implies one benefit and one drawback:
- the benefit is remarkable: the normalized radiance does not depend on the sensor responsivity. The latter cancels out when data are normalized. Thus, the sensor response characterization is avoided.
- the same sensor must observe a wide dynamic signal range. This is a drawback, because the direct Sun signal is order of magnitudes more intense than the diffuse sky signal. Thus, to design a proper preamplification electronics becomes a challenging technical task. We describe now this task.

Photodiodes are ideal components to cover the needs of both sky and Sun measurements. Their dynamics can actually span orders of

magnitude. They produce a photocurrent proportional to the incoming light. As the Sun direct irradiance and the diffuse sky radiance differ for orders of magnitude, the same is true for the Sun and sky photocurrents.

The transimpedance amplifier (TIA) circuit converts the photocurrents into analog voltages. The voltage digitalization imposes strict boundaries. The analog voltage must lie between 10 volts and few millivolts. The TIA preamplification must map an input current range 5 orders of magnitudes wide (see below) into an output voltage only three orders of magnitude wide. This is the technical challenge.

To solve this problem, the transimpedance is given two gain loops and two gain values (R_1 and R_2, see the schematic 3.4). The values of R_1 and R_2 must be optimal to guarantee a proper current to voltage conversion factor. A step by step approach has been assumed to optimize the gain values.

5.1.1 Numerical simulations

The first step is to estimate the extension of the input current range. Both sunlight and skylight have been simulated with a numerical code, Uvspec. Uvspec is a radiative transfer model included in LibRadtran 2.0.2 (see Emde, Buras-Schnell, Kylling, *et al.* 2016[29]), a set of packages adopted for the Meteosat meteorological forecasting.

To find the direct beam irradiance, $EDIR$, the rte solver "disort" with the standard six streams approximation has been employed. The following inputs were given to Uvspec:
- the U.S. Standard atmospheric profile (afglus.dat).
- the plane-parallel geometry.
- a solar zenith angle $SZA = 22°$, corresponding to the summer solstice conditions in Aosta.
- an observation site altitude $z = 1600m$, corresponding to the highest measurement site of the GAIA project, the OAVdA site, where the direct sunlight is expected to reach the brightest conditions.
- a spectral range from $340.0nm$ to $1100.0nm$, including all the filter bands of ARBOL.
- a 300 D.U. ozone concentration to account for the gas absorption. Other gases have been neglected.
- the default aerosol model described in Shettle and Fenn 1979[2].
- a small aerosol load. The angstroem parameter have been assumed to be $\beta = 0.02$, $\alpha = 1.1$.

The direct normal irradiance DNI is obtained from $EDIR$ through the following equation:

$$DNI = \frac{EDIR}{cos(SZA)} \tag{5.1}$$

where SZA is the solar zenith angle. The light power falling onto the photodiode is given by:

$$P^{in} = \Delta\lambda \times S^l \times DNI \tag{5.2}$$

where $\Delta\lambda$ is the FWHM of the narrow transmission window of the passband filters, S^l the illuminated area of the objective lens.

The diffuse radiance has also been simulated with Uvspec. The inputs are the same as above, but with the following exceptions:
- only monochromatic simulations at $400nm$, $500nm$, $675nm$, $870nm$ and $1020nm$ were launched
- a solar zenith angle $SZA = 30°$.
- an observation zenith angle equal to SZA. Note that ARBOL observes the diffuse radiance along the almucantar, and therefore the two angles coincide.
- an observation azimuth angle spanning from 2.5° up to 20°, with a grid $\Delta\phi = 0.5°$ up to 10°, $\Delta\phi = 2.5°$ up to 20°.
- a small surface albedo (0.2). In this case, the goal is to minimize the diffuse component to simulate the weakest sky radiance.
- the default aerosol model Shettle and Fenn 1979[2] with $\beta = 0.02$.

The following equation describes the diffuse radiation power impinging onto the sensor:

$$P^{in} = \Delta\lambda \times \Omega \times S^l \times Rad \tag{5.3}$$

where Rad is the sky radiance, Ω the solid angle observed by a telescope, S^l the illuminated objective lens area and $\Delta\lambda$ the FWHM of the filter transmission. The optomechanical specifications of each telescope are the following:
- $S^l = 491mm^2$
- $\Omega = 10^{-4}\pi sr$
- $\Delta\lambda = 10nm$ for all the spectral channels but the $1020nm$ wavelength, where $\Delta\lambda = 15nm$.

According to sunlight simulations, a few mW reach the photodiode in each channel. For example, $P^{in} \simeq 8.3mW$ at $500nm$, $P^{in} \simeq 4.7mW$

at $870nm$. During the sky observation the incident power can be as small as $P^{in} \simeq 10nW$, particularly in the infra-red channels. The corresponding photocurrents can be estimated as:

$$I_{pd} = P^{in} S_\lambda \qquad (5.4)$$

where I_{pd} is the photocurrent, P^{in} the impinging light power and S_λ the photosensitivity for the wavelength λ. The latter is obtained from the plots in figure 3.1. Inserting S_λ and the simulated P^{in} into eq. 5.4, we find a photocurrent range between 10 nA and $2-3$ mA. This is the expected photocurrent range.

5.1.2 Test measurements

Results from the previous simulations can be verified using in situ test measurements. This is the final step to optimize the gain values, R_1 and R_2. In this case, the employed telescope and electronics are prototype versions. A first transimpedance amplifier stage and a simple subsequent inverting amplifier are adopted for the tests. There isn't an high gain loop in the test circuit, but the second stage inverting amplifier provides an extra voltage gain $A \simeq 200$. The sensor is the photodiode S5107. The V_{out1} node (see figure 5.1) is the first stage output, while the V_{out2} node is the second stage output. $R_1 = 3.3K\Omega$ is chosen from numerical simulations. The transimpedance amplification for V_{out2} is:

$$R_2^{test} = R_1 \times A \simeq 660K\Omega \qquad (5.5)$$
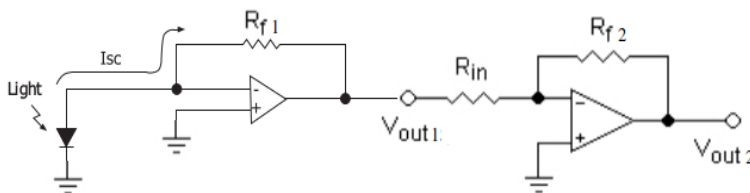

Figure 5.1. Scheme of the prototype circuit used during the measurement tests.

This kind of circuit was used only during these test measurements, because the front-end of ARBOL is an improved circuit version. However, the circuit of fig. 5.1 is more than acceptable for these characterizations. Finally, the voltage signal is acquired with the "BitScope", a programmable PC-based oscilloscope.
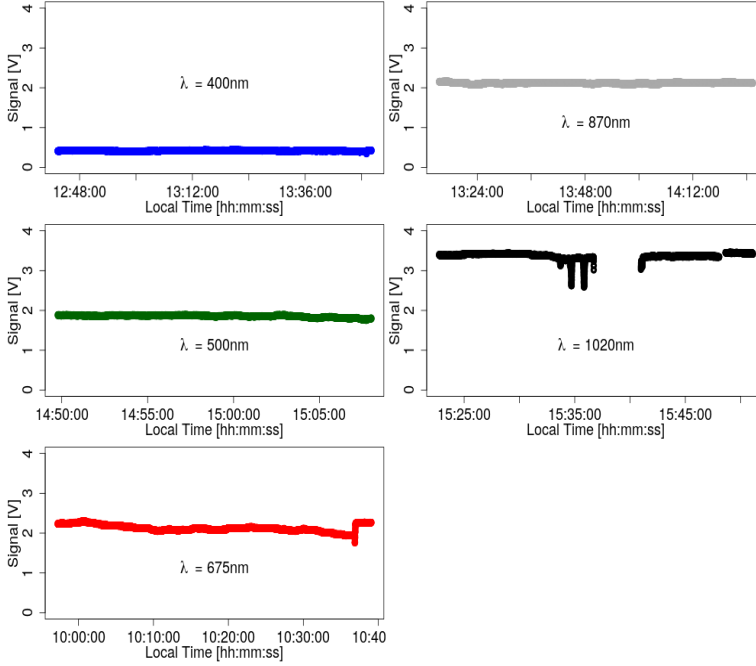
Figure 5.2. Measurement test taken July, 17 and July 18, in Milan. The plots shows clearly the signal's range is between 0.5 and 4 volts with $R_{f1} = 3.3K\Omega$

Test measurements were performed for many days and from different locations. V_{out1} was never larger than $4.5V$ even during days close to the Summer solstice. For this reason ARBOL has been given a R_1 value about two times larger than that adopted for the tests:

$$R_1 = 6.8K\Omega \tag{5.6}$$

The same could not be possible for R_2. Actually, stray light prevented the possibility of performing reliable tests. The stray light becomes critical when weak light power is observed. This is the case of skylight. Therefore, the value of R_2 resulting from simulations is maintained for the moment:

$$R_2 = 680K\Omega \tag{5.7}$$

More accurate tests on R_2 have been performed with the final instrument configuration. The latter is better in terms of mechanical precision and stability and the stray light is almost removed. At the time this PhD thesis is written, the sky observations are still being devel-

oped. Anyway, we expect to increase R_2, as it has already been done with R_1.

Figure 5.3. The prototype of ARBOL

From now on, we will leave diffuse sky measurements and focus on direct Sun measurements only. The following section describes the field of view and the photodiode temperature response characterizations.

5.2   Direct signal photocurrents

As already explained, ARBOL signal acquisition is based on the National Instrument acquisition system. It's worth recalling that ARBOL acquires 300 samples within the time interval $\Delta t = 0.5s$ every 5 seconds. A single measurement corresponds to the sample average within Δt and the root mean square (rms) gives the uncertainty.

In section 4.1.4 it was shown that the signal dynamic range is determined by the least significant bit (LSB) of the NI device:

$$\Delta V^{LSB} \simeq 300 \mu V \tag{5.8}$$

Specific tests with artificial light sources have confirmed this limit. Nevertheless, the sample root mean square within $\Delta t = 0.5s$ is larger than the LSB limit. Thus, in real sunlight conditions the signal is less stable and measurements show greater uncertainties. We recognize two sources of signal instability:
1) the atmospheric turbulences;
2) the solar tracking perfromances
We believe source "2" is the most relevant. In the next section we discuss the field of view characterization to improve the solar tracking precision.
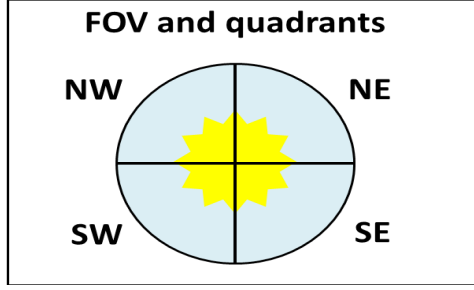
Figure 5.4. The Sun in the field of view

5.2.1 Solar tracking and FOV characterization

The position of the Sun inside the field of view (FOV) of the telescopes may affect the measured signal. Hence, the FOV must be characterized. If proper offsets are added to the following differences:

$$(NW + NE) - (SW + SE) \tag{5.9}$$

and:

$$(NW + SW) - (NE + SE) \tag{5.10}$$

it is possible to move the Sun inside the FOV (see section 2.4.2). In eq.s 5.9 and 5.10, NW, NE, SW and SE are the QPD quadrant signals. The former difference tunes the height direction, the latter the azimuth direction. For istance, let's consider the azimuth characterization of $ARBOL_A$ in fig. 5.5a. If an offset $offs = -1000$ is added to eq. 5.10, the Sun is moved 0.77° westwards in the telescope FOV.

Cloudless days and small solar zenith angles are selected to perform the characterization. Moreover, the atmospheric disturbances should be as small as possible during the process. We characterized both the instruments: $ARBOL_A$, which is installed at the observatory site, and $ARBOL_B$, which is installed at the ARPA site. Each instrument needs two characterizations, one for each direction. Both the directions were spanned covering an angular range 1° wide. For each offset the corresponding telescope signal was recorded, so that plots 5.5 and 5.6 are obtained for $ARBOL_A$ and $ARBOL_B$, respectively.

When the Sun is centered in the field of view, the signal is maximized and less noisy. Hence, the FOV curves show a maximum condition. If this condition is adopted to calibrate the tracking software, the tracking is optimized and the instrument performances improved.

Figure 5.7 compares two days of measured photocurrents with $ARBOL_A$. The former is on March, 22 and the tracking software is uncalibrated.
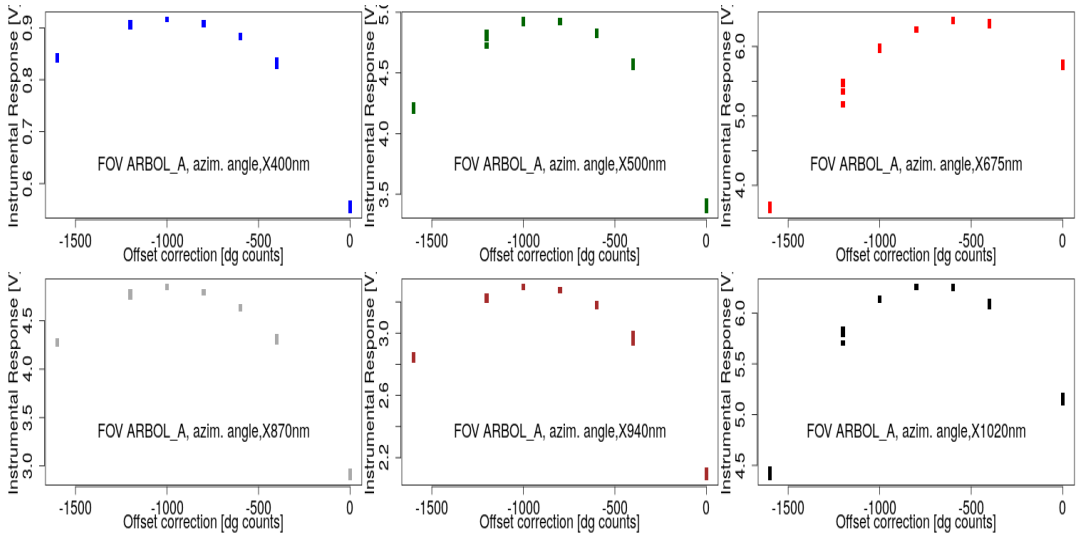
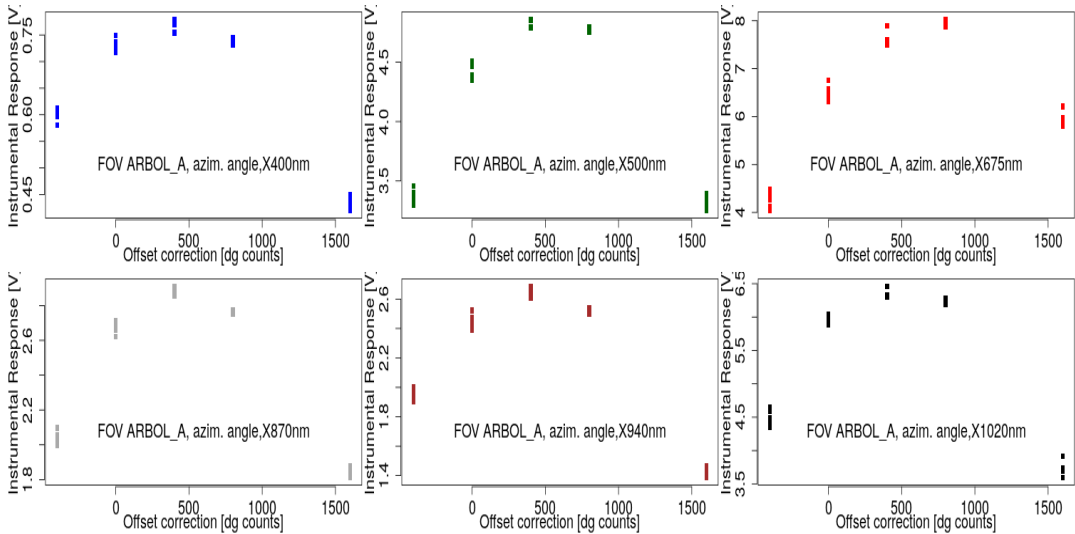(a) Azimuthal angle characterization
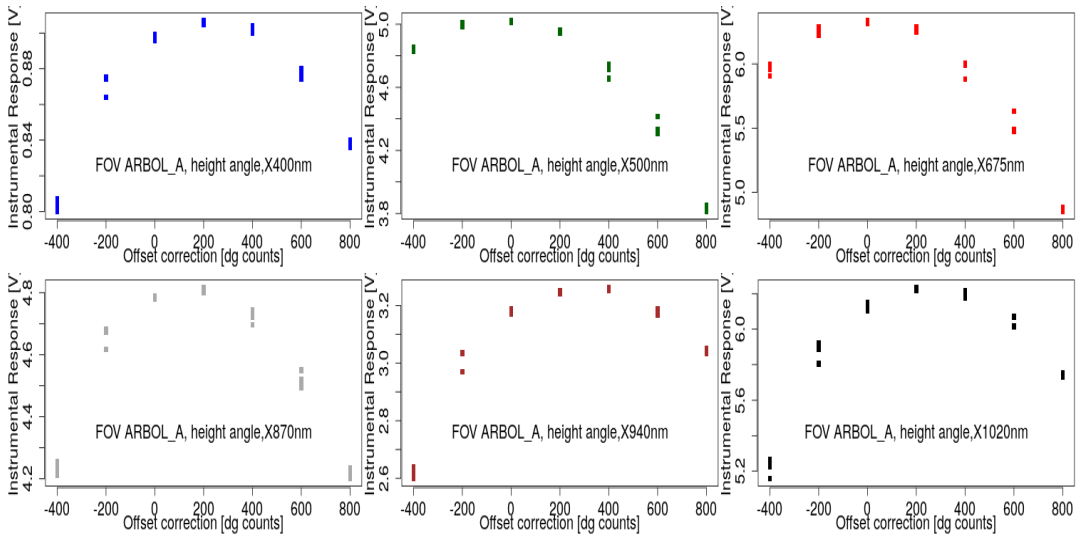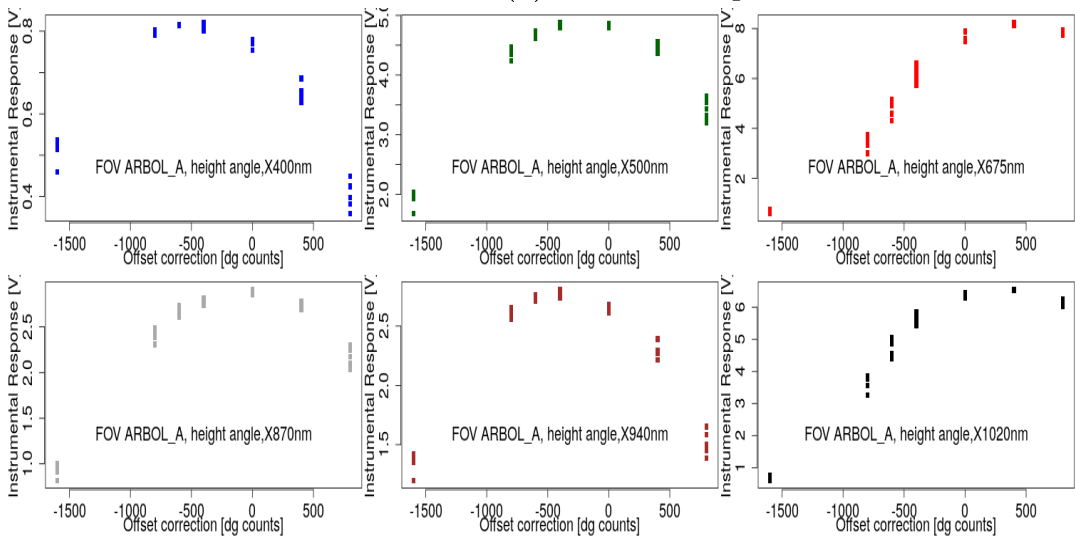

(b) Height angle characterization

Figure 5.5. Characterization of the FOV for the 6 wavelengths measured by $ARBOL_A$

The second day is on May, 30 and the Sun is centered in the FOV. The improvement can be clearly appreciated.

Unfortunately, ARBOL telescopes appear to be cross-eyed. Within the same instrument, different telescopes show different FOVs. In this case, it is not possible to correct every telescope at the same time,

(a) Azimuthal angle characterization

(b) Height angle characterization

Figure 5.6. Characterization of the FOV for the 6 wavelengths measured by $ARBOL_B$

because different correction factors are necessary. For example, in fig. 5.6b the $400nm$ maximum point is approximately $offs = -500$, while the $675nm$ maximum point is $offs = +500$. The offset difference is $\Delta offs = 1000$, corresponding to a large angular difference of $0.25°$. Thus, it is not possible to point to the Sun both the $400nm$ telescope
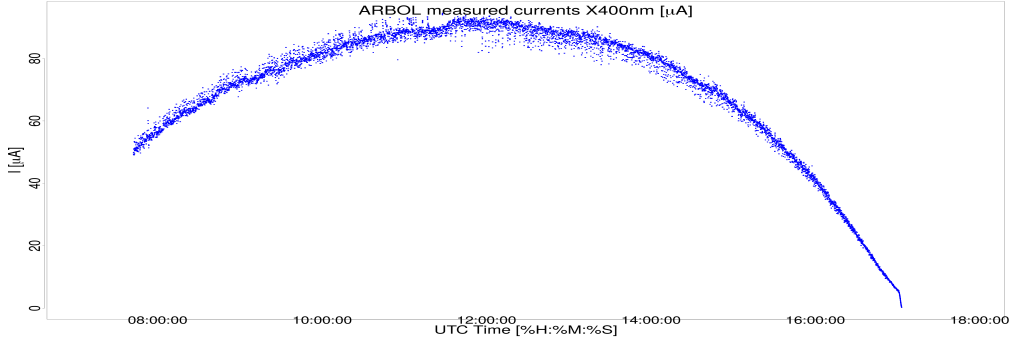
(a) 22nd March, no offset correction.
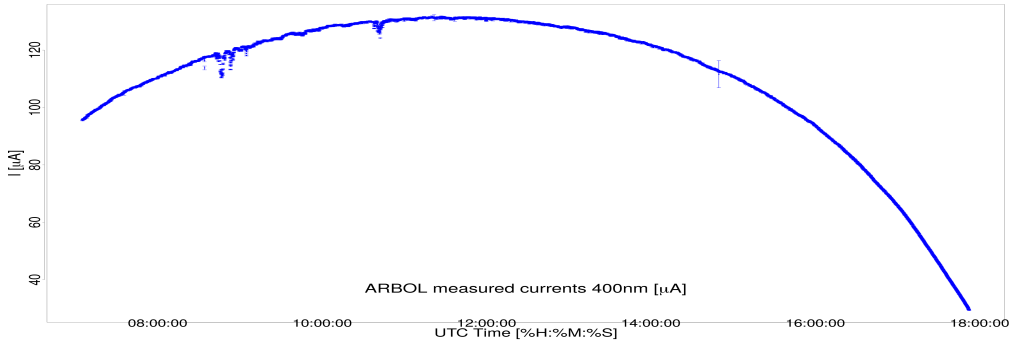
(b) 30th May, corrected measurements

Figure 5.7. Comparison between currents measured by the same instrument, $ARBOL_A$, with and without field of view correction

and the $675nm$ telescope at the same time.

In fact, for $ARBOL_A$ a tradeoff has been obtained because the FOV differences are small. An offset correction $+200$ has been applied to the height direction, -900 to the azimuth direction. Specifically, the corrected direction is $0.05°$ southward and $0.24°$ westward. All the spectral channels are now considered to give reliable results.

Nevertheless, it has not been possible to correct the six telescopes of $ARBOL_B$. The height angle direction is the most critical. In addition to the $675nm$ case we discussed above, the $1020nm$ channel also shows a large FOV difference ($+800$ counts or $0.22°$). Hence, it was chosen to sacrify the $675nm$ and $1020nm$ signal quality and improve the other wavelengths. As a result, $ARBOL_B$ measures reliable and low noise signals in the $400nm$, $500nm$, $870nm$ and $940nm$ spectral bands. The offset corrections are -350 counts in the height direction ($0.09°$ northward) and $+700$ in the azimuth direction ($0.19°$ eastward).

For the sake of completeness, we briefly discuss the possible causes of discrepancies among the FOVs. Actually, the reason why the telescope FOV curves are different is still under study. A possible source of this discrepancy cound be due to the position of the photodiodes. Soldering issues prevented the photodiodes from being mounted close enough to the surface. This can partially explain the observed FOV differences. However, further investigations remain necessary to tackle the disturbing factor.

5.2.2   Temperature monitoring and correction

As discussed in section 3.2.1 a bias can be introduced in the $1020nm$ measured photocurrents because of thermal effects. Here we explain how to apply a temperature correction to the measured data. Moreover, a case where the correction is significant is reported below.

Each front end electronics is added with a thermistor-based voltage divider, so that the temperature is measured directly within the telescope. To get T from the measured voltage, equations 3.37 and 3.40 must be inverted:

$$RT1(T) = \frac{R3}{\frac{V^{Reft}}{V^{Temp}(T)} - 1} \tag{5.11}$$

$$T(^{\circ}C) = \left(log \left(\frac{RT1(T)}{RT1(298.15K)} \right) \frac{1}{\beta} + \frac{1}{298.15} \right)^{-1} - 273.15 \tag{5.12}$$

where $V^{Temp}(T)$ is the measured voltage. The voltage divider schematic is shown in figure 3.13.

Once the temperature is known, it is possible to access the corresponding photosensitivity:

$$S_\lambda(T) = S_\lambda(25) + \frac{dS_\lambda}{dT} S_\lambda(25) \frac{1}{100} \tag{5.13}$$

where $S_\lambda(25)$ and $\frac{dS_\lambda}{dT}$ are taken from the plots 3.1a and 3.2a respectively. More precisely, the plots can be averaged over the filter transmission band to obtain:

$$S_{1020nm}(25) = 0.56 \frac{A}{W} \tag{5.14}$$

and

$$\frac{dS_{1020nm}}{dT} = 0.30 \frac{\%}{^{\circ}C} \tag{5.15}$$

Finally, if $S_\lambda(T)$ is known, the temperature correction is straightforward:

$$I = I_{meas} \frac{S_\lambda(25)}{S_\lambda(T)} \tag{5.16}$$

In equation 5.16 I is the current measured by the same instrument at $25°C$, I_{meas} the actual measured current before applying any correction.
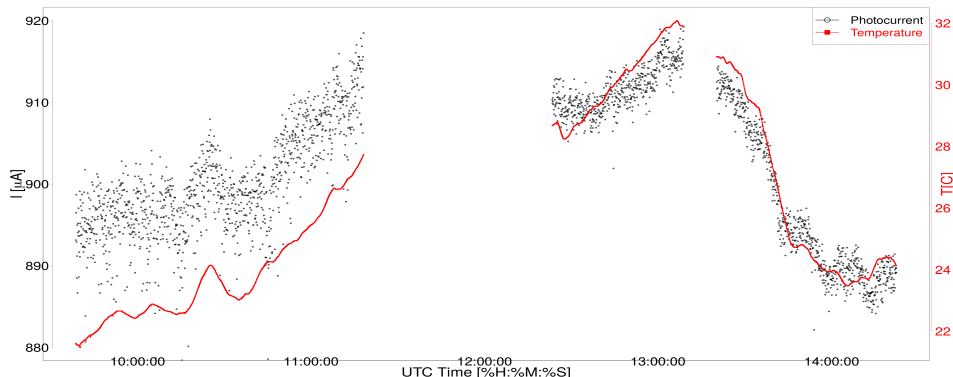

Figure 5.8. Comparison between ARBOL $1020nm$ photocurrent and the temperature measured inside the instrument simultaneously. A correlation between the two quantities can be appreciated.

Measurements have been made from the observatory site on 17th June 2019. The weather was sunny and hot. The temperature of the $1020nm$ telescope rised from almost $22°C$ in the morning up to $32°C$. Figure 5.8 compares $I_{meas}(1020nm)$ with the temperature T measured simultaneously. The shape of the two plots is similar. The correlation between temperature and photocurrent strongly suggests a change in photosensitivity.

I_{meas} has been corrected for the sensitivity variation and the result is shown in figure 5.9 (black dots). The trend imposed by the temperature is completely removed from the signal. Moreover, we can compare the $870nm$ currents (not affected by temperature) with the corrected $1020nm$ signal (fig. 5.9 again). Note that their behaviour is the same.

Accordingly, we can conclude:
- the temperature variations affect the $1020nm$ photodiode sensitivity.
- it is possible to account for temperature biases and the corrected signals are reliable measurements.

Finally, we focus on the temperature uncertainties. Figure 5.10 shows the temperature diurnal evolution and the corresponding un-
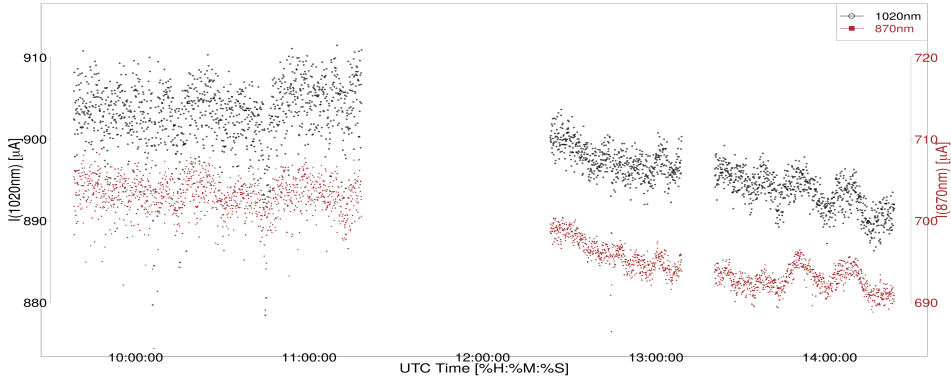
Figure 5.9. ARBOL corrected $1020nm$ currents (black) and $870nm$ currents (brown). The latters are not affected by the temperature.

certainties. The error bars are apparently very small, namely down to 0.01 degree as obtained from the root mean square of the data set acquired within $\Delta t = 0.5s$. This indicates that the measured voltage, and therefore the electronic behaviour, are very stable and give a very precise measurement. However, the accuracy of the temperature measurement is larger, as discussed below.

Three telescopes have the temperature monitor circuit: $400nm$, $940nm$ and $1020nm$. According to equation 5.15, a temperature shift of 2 degrees corresponds to an uncertainty below 0.6%. Nevertheless, different thermistor characteristics might lead to larger discrepancies, expecially under winter conditions when temperature is much less than the reference one, 25°. A careful calibration of the temperature measuring system, especially in terms of accuracy, could be considered as a possible future developement.

5.3   Future developments

The goal of this section is to summarize some characterizations to do in the future. They certainly will help improving the performances of the instrument:

– as mentioned above, each thermistor inside ARBOL telescopes has a different characteristic curve. The characterization of their response in a temperature-controlled environment will improve the accuracy of the temperature measurement.
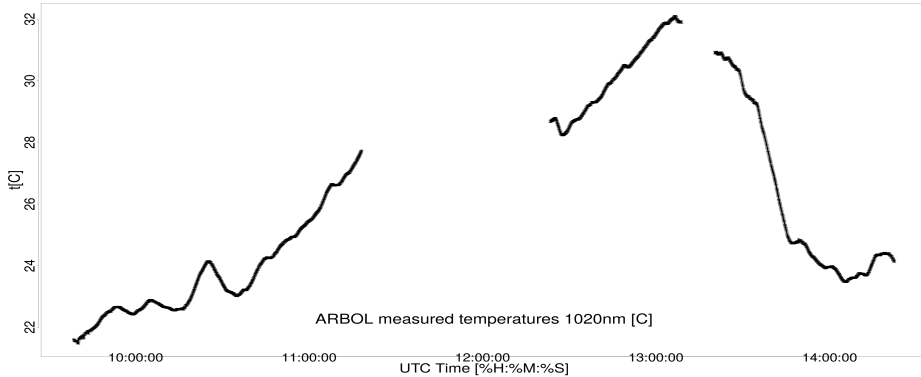
83

Figure 5.10. Temperature measured on 17th June from Saint Barthelemy. Error bars are shown.

 – the spectral filter efficiency is expected to change as the instrument ages: the stability in time of the filter response will have to be monitored.

 – in section 3.1.3 it was shown that the photodiode linearity limit is above the maximum light power observed by ARBOL. An experimental check with linearity measurements is a further development.

 – tests to optimize the high gain value R_2 in the front end circuit of ARBOL are still expected. The optimal R_2 value:

 • covers the entire sky light power range

 • guarantees a good signal-to-noise ratio in the front-end output voltage.

Finally, in section 5.2.1 we stressed that the telescope FOVs in ARBOL are not homogeneous. Probably there is still a mechanical issue to be solved. Afterwards, the FOVs will have to be characterized again.

5.4 Acronyms in chapter 5

Acronym	Meaning
TIA	TranImpedance Amplifier
FWHM	Full Width at Half Maximum
NI	National Instruments
LSB	Least Significant Bit
FOV	Field Of View

CHAPTER 6

Measurements and calibration

The current chapter is about calibration and measurements. As explained earlier (sect. 5.1.2), diffuse sky measurements still need some improvement. Hence, the discussion will focus on direct Sun measurements. These measurements have been collected with ARBOL from two different locations: the ARPA site and the OAVdA site. The first place is in the suburbs of the city of Aosta ($583m$ a.s.l.), while the second one is located at the astronomical observatory of Saint Barthelemy ($1700m$ a.s.l.). Despite the altitude difference, the two measurement sites are close (approximately $\simeq 20Km$).

The famous Lambert-Beer law relates the aerosol optical depth and the direct Sun measurements:

$$I = I_0 e^{-AM\tau} \tag{6.1}$$

In the 6.1 I is the measured irradiance, I_0 the irradiance at the top of the atmosphere, τ the optical depth, AM the air mass factor (this factor depends on the solar zenith angle, SZA). To obtain the AOD τ_{aer}, two steps are necessary:
- first, the photometer must be calibrated to find I_0, the extraterrestrial constant.
- second, τ_{aer} is obtained from τ by subtracting all the other components of the optical depth.

Even though there are some open issues regarding data uncertainties, the instrument performances can be considered satisfactory. Promising data have been collected from both the ARBOLs (the ARPA one and the observatory one).

We start examining the photometer calibration and the related issues. Afterwards, a discussion about the data quality is given.

6.1 The photometer calibration

The photometer calibration process is the retrieval of I_0. Three methods can be used to retrieve I_0:
1) Absolute calibration of the sensor and use of the extraterrestrial constant measured by a satellite
2) Langley method
3) Calibration transfer

Typically, a 1% accuracy is required for the applicability of the calibration. If an inaccurate estimate I_0^* is obtained from calibration, the optical depth retrieval is biased as well (Cachorro, Toledano, Berjón, *et al.* 2008 [18]). To prove it, we assume:

$$ln(I_0^*) = ln(I_0) + \epsilon \qquad (6.2)$$

where ϵ is the bias in the inaccurate estimate. From the retrieval based on I_0^*, we get the following AOD:

$$\tau^{mis} = \frac{1}{AM}(ln(I_0^*) - ln(I)) = \frac{1}{AM}(ln(I_0) + \epsilon - ln(I)) = \tau + \frac{\epsilon}{AM} \quad (6.3)$$

In the 6.3, $\frac{\epsilon}{AM}$ is the bias (while τ the unbiased optical depth).

For this reason, an accurate photometer calibration is very important. Unfortunately, both instrumental problems or atmospheric instabilities can affect the calibration and generate a bias ϵ.

The calibration method 1) relies on the I_0 measured by a satellite. It compares the satellite measurement with the radiation power measured at ground. To allow the comparison between different instruments, the photometer must be calibrated absolutely. This calibration is non-trivial: it needs a traceable calibrated source and very precise measurements, which are generally very expensive and time-comsuming. Moreover, accuracy is often an issue.

The other two calibration methods are generally preferred because they don't need absolute calibration. The Langley method is the primary calibration method used in worldwide photometer networks such as Aeronet (Holben, Eck, Slutsker, *et al.* 1998[8]). Unfortunately, this method suffers some accuracy issues, described below. The calibration transfer has been employed in the current work.

6.1.1 The calibration transfer

We devote this section to discussing the calibration transfer (Estellés, Campanelli, Smyth, *et al.* 2012[24]). Within this approach, a reference

calibrated instrument and an uncalibrated one make measurements from the same site. Moreover, they must observe the same wavelength. The Lambert-Beer law can be written for both instruments:

$$I(\lambda) = I_0(\lambda)e^{-AM\tau} \tag{6.4}$$

and

$$V(\lambda) = V_0(\lambda)e^{-AM\tau} \tag{6.5}$$

where V refers to the reference instrument, I to the uncalibrated one. If the measurements are simultaneous, the atmospheric transmission factor $e^{-AM\tau}$ in the equations above must be the same. Accordingly, the following equality holds as well:

$$\frac{I}{I_0} = \frac{V}{V_0} \tag{6.6}$$

In the 6.6 I and V are measured, while V_0 is known because the reference instrument is already calibrated. Consequently, I_0 can be directly obtained as:

$$I_0 = \frac{I \times V_0}{V} \tag{6.7}$$

In our case, the calibrated instrument is the POM02 sunphotometer installed at the ARPA site. The $400nm$, $500nm$, $675nm$, $870nm$ and $1020nm$ calibration factors have been transferred. No $940nm$ calibration was possible because no $940nm$ measurements are available from POM. The ARBOLs have been calibrated for some days in May, June and August 2019.

Actually, the data sets from POM photometer and ARBOL are not actually simultaneous. There is 1 measurement per minute from POM, about 12 per minute from ARBOL (one every 5 seconds). Hence, the 12 measurements from ARBOL feed the following linear regression:

$$ln(I) = A + AM(t^{mis})B \tag{6.8}$$

where $ln(I)$ are the currents measured by ARBOL, A and B the fitting parameters, AM the geometrical air mass factor. The latter can be accessed in two steps:
- the solar zenith angle must be retrieved. It's the Blanco-Muriel algorithm to provide SZA from the measurement time t^{mis} (Blanco-Muriel, Alarcón-Padilla, López-Moratalla, *et al.* 2001[12])
- the Kasten and Young formula (see eq. 6.15 below) takes the SZA

input and computes the corresponding air mass factor, AM (Kasten and Young 1989[5]).

If A and B are known, it is possible to extrapolate a value matching the POM measurement time and obtain simultaneous measurements.
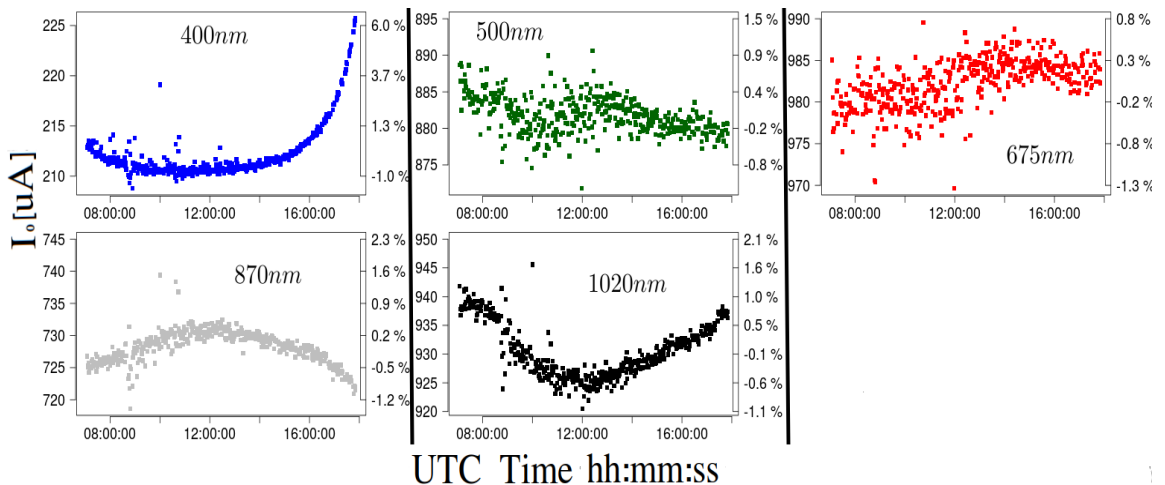

Figure 6.1. Retrieved I_0 for $ARBOL_A$ on 30th May. Currents are shown on the left y-axis, percentage discrepancies on the right y-axis

Figure 6.1 shows the I_0 values for May 30th. I_0 is a time constant. Thus, the $\frac{I}{V}$ ratio should cancel out the time dependences of I and V. In fact, we expect them to differ no more than 1%. Results in fig. 6.1 differ for less than 2% for all the wavelenghts but the $400nm$. The latter shows a discrepancy up to 6%: no wavelength is below the 1% threshold. The trends of the curves suggest that there are some factors introducing a bias in the calibration transfer. These factors might be a different filter transmission or a different field of view of the two instruments. Further investigation in controlled laboratory conditions are necessary to detect calibration biases.

For the time being the I_0 data sets are averaged to reduce the uncertainties. The following values have been found on May the 30th in the morning:

Wavelength [nm]	$I_0[\mu A]$	$\delta I_0[\mu A]$	Percentage
400	212.2	2.8	1.3%
500	881.9	3.0	0.3%
675	982.4	4.4	0.4%
870	728.4	3.4	0.5%
1020	930.5	5.2	0.6%

Table 6.1. I_0 constants for the various wavelengths obtained from the calibration transfer,30th May in the morning

The uncertainties δI_0 are obtained from the root mean square of the I_0 data sets. The uncertainties are close to 1% for the $400nm$ spectral channel, less than 1% for the other wavelengths. This is enough for the purposes of ARBOL.
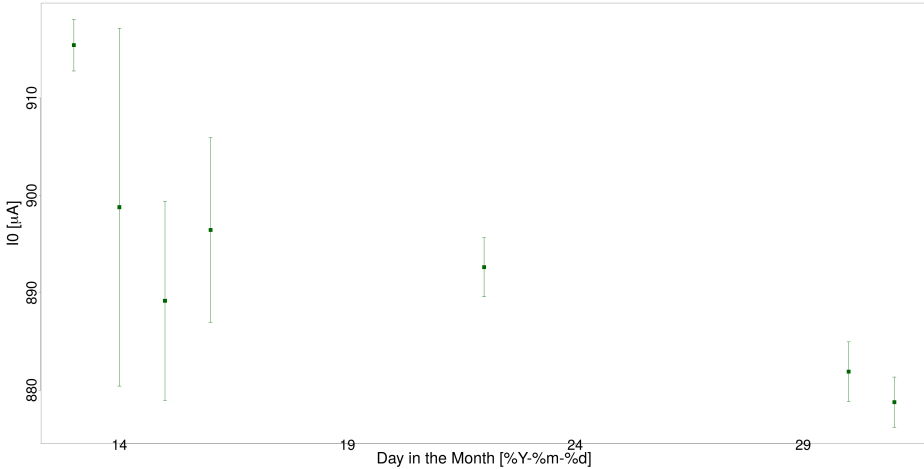

Figure 6.2. Calibration transfer during May 2019 for $ARBOL_A$, $500nm$

Finally, figure 6.2 shows the daily averaged I_0 obtained for the $500nm$ wavelength in May 2019. We can point out the following conclusions:
- The standard deviation is within 1% for days 13, 22, 30 and 31.
- Days 14,15 and 16 show a large standard deviation because clouds have passed into the field of view. Clouds interferences must be removed, but a cloud screening algorithm has not been developed yet.
- I_0 values from different days differ for more than 1%. These discrepancies might be due to monthly-long drifts or to some unknown source of noise. Only a longer data series of calibration transfer results will allow a better understanding of the monthly behaviour of I_0.

I_0 values from the same measurement day have been used to retrieve the aerosol optical depth. When a calibration constant from the same day is not available, a value from the closest day has been selected.

6.1.2 Langley calibration and its limits

The Langley plot and the corresponding issues are discussed in this section. Data from ARBOL are used to clarify the Langley limits. We stress these limits affect every photometer: they are typical of the Langley method.

The Lambert-Beer law can be written in the following form:

$$ln(I) = ln(I_0) - AM\tau \qquad (6.9)$$

If τ can be considered as constant, equation 6.9 defines a straight line. The graph is then called a Langley plot. The Langley calibration retrieves the extraterrestrial constant I_0 from the data set $(AM_i, ln(I_i))$ through a linear regression: the intercept of the straight line gives $ln(I_0)$.

Typically, the Langley plot lasts half a day because the solar zenith angle must increase (or decrease). τ must remain constant within this time interval. If τ is not constant for shorter time intervals, outliers are introduced. These can be discarded and I_0 can still be obtained from the regression.

However, if τ is proportional to AM^{-1}:

$$\tau = \tau_1 + \frac{\tau_2}{AM} \qquad (6.10)$$

it's straightforward to demonstrate the straight line intercept changes:

$$ln(I) = ln(I_0) - AM\tau = ln(I_0) - \tau_2 - AM\tau_1 \qquad (6.11)$$

In the equation above, the intercept is $ln(I_0) - \tau_2$ and the Langley plot is biased. Unfortunately, a single Langley plot cannot identify τ_2 in Eq. 6.11, because no information is contained in the set of couples $(ln(I_i), AM_i)$. This problem is well known in the scientific literature (Campanelli, Nakajima, and Olivieri 2004[14]; Marenco 2007[17];Kiedron and Michalsky 2016[30]).

Statistical analysis of the Langley plot intercepts $ln(I_0) - \tau_2$ is necessary to improve the I_0 estimate. Averaging the monthly series of $ln(I_0) - \tau_2$ cancels out the biased component τ_2. However, about a month or more is required to collect enough data and have enough statistics.

Mountaintops on volcanic islands (like Mauna Loa in Hawaii or Izaña on Tenerife) are ideal environments to collect Langley plot data series. In these sites the constancy of the optical depth ($\Rightarrow \tau_2 =$

0) is frequent. With a small standard deviation a smaller number of Langleys is necessary to achieve the desired calibration accuracy (Kiedron and Michalsky 2016[30]).

By contrast, in sites like the Aosta Valley, periods of stable atmospheres are much less common. The statistics of τ_2 is likely to be biased with a large standard deviation. Generally, the 1% accuracy threshold cannot be reached from this kind of measurement sites. For these reasons, ARBOL has been calibrated through the calibration transfer method explained above (sect. 6.1.1).
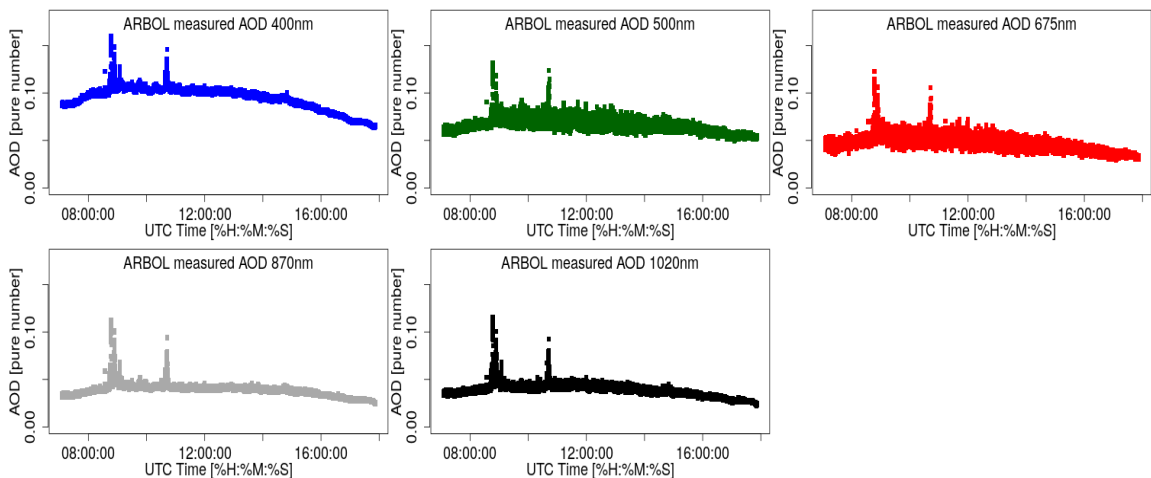

Figure 6.3. Aerosol optical depth measured by $ARBOL$ on 30th May

Nevertheless, a Langley plot can still be attempted and compared with the calibration transfer results. The data set from the morning of May the 30th has been used for this purpose. This particular day of measurements is interensting since the corresponding Langley plot exhibits a tangible bias. Table 6.2 contains I_0 factors retrieved from the Langley. They are 4% lower than the corresponding values from the calibration transfer, on average. The AOD curve shapes in figure 6.3 are proportional to AM^{-1}.

Wavelength [nm]	$I_0[\mu A]$	$\delta I_0[\mu A]$
400	200.3	0.2
500	844.9	0.6
675	951.0	0.8
870	704.7	0.5
1020	903.5	0.6

Table 6.2. I_0 constants for the various wavelengths obtained from the Langley plot, May the 30th in the morning

The I_0 value from calibration transfer is considered the correct one. This choice is the most reasonable because of the Langley problems described above. Consequently, the observed AOD shape is caused by a real AOD change and the Langley plot results in table 6.2 are actually biased, as in Eq. 6.10 and 6.11.

6.2 The aerosol optical depth

The current section describes how to retrieve the aerosol optical depth (AOD) from the direct radiation measurements. We assume the instrument already calibrated (I_0 known).

Among the spectral channels of ARBOL, only the $400nm$, $500nm$, $675nm$, $870nm$ and $1020nm$ wavelengths are considered from now on. The $940nm$ wavelength is observed to retrieve the water vapour content. However, the algorithm for the retrieval of the water vapour is not developed yet: this is a task to be developed in the future. Thus, for the time being this wavelength is ignored.

6.2.1 The retrieval of the AOD

Let's write the Lambert-Beer law 6.1 in the following way (see Iqbal 1983[3] or Gueymard 2001[13]):

$$I = I_0 e^{-AM_{aer}\tau_{aer}} e^{-AM_{ray}\tau_{ray}} e^{-AM_{o3}\tau_{o3}} \qquad (6.12)$$

In the equation above each atmospheric process is given its own transmissivity. Three different phenomena cause light extinction:
- Rayleigh scattering from air molecules: τ_{ray} is the corresponding optical depth
- Ozone absorption, described by τ_{o3}
- aerosol extinction: the AOD is represented by τ_{aer} in eq. 6.12

Other minor phenomena (e.g. NO_2 absorption) are neglected.
The 6.12 can be inverted:

$$\tau_{aer} = \frac{1}{AM_{aer}}(ln(I_0) - ln(I) - AM_{o3}\tau_{o3} - AM_{ray}\tau_{ray}) \qquad (6.13)$$

Different extinction mechanisms occur at different altitudes. For instance, the ozone absorption happens the most in the ozone layer (about $20Km$ above Earth surface). Multiple air mass factors (AM) account for altitude differences. For these reasons, both equations 6.12 and 6.13 assign different AM values. In fact, the aerosol air mass (AM_{aer}) is approximated with the air molecules factor (AM_{ray}):

$$AM_{ray} \simeq AM_{aer} \qquad (6.14)$$

because the aerosol vertical profile is not well known. The Kasten and Young formula is used to retrieve AM_{ray}:

$$AM_{ray} = \frac{1}{cos(SZA) + 0.50572(96.07995 - SZA)^{-1.6364}} \qquad (6.15)$$

where SZA is expressed in degrees. The error caused by the above assumption is not large: Gueymard 2001[13] claims that different air masses are significant only for solar zenith angles greater than 80°.

The ozone air mass formula is based on Antón, López, Costa, *et al.* 2009[19]:

$$AM_{o3} = \frac{1}{\sqrt{1 - \frac{R+r}{R+h} sin^2(SZA)}} \qquad (6.16)$$

where R is the Earth radius; r the measurement site altitude and h the altitude of the ozone layer.

τ_{o3} and τ_{ray} must be known to obtain τ_{aer} from the 6.13. The former is accessed multiplying the corresponding absorption cross section by the ozone abundance, according to Gueymard [13]:

$$\tau_{o3} = u_{o3} \times \sigma_{o3}(\lambda) \qquad (6.17)$$

As for the Rayleigh optical depth, Bodhaine (Bodhaine, Wood, Dutton, *et al.* 1999[9]) proposes the following equation:

$$\tau_{Ray}(\lambda) = (\lambda)\frac{PA}{m_a g}\sigma_{ray} \qquad (6.18)$$

where $\sigma_{ray}(\lambda)$ is the Rayleigh cross section of the air molecules; P the site air pressure when the measurement is performed; A the Avogadro's number, m_a the average molecular weight of dry air and g the gravity acceleration. σ_{ray} can be obtained analitically, but Bodhaine proposes a nice formula depending on the wavelength. The latter approach is followed here.
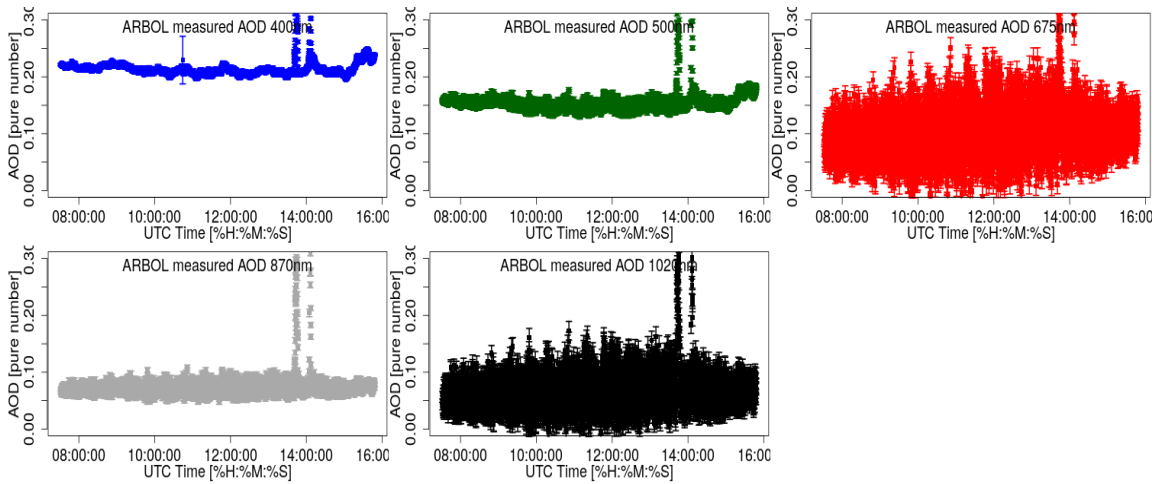
(a) 29th August. Two cloud passages around 14:00 UTC can be appreciated
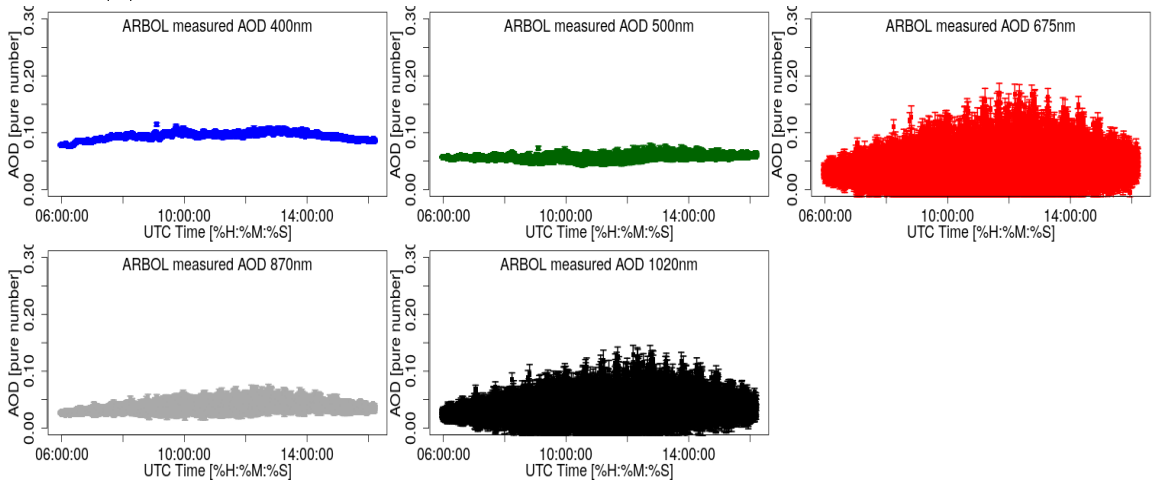
(b) 3rd September

Figure 6.4. AOD measured from ARPA VdA

6.2.2 The measurements

Figure 6.4 shows the AOD plots retrieved on 29th August and 3rd September from the ARPA VdA site. Fixed values of pressure ($P = 947hPa$) and ozone abundance ($u_{o3} = 300DU$) have been assumed to get τ_{ray} and τ_{o3}. Both the 29th August and the 3rd September were sunny. Two fast cloud passages appear on 29th August in the afternoon (fig. 6.4a, around 14:00UTC). They are responsible for two sudden AOD increases. From the plots in figure 6.4 we can reach the following

96

conclusions:

- As the wavelength increases, the AOD decreases. A more efficient extinction at shorter wavelengths is generally due to fine aerosols.
- The sky was cleaner on 3rd September (fig. 6.4b). The measured AOD is half or less the AOD measured on 29th August (fig. 6.4a).
- The spectral channels $675nm$ and $1020nm$ show no reliable measurements. The FOV problems discussed before (sect. 5.2.1) introduce noise and the signal becomes indistinguishable.

By contrast, measurements from the observatory location are trustworthy even at $675nm$ and $1020nm$. A fixed pressure $P = 830hPa$ and a fixed ozone content $u_{o3} = 300DU$ have been assumed to retrieve τ_{ray} and τ_{o3} respectively.

Figure 6.5 and 6.6 show the AOD diurnal evolution for three different days: 13th July, 16th August, and 4th September.
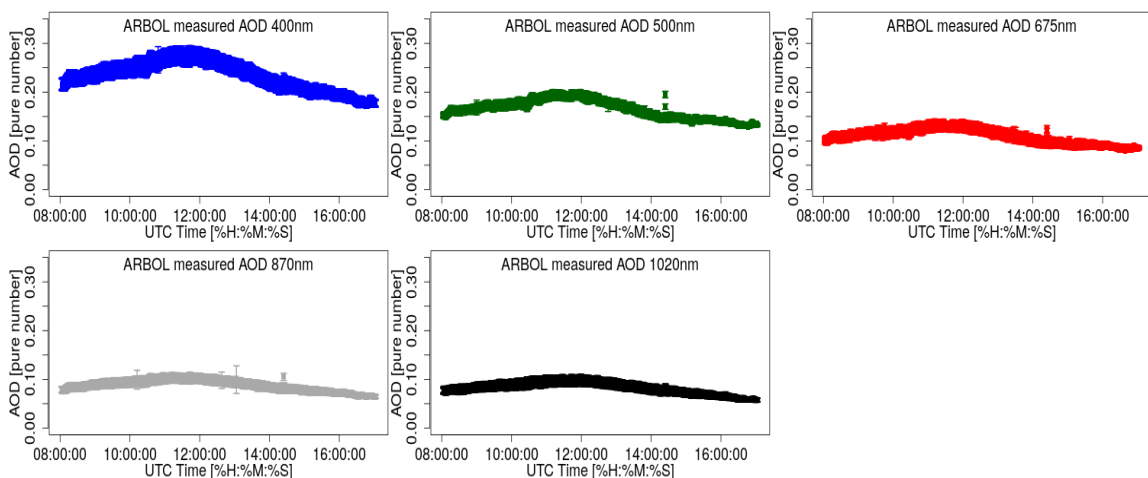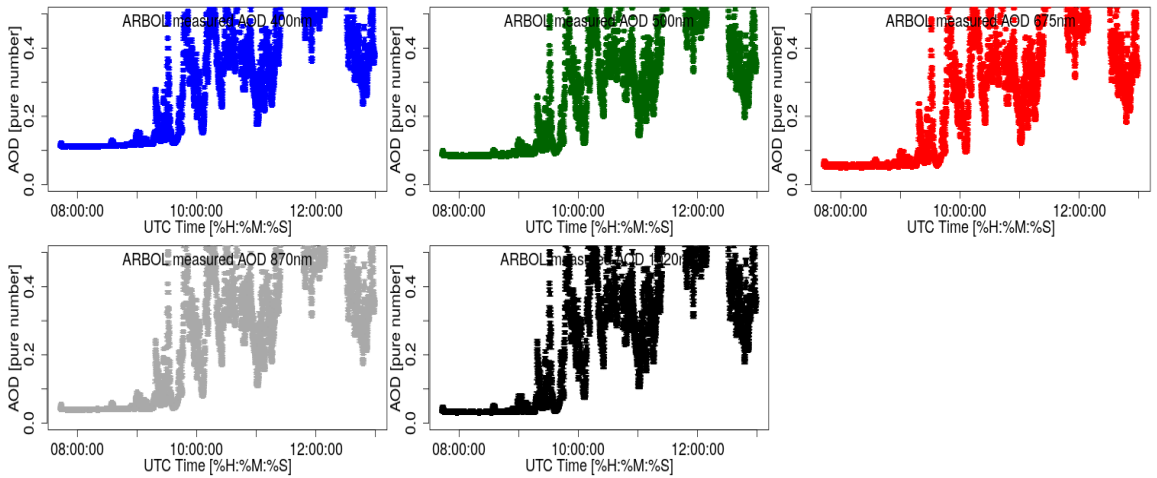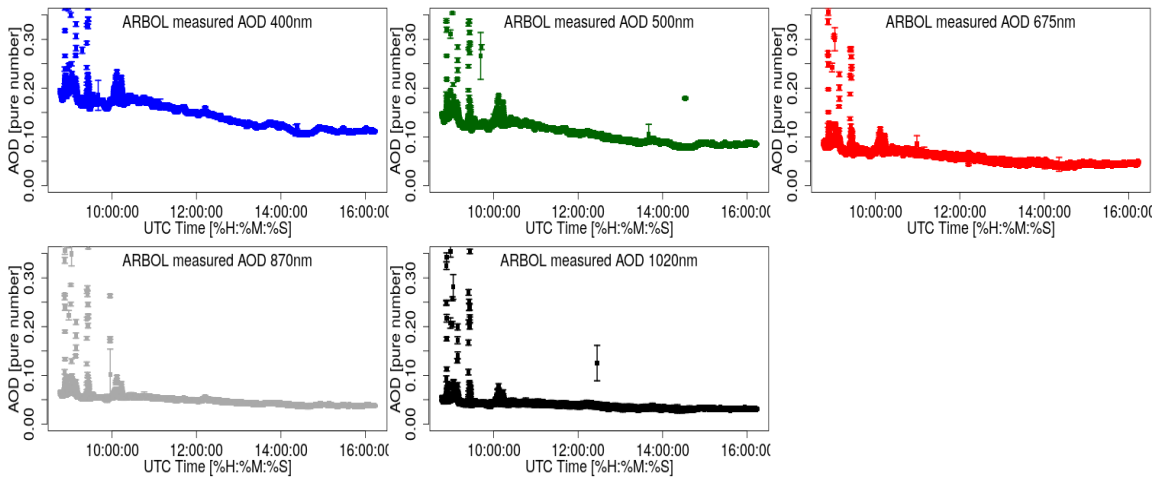

Figure 6.5. 13th July. AOD measured from the observatory site (OAVdA)

The plots are interesting for the following reasons:
- the wavelength increases, the AOD decreases (figs. 6.5 and 6.6). Once again, the AOD spectral behaviour is detected.
- On 16th August (see figs. 6.6a) the weather was initially sunny, cloudy afterwards. Consequently, the AOD increases and fluctuates dramatically after 10 UTC. Clouds disturb the measurements and a cloud-screening algorithm will have to be applied in the future.
- For each observed wavelength, a decreasing AOD trend is visible on

97

(a) 16th August. Weather becomes cloudy after 10 UTC

(b) 4th September. Thin clouds pass before 10 UTC, afterwards the AOD decreases

Figure 6.6. AOD measured from the observatory site (OAVdA).

4th September (fig. 6.6b). The instrument has the sensitivity to detect the AOD diurnal evolution.

6.2.3 The uncertainties

Uncertainty analysis is still preliminary. The absolute uncertainty in the AOD measurement can be described as:

$$\delta\tau = \frac{1}{AM}\left(\frac{\delta I}{I} + \frac{\delta I_0}{I_0}\right) \tag{6.19}$$

For the sake of simplicity, only a single air mass factor is considered here, which is given by the Kasten and Young formula (eq. 6.15).

The term $\frac{\delta I_0}{I_0}$ in equation 6.19 is from the results of the calibration transfer (see table 6.1). δI describes the uncertainty in the measured current, I. Generally, the calibration term is the dominant error source (Giles, Sinyuk, Sorokin, *et al.*2019 [34]). Aerosol optical depth uncer-
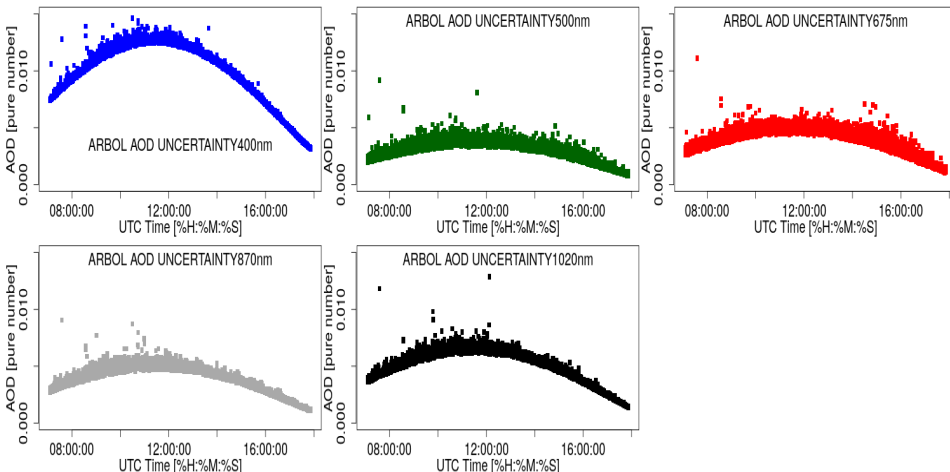

Figure 6.7. Aerosol optical depth errors for the measurements taken on 30th May.

tainties on 30th May are plotted in figure 6.7. The AM^{-1} depence of the uncertainties can be appreciated. The errors are not larger than $\delta\tau_{aer} = 0.014$ for the $400nm$ wavelength, $\delta\tau_{aer} = 0.01$ for the other wavelengths. Generally speacking, the AOD uncertainty limits for commercial sunphotometers are < 0.01 for $\lambda > 440nm$ and < 0.02 for shorter wavelengths (see Holben, Eck, Slutsker, *et al.* 1998 [8]).

The results obtained for ARBOL are good. However, the uncertainty evaluation is not complete yet. There are still some minor issues to be investigated. For example, Carlrund (Carlund, Kouremeti, Kazadzis, *et al.*2017 [31]) considers other error sources such as:
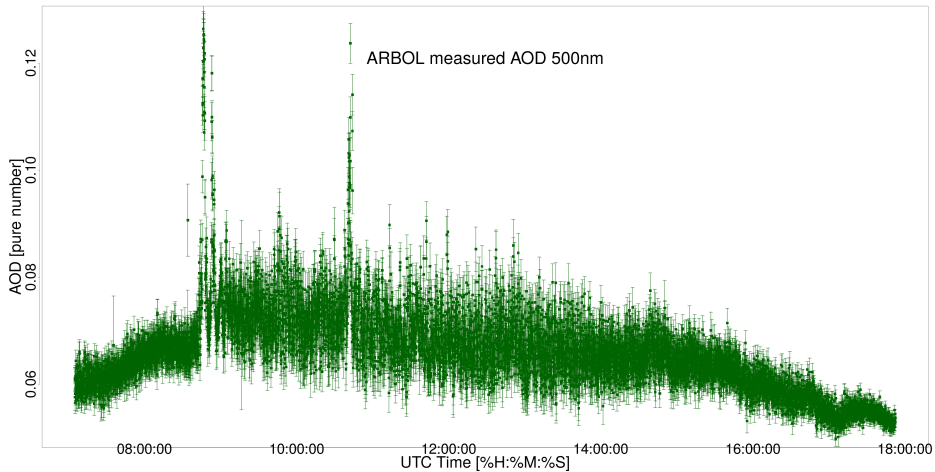- uncertainty of Rayleigh optical depth

Figure 6.8. The same plot of figure 6.3 at $500nm$. The uncertainties are plotted as error bars
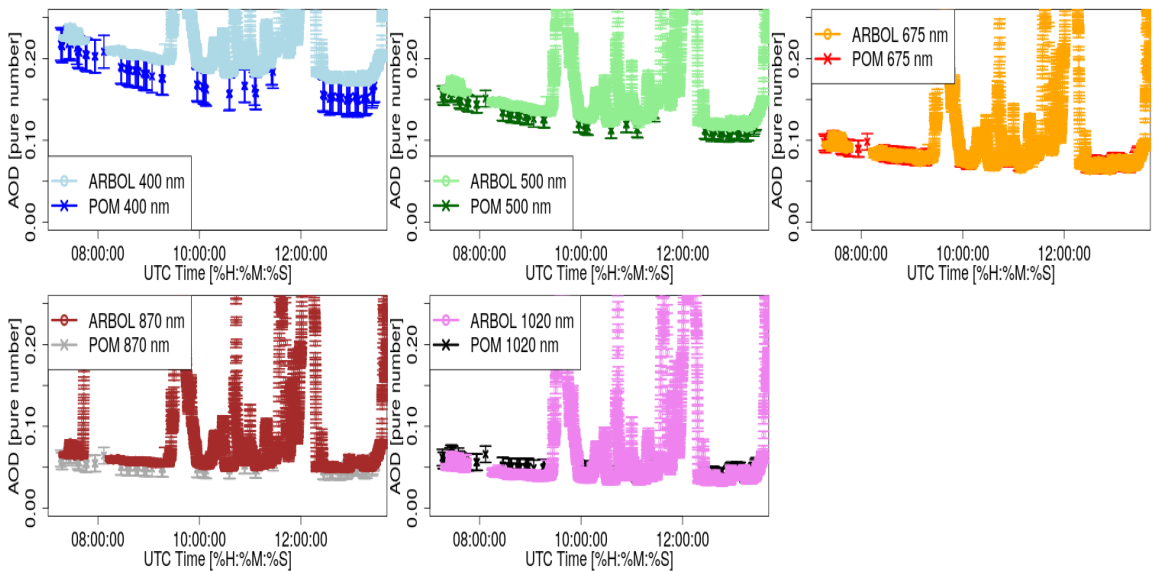

Figure 6.9. ARBOL and POM AOD comparison on 30th August

- uncertainty of ozone optical depth
- uncertainty of measured signal including circumsolar contribution
- uncertainty due to neglected gaseous absorption
- uncertainty in solar position and air mass terms

The uncertainty evaluation must account for all these factors. Consequently, the final AOD uncertainty of ARBOL will be greater than the

current estimate.

ARBOL AOD accuracy can be investigated by comparing its data with those from POM (see fig. 6.9 for a comparison between $ARBOL_A$ and POM). The latter is assumed as reference, because it is well calibrated and tested. The comparison is done on 30th August from the ARPA site. ARBOL data show sudden signal increases due to clouds, while POM data are screened. The agreement is within experimental errors for all the wavelengths. The worst agreement is shown for the $400nm$ channel, where the calibration transfer precision was the least good.

We can conclude the AOD accuracy is good.

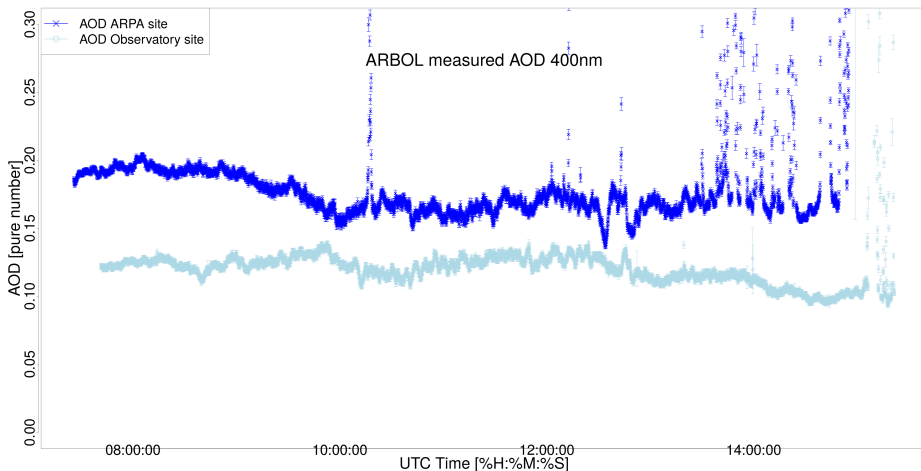## 6.2.4 Comparisons between simultaneous data from ARPA and OAVdA

Figure 6.10. 17th September, ARPA VdA-OAVdA AOD measurements at $400nm$

We discuss here data observed on 4th September and on 17th September from both the ARPA and the observatory sites. Only $400nm$ and $500nm$ channels are shown because $ARBOL_B$ (installed at ARPA VdA) has got mechanical problems, explained above (sect. 5.2.1). These days are insteresting because significant AOD differences are observed between the two measurement places. By contrast, other measurement days from July, August and early September have not shown AOD differences.
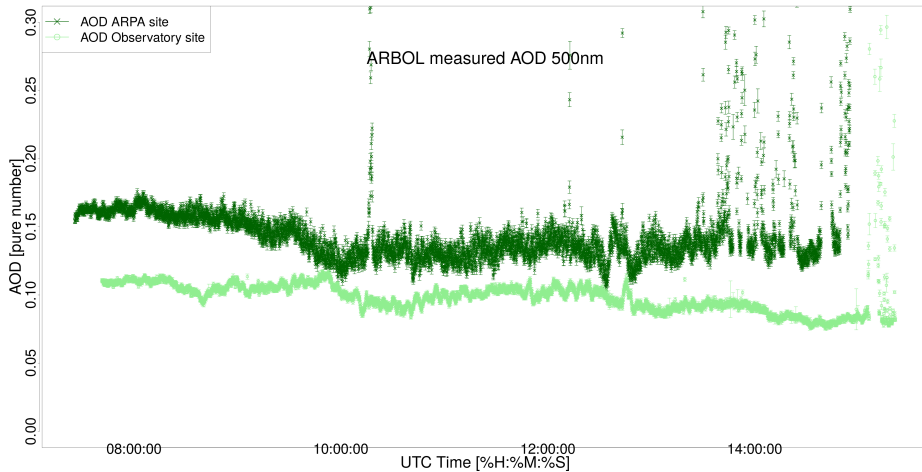
Figure 6.11. 17th September, ARPA VdA-OAVdA AOD measurements at $500nm$
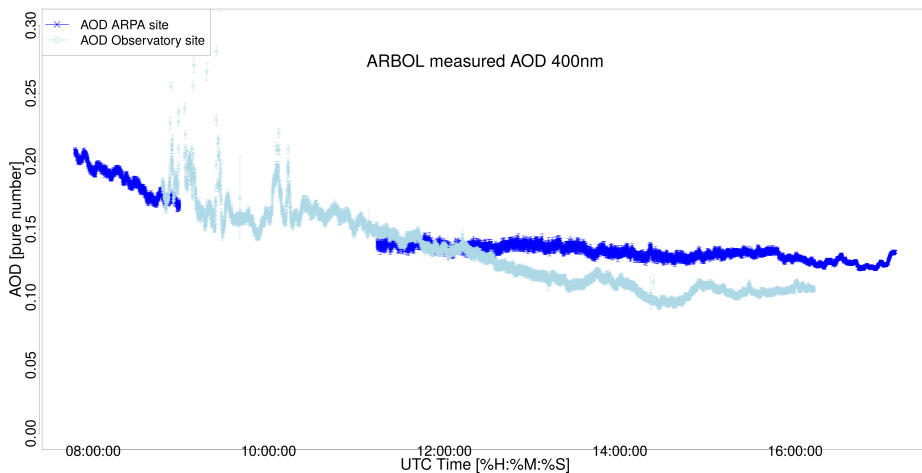

Figure 6.12. 4th September, ARPA VdA-OAVdA AOD measurements at $400nm$

The AOD from ARPA VdA is greater than the same data from OAVdA on 17 September (fig. 6.10 and 6.11). We can suppose the difference is contained into the atmospheric layer between the observation sites. Thus, simultaneous observations can actually catch the AOD in the lowest atmospheric layer.

During day 4 (fig. 6.12 and 6.13) the AOD decreases in both sites, particularly between 11:00 and 15:00 UTC. However, evolution differences can be appreciated. The lowering trend appears faster in the
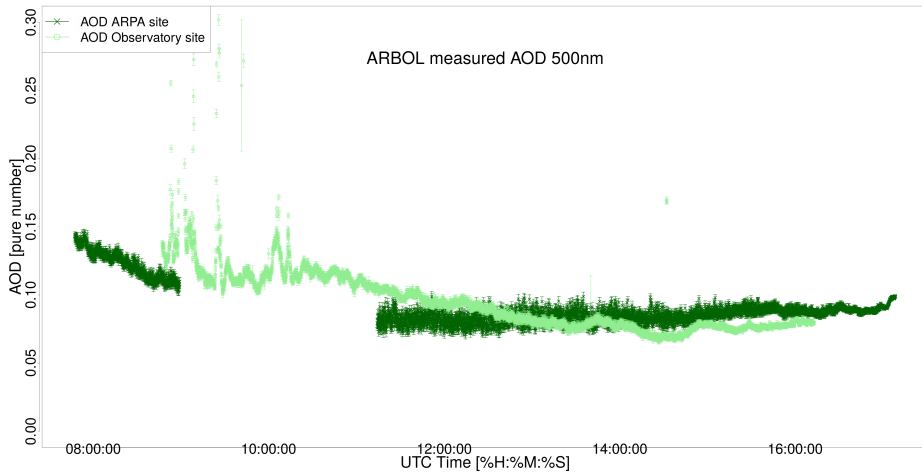
Figure 6.13. 4th September, ARPA VdA-OAVdA AOD measurements at $500nm$

OAVdA site, slower in ARPA. Moreover, the AOD drop is more consistent in the observatory site. We can assume that the removal of aerosol has a greater impact on the higher observing site rather than the ARPA VdA site within the Aosta Valley. Thus, the simultaneous measurement technique helps gaining an insight into the aerosol dynamics in the Valley.

6.3   Acronyms in chapter 6

Acronym	Meaning
ARPA VdA	Agenzia Regionale Protezione Ambiente Valle d'Aosta
OAVdA	Osservatorio Astronomico della Regione Autonoma Valle d'Aosta
SZA	Solar Zenith Angle
AOD	Aerosol Optical Depth
FOV	Field Of View

Conclusion

In the current PhD job a novel and efficient sunphotometer was developed. Its structure is based on seven parallel telescopes. Six of them contain a bolometer to observe sunlight or skylight. The seventh tracks the Sun during its diurnal motion. The instrument name is ARBOL (ARray of BOLometers).

The instrument is multispectral, each telescope observes a different narrow spectral band in the visible to near infrared range (from $400nm$ to $1020nm$). Inside the telescope, a lens-pinhole system selects light from a field of view 1.1° wide.

The sensor is a silicon photodiode. The preamplification is a transimpedance circuit with two gain options to enhance the instrument dynamic range. A thermistor monitors the internal telescope temperature and avoids thermal drift issues.

A flexible and open source software was developed to offer full control over the acquisition strategy.

The mechanics, the electronics and the control software of ARBOL were designed and created to achieve superior performances with respect to conventional sunphotometers, indeed:

- generally, sunphotometers make sequential observations with a wheel mounting spectral filters. ARBOL has six parallel telescopes, hence it can observe six spectral channels simultaneously

- ARBOL can observe the direct normal irradiance with a high temporal resolution (every 5 seconds).

- almucantar sky measurements reach a high angular resolution ($\sim 1°$)

The bolometric characterization, the characterization of the field of view and the characterization of the temperature response were performed, while the calibration has been transferred from a traceable sunphotometer. ARBOL was already and successfully employed for a measurement campaign started during Spring 2019 and lasted until the end of Summer 2019. The results confirmed that the direct sunlight extinction is measured with a sensibility akin to that of well tested photometers.

Simultaneous measurement were collected from ARPA VdA and OAVdA, two locations near Aosta placed at $583m$ a.s.l and $1700m$ a.s.l respectively. Thus, the comparison between simultaneous measurement reveals information about the aerosols of the lowest atmospheric layer. Preliminary comparison results are discussed in this thesis.

Finally, the future enhancements of ARBOL are described as well. We list here only the most relevant ones:

– the improvement of the field of view and the telescopes fine alignment (see sect. 5.2.1). For istance, a diffuser can be introduced to make the field of view more flat.

– the development of the sky radiance measurements. The high gain must be further optimized to enhance the sky radiance sensibility.

– the Improved Langley method will be tested on ARBOL measurements (Campanelli, Nakajima, and Olivieri 2004[14]). This method provides calibration based only on reliable sky radiance measurements.

CHAPTER 8

Ringraziamenti

References: scientific papers

[1] S. Twomey, "The influence of pollution on the shortwave albedo of clouds", *Journal of the atmospheric sciences*, vol. 34, no. 7, pp. 1149–1152, 1977.

[2] E. P. Shettle and R. W. Fenn, "Models for the aerosols of the lower atmosphere and the effects of humidity variations on their optical properties", 1979.

[4] T. Nakajima, M. Tanaka, and T. Yamauchi, "Retrieval of the optical properties of aerosols from aureole and extinction data", *Applied Optics*, vol. 22, no. 19, pp. 2951–2959, 1983.

[5] F. Kasten and A. T. Young, "Revised optical air mass tables and approximation formula", *Applied optics*, vol. 28, no. 22, pp. 4735–4738, 1989.

[6] T. Nakajima, G. Tonna, R. Rao, P. Boi, Y. Kaufman, and B. Holben, "Use of sky brightness measurements from ground for remote sensing of particulate polydispersions", *Applied Optics*, vol. 35, no. 15, pp. 2672–2686, 1996.

[7] M. Hess, P. Koepke, and I. Schult, "Optical properties of aerosols and clouds: The software package opac", *Bulletin of the American meteorological society*, vol. 79, no. 5, pp. 831–844, 1998.

[8] B. N. Holben, T. F. Eck, I. Slutsker, D. Tanre, J. Buis, A. Setzer, E. Vermote, J. A. Reagan, Y. Kaufman, T. Nakajima, *et al.*, "Aeronet - a federated instrument network and data archive for aerosol characterization", *Remote sensing of environment*, vol. 66, no. 1, pp. 1–16, 1998.

[9] B. A. Bodhaine, N. B. Wood, E. G. Dutton, and J. R. Slusser, "On rayleigh optical depth calculations", *Journal of Atmospheric and Oceanic Technology*, vol. 16, no. 11, pp. 1854–1861, 1999.

[10] O. Dubovik, A. Smirnov, B. Holben, M. King, Y. Kaufman, T. Eck, and I. Slutsker, "Accuracy assessments of aerosol optical properties retrieved from aerosol robotic network (aeronet) sun and sky radiance measurements", *Journal of Geophysical Research: Atmospheres*, vol. 105, no. D8, pp. 9791–9806, 2000.

[11] J. Schwartz and L. M. Neas, "Fine particles are more strongly associated than coarse particles with acute respiratory health effects in schoolchildren", *Epidemiology*, vol. 11, no. 1, pp. 6–10, 2000.

[12]   M. Blanco-Muriel, D. C. Alarcón-Padilla, T. López-Moratalla, and M. Lara-Coira, "Computing the solar vector", *Solar Energy*, vol. 70, no. 5, pp. 431–441, 2001.

[13]   C. A. Gueymard, "Parameterized transmittance model for direct beam and circumsolar spectral irradiance", *Solar Energy*, vol. 71, no. 5, pp. 325–346, 2001.

[14]   M. Campanelli, T. Nakajima, and B. Olivieri, "Determination of the solar calibration constant for a sun-sky radiometer: Proposal of an in-situ procedure", *Applied optics*, vol. 43, no. 3, pp. 651–659, 2004.

[16]   S. Kazadzis, A. Bais, V. Amiridis, D. Balis, C. Meleti, N. Kouremeti, C. Zerefos, S. Rapsomanikis, M. Petrakakis, A. Kelesis, *et al.*, "Nine years of uv aerosol optical depth measurements at thessaloniki, greece", *Atmospheric Chemistry and Physics*, vol. 7, no. 8, pp. 2091–2101, 2007.

[17]   F. Marenco, "On langley plots in the presence of a systematic diurnal aerosol cycle centered at noon: A comment on recently proposed methodologies", *Journal of Geophysical Research: Atmospheres*, vol. 112, no. D6, 2007.

[18]   V. Cachorro, C. Toledano, A. Berjón, A. de Frutos, B. Torres, M. Sorribas, and N. S. Laulainen, "An "in situ" calibration correction procedure (kciclo) based on aod diurnal cycle: Application to aeronet–el arenosillo (spain) aod data series", *Journal of Geophysical Research: Atmospheres*, vol. 113, no. D12, 2008.

[19]   M. Antón, M. López, M. J. Costa, A. Serrano Pérez, D. Bortoli, M. Bañón García, J. M. Vilaplana, and A. M. Silva, "Influence of the ozone profile above madrid (spain) on brewer estimation of ozone air mass factor", 2009.

[20]   W. Kester, "Taking the mystery out of the infamous formula," snr= 6.02 n+ 1.76 db," and why you should care", *Analog Devices Tutorial, MT-001 Rev. A*, vol. 10, no. 08, 2009.

[21]   E. Drury, D. J. Jacob, R. J. Spurr, J. Wang, Y. Shinozuka, B. E. Anderson, A. D. Clarke, J. Dibb, C. McNaughton, and R. Weber, "Synthesis of satellite (modis), aircraft (icartt), and surface (improve, epa-aqs, aeronet) aerosol observations over eastern north america to improve modis aerosol retrievals and constrain surface aerosol concentrations and sources", *Journal of Geophysical Research: Atmospheres*, vol. 115, no. D14, 2010.

[22]   M. Mazzola, C. Lanconelli, A. Lupi, M. Busetto, V. Vitale, and C. Tomasi, "Columnar aerosol optical properties in the po valley, italy, from mfrsr data", *Journal of Geophysical Research: Atmospheres*, vol. 115, no. D17, 2010.

[24]   V. Estellés, M. Campanelli, T. Smyth, M. Utrillas, and J. Martínez-Lozano, "Evaluation of the new esr network software for the retrieval of direct sun products from cimel ce318 and prede pom01 sun-sky radiometers", *Atmospheric Chemistry and Physics*, vol. 12, no. 23, pp. 11 619–11 630, 2012.

[26]   C. Heald, D. Ridley, J. Kroll, S. Barrett, K. Cady-Pereira, M. Alvarado, and C. Holmes, "Contrasting the direct radiative effect and direct radiative forcing of aerosols", *Atmospheric Chemistry and Physics*, vol. 14, no. 11, pp. 5513–5527, 2014.

[27]   L. Orozco, "Optimizing precision photodiode sensor circuit design", *Application note MS-2624*, pp. 1–5, 2014.

[28]   J. Putaud, F. Cavalli, S. Martins dos Santos, and A. Dell'Acqua, "Long-term trends in aerosol optical characteristics in the po valley, italy", *Atmospheric Chemistry and Physics*, vol. 14, no. 17, pp. 9129–9136, 2014.

[29]   C. Emde, R. Buras-Schnell, A. Kylling, B. Mayer, J. Gasteiger, U. Hamann, J. Kylling, B. Richter, C. Pause, T. Dowling, *et al.*, "The libradtran software package for radiative transfer calculations (version 2.0. 1)", *Geoscientific Model Development*, no. 5, pp. 1647–1672, 2016.

[30]   P. Kiedron and J. Michalsky, "Non-parametric and least squares langley plot methods", *Atmospheric Measurement Techniques*, vol. 9, no. 1, pp. 215–225, 2016.

[31]   T. Carlund, N. Kouremeti, S. Kazadzis, and J. Grobner, "Aerosol optical depth determination in the uv using a four-channel precision filter radiometer", *Atmospheric Measurement Techniques*, vol. 10, no. 3, pp. 905–923, 2017.

[33]   H. Diémoz, F. Barnaba, T. Magri, G. Pession, D. Dionisi, S. Pittavino, I. K. Tombolato, M. Campanelli, L. S. D. Ceca, M. Hervo, *et al.*, "Transport of po valley aerosol pollution to the northwestern alps–part 1: Phenomenology", *Atmospheric Chemistry and Physics*, vol. 19, no. 5, pp. 3065–3095, 2019.

[34] D. M. Giles, A. Sinyuk, M. G. Sorokin, J. S. Schafer, A. Smirnov, I. Slutsker, T. F. Eck, B. N. Holben, J. R. Lewis, J. R. Campbell, *et al.*, "Advancements in the aerosol robotic network (aeronet) version 3 database–automated near-real-time quality control algorithm with improved cloud screening for sun photometer aerosol optical depth (aod) measurements", *Atmospheric Measurement Techniques*, vol. 12, no. 1, pp. 169–209, 2019.

References: books

[3] M. Iqbal, *An introduction to solar radiation*. Elsevier, 1983.

[23] P. Kulkarni, P. A. Baron, and K. Willeke, *Aerosol measurement: principles, techniques, and applications*. John Wiley & Sons, 2011.

[25] I. W. G. I, *Climate Change 2013-The Physical Science Basis: Summary for Policymakers*. Intergovernmental Panel on Climate Change, 2013.

References: master thesis

[32] M. Pallavera, *Realizzazione e caratterizzazione di un sistema automatizzato per lánalisi delláerosol atmosferico*, 2017.

References: datasheets

[36] T. Instruments, *Lm4040-n/-q1 precision micropower shunt voltage reference*, October 2000–Revised June 2016. [Online]. Available: https://www.ti.com/lit/ds/symlink/lm4040-n.pdf.

[37] ——, *Opax191 36-v, low power, precision, cmos, rail-to-rail input/output,low offset voltage, low input bias current op amp*, December 2015–Revised April 2016. [Online]. Available: http://www.ti.com/lit/ds/sbos701a/sbos701a.pdf.

[38] N. Instruments, *Specifications usb-6210, 16 ai (16-bit, 250 ks/s), 4 di, 4 do usb multifunction i/o device*, 2015-2016. [Online]. Available: http://www.ni.com/pdf/manuals/375194d.pdf.

[39] S. S. D. HAMAMATSU PHOTONICS K.K., *Si pin photodiodes s5106, s5107, s7509, s7510, Chip carrier package for surface mount*, May 2018. [Online]. Available: `https://www.hamamatsu.com/resources/pdf/ssd/s5106_etc_kpin1033e.pdf`.

[40] O. Semiconductor, *Bd135 / 137 / 139, Npn epitaxial silicon transistor*, August 2013. [Online]. Available: `https://www.onsemi.com/pub/Collateral/BD139-D.PDF`.

[41] S. S. D. HAMAMATSU PHOTONICS K.K., *Si photodiodes s1337 series, For uv to ir, precision photometry*, October 2015. [Online]. Available: `https://www.hamamatsu.com/resources/pdf/ssd/s1337_series_kspd1032e.pdf`.

[45] Littelfuse, *He700 miniature dual in-line reed relay, Reed relays dil packaged > he700*. [Online]. Available: `https://m.littelfuse.com/~/media/electronics/datasheets/reed_relays/littelfuse_reed_relays_he700_datasheet.pdf.pdf`.

[50] O. Semiconductor, *Lm317, ncv317, 1.5 a adjustable output,positive voltage regulator*. [Online]. Available: `https://www.onsemi.com/pub/Collateral/LM317-D.PDF`.

[51] ——, *Lm337, 1.5 a, adjustable output, negative voltage regulator*. [Online]. Available: `https://www.onsemi.com/pub/Collateral/LM337-D.PDF`.

References: technical Notes

[20] W. Kester, "Taking the mystery out of the infamous formula," snr= 6.02 n+ 1.76 db," and why you should care", *Analog Devices Tutorial, MT-001 Rev. A*, vol. 10, no. 08, 2009.

[27] L. Orozco, "Optimizing precision photodiode sensor circuit design", *Application note MS-2624*, pp. 1–5, 2014.

[35] B. E. Tony Wang, *Compensate transimpedance amplifiers intuitively, Application report sboa055a*, March 1993 – Revised March 2005. [Online]. Available: `http://www.ti.com/lit/an/sboa055a/sboa055a.pdf`.

[42] *Daq m series, Ni usb-621x user manual*. [Online]. Available: `https://www.ni.com/pdf/manuals/371931f.pdf`.

[43] *Det36a(/m), si biased detector, user guide.* [Online]. Available: `https://www.thorlabs.com/drawings/7a5e33817328f68a-9CCF5A5D-C90D-6B03-B6FA4D3B421ACCF6/DET36A_M-Manual.pdf`.

[44] *Grounding considerations for improved measurements.* [Online]. Available: `ftp://ftp.ni.com/evaluation/pxi/Grounding_Considerations.pdf`.

[46] *Ni-daq mx base 3.x.* [Online]. Available: `http://www.ni.com/pdf/manuals/371259h.pdf`.

[47] *Noise analysis in operational amplifier circuits, Application report.* [Online]. Available: `http://www.ti.com/lit/an/slva043b/slva043b.pdf`.

[48] *Noise analysis of fet transimpedance amplifiers, Burr-brown application bulletin.* [Online]. Available: `http://www.ti.com/lit/an/sboa060/sboa060.pdf`.

[49] *Photodiode characteristics and applications.* [Online]. Available: `http://www.osioptoelectronics.com/application-notes/AN-Photodiode-Parameters-and-Characteristics.pdf`.

[52] *Si photodiodes, Silicon photodiode handbook.* [Online]. Available: `https://www.hamamatsu.com/resources/pdf/ssd/e02_handbook_si_photodiode.pdf`.

[53] *Voltage feedback op amp gain and bandwidth, Mt-033 tutorial.* [Online]. Available: `https://www.analog.com/media/en/training-seminars/tutorials/MT-033.pdf`.

[54] Y. Zhen, *Using mcp6491 op amps for photodetection applications.* [Online]. Available: `http://ww1.microchip.com/downloads/en/AppNotes/01494A.pdf`.